RMZ

MATERIALS and GEOENVIRONMENT

MATERIALI in GEOOKOLJE

RMZ – M&G, **Vol. 67**, No. 3
pp. 91–159 (2020)

Ljubljana, September 2020

Table of Contents

Kazalo

Original scientific papers

Izvirni znanstveni članki

Original scientific article

Received: Dec 07, 2020
Accepted: Dec 11, 2020
DOI: 10.2478/rmzmag-2020-0013

Characterisation of the Wear of the Roller Cone Drill Bit Caused by Improperly Chosen Drilling Regime

Karakterizacija obrabe kotalnega dleta povzročene z nepravilno izbiro režima vrtanja

Jurij Šporin*
Faculty of Natural Sciences and Engineering, Department of Geotechnology, Mining and Environment, University of Ljubljana, Aškerčeva 12, Ljubljana, Slovenia
* jurij.sporin@ogr.ntf.uni-lj.si

Abstract

The rapid drop in the penetration rate or failure of the drill bit during the drilling process delays the drilling process. In our investigation, the '*in situ*' drilling parameters were monitored during the drilling process along with the roller cone drill bit, which is suitable for drilling in soft rock formations (IADC 136). The drill bit was thoroughly examined to determine its damage and wear occurred during drilling along with decreasing penetration rate. The modern and standardised investigation methods were used to analyse the rock materials and the micro- and macro-structure of the materials of the roller cone bit. The analyses were performed by means of optical and electron microscopes, simultaneous thermal analysis of the steel materials, analysis of the chemical composition of the materials of the drill bit and determination of the geomechanical parameters of the drilled rock. The resulting wear, localised fractures and cracks were quantitatively and qualitatively defined and the parameters were correlated to the drilling regime and the rock material. The results of our investigation of the material of the roller cone bit can serve as a good basis for the development of new steel alloys that can withstand higher temperatures and allow effective drilling without structural changes of the steel material.

Keywords: drilling regime, roller cone bit, wear, reduced penetration rate, change of the material properties.

Izvleček

Upad napredka vrtanja ali odpoved dleta med vrtanjem imata za posledico daljši čas izvajanja vrtalnih del. V toku raziskave obrabe kotalnega dleta IADC 136, ki je namenjen uporabi pri vrtanju skozi mehkejše kamnine, so se izvajale opazovanja in meritve vrtalnih parametrov. Po končanem odseku vrtanja, ko je hitrost napredovanja drastično padla, se je kotalno dleto natančno pregledalo za ugotovitev nastalih poškodb med vrtanjem. Za ugotavljanje in določanje načina obrabe so se uporabile moderne in standardne metode. Izvedla se je analiza hribinskega materiala skozi katerega se je vrtalo, ter analiza mikro in makro strukture materialov kotalnega dleta. Analiza materialov se je izvedla z uporabo optičnega in elektronskega mikroskopa, simultane termalne analize jekla kotalnega dleta, določila se je kemijska sestava jekla kotalnega dleta in geomehanske karakteristike hribinskega materiala skozi katerega se je vrtalo. Izražena obraba kotalnega dleta se je kvantitativno in kvalitativno ovrednotila v povezavi z režimom vrtanja in karakteristikami hribine skozi katere se je vrtalo. Rezultati naše raziskave materialov kotalnega dleta lahko služijo kot dobra osnova za razvoj novih jeklenih zlitin, ki bodo prenašale visoke temperature, ki nastajajo med vrtanjem, brez strukturnih sprememb jeklenih materialov.

Ključne besede: režim vrtanja, kotalno dleto, obraba, zmanjšani napredek vrtanja, sprememba lastnosti materiala.

Introduction

The time of effective drilling operations depends on the properties of the materials from which the roller cone bit components are manufactured. The roller bit will wear out due to the consequences of effects of the rock material it is drilling through and the drilling regime. The penetration rate decreases due to the wear of the bit.

The following factors among all have a significant influence on the effective operation of the roller cone bit are the steel material from which the rollers and teeth of the bit are made, the drilling regime (load on the bit during drilling, torque, number of bit revolutions and the quantity and properties of the drilling fluid) and the properties of rock drilled.

We analysed the mechanical properties of the steel material of the roller cone bit IADC 136, 155.57 mm (6 1/8″), which was drilling through carbonatic siltstone where sandstone plates and rare thin layers of clay and limestone exist in a total length of 87.89 m.

Our research focused on the resistance of the steel material of the roller cone bit to the rock material using a selected drilling regime.

To accomplish this, it was necessary to use scientific approaches to determine the causes that lead to wear of the bit and identify the weak points on the bit that need to be technologically modified in order to enhance the effective drilling time.

Drilling Principle of the Roller Cone Drill Bit

The roller cone bit contains cutting elements, i.e. teeth or inserts, which are mounted on the rollers. The rollers, which are inserted into the bearings of the bit, rotate around their axis. They are driven by rotating drilling rods that drives the body of the drill bit on which the roller is mounted. Nozzles (outlet) for the drilling fluid are attached to the bit body to effectively remove the rock particles from the borehole bottom of the borehole and to cool the rollers and teeth of the bit. The drilling fluid flows through the nozzles from the inside of the drill pipes into the area of the bit. When the orifice is reduced, which is the ratio of the cross-section of the drill bit to the cross-section of the nozzles, the velocity of the drilling fluid flow is increased significantly. The increasing velocity of the drilling fluid has a positive effect on the flow of the drilling fluid around the rollers, which effectively removes the drilled rock particles from the bottom of the borehole and contributes to the fracture of the borehole, especially in the softer, poorly bonded rocks [1–20].

The roller cone bit with steel teeth, which is investigated here, is used in softer, poorly bonded rock formations. The teeth of the rollers are large and sharp so that they can penetrate deep into the soft rock structures where the rock is crushed and removed from the crushed area. The teeth are protected with a carbide coating to improve durability, which increases the effective operating time. The axes of the rollers do not intersect at the point of the vertical axis of the bit, but do have an offset corresponding to the point of the vertical axis of the bit. The offset of the roller axis is normally in the range of 2°–5°.

The load on tooth F, which causes the tooth to penetrate the rock (h), is a linear combination of the force acting against the surface at the tip of the tooth and the force acting against the surface formed by the inclined surfaces of the tooth.

When rollers and bits with teeth on rollers are made of the same material, we could state the following [21]:

$$F = (C_1 \cdot w + C_2 \cdot h) \cdot l \cdot \sigma_p, \qquad (1)$$

where F is the load on a single tooth of the bit; C_1 is the coefficient of friction on the surface at the tooth tip (-); w is the tooth width (m); C_2 is the coefficient of friction on the tooth surface in contact with the rock (-); h is the penetration depth of the tooth (m); l is the tooth length (m) and σ_p is the compressive strength of the rock (Pa).

The result of the reaction force F on the tooth of the bit in contact with the rock is equal to the load generated on the bit [22] and is given by:

$$\text{WOB} = n_t \cdot F, \qquad (2)$$

where WOB is the weight on the bit (N) and n_t is the number of teeth in contact with the rock.

The volume of the crater of the crushed rock V_{crat} (m^3) created by one tooth, assuming that the crater has a conical shape, is stated by the following equation [22]:

$$V_{crat} = \frac{1}{3} \cdot \pi \cdot r_{crat}^2 \cdot h, \tag{3}$$

where r_{crat} is the crater radius (m) and h is the crater depth (m).

By determining the volume of a single crater formed by a single tooth, the penetration rate can be evaluated, which is defined by the volume of the rock craters on the entire cutting surface of the roller cone bit in number of revolutions [22] and can be stated as follows.

$$\mathrm{ROP} = \frac{V_{crat} \cdot n_t \cdot \mathrm{RPM}}{A_{bit}}, \tag{4}$$

where ROP is the rate of penetration (m/s); V_{crat} is the volume of the crater of the removed rock (m^3); RPM is the number of rotations of the bit (s^{-1}) and A_{bit} is the cutting area of the bit (m^2).

As the bit advances through the rock, the teeth of the roller cone bit wear out. Further, the parameters that influence the penetration rate (ROP) of the roller cone bit are focused here to determine the wear of the bit. Bourgoyne and Young [23, 24] defined these as influential parameters as stated in Eq. (5).

$$\mathrm{ROP} = f_1 \cdot f_2 \cdot f_3 \cdot f_4 \cdot f_5 \cdot f_6 \cdot f_7 \cdot f_8, \tag{5}$$

where f_1 is the effect of formation strength or rock durability; f_2 is the effect of formation depth; f_3 is the effect of formation compaction or pore pressure; f_4 is the effect of differential pressure; f_5 is the effect of bit diameter and bit weight; f_6 is the effect of rotary speed; f_7 is the effect of tooth wear and f_8 is the effect of bit hydraulics.

We investigated the wear of the roller cone bit, the occurrence of damage and the change in the properties of the bit materials under the conditions of the properties of the material drilled through, the drilling regime (weight on the bit, speed, etc.) and the hydraulics of the drilling fluid in the area of the bit.

Materials and Methods

When determining the characterisation of the wear of the roller cone bit at the time of the investigations, detailed analyses were made against the drilling regime, the materials from which the bit was made and the rock through which the bit was drilled. To achieve this purpose, in the first phase, we carried out a survey of the bit, which included an overview of the condition of the bit after drilling according to the IADC bit dull standard. In this part, we investigated the condition of the teeth and rollers of the bit after drilling through known rock.

While drilling through the known rock, the following drilling parameters of drilling regime were monitored:

- The penetration rate;
- The length of the drilled interval;
- The load on the bit;
- The bit RPM; and
- The amount, pressure and properties of the drilling fluid.

We carried out a complete analysis of the steel materials of the roller cone bit, which included the following investigations:

- Analysing the micro- and macrostructure of roll cone bit materials with an reflected light microscope (Olympus BX61 and Olympus SZ61 stereo microscope using the Analysis 6.0 image analysis system);
- The composition of the carbide coating of bit teeth using the XRF (X-ray fluorescence) method (Thermo NITON XL3t XRF analyser);
- A cross-sectional view of bit teeth using a scanning electron microscope (SEM) and EDS analysis (energy dispersive X-ray spectroscopy) (Jeol JSM 5610);
- A dilatometric analysis of tooth steel and tooth carbide coating with the low temperature dilatometer (Baehr-Thermoanalyse GmbH DIL 801);
- Chemical analysis of the components of the teeth and rollers with an ICP (inductively coupled plasma) analyser (ICP-OES Agilent 720);

- DSC (Differential Scanning Calorimetry) of tooth carbide coating and tooth steel with a thermal analyser (NETZSCH STA 449 C Jupiter) and
- Vickers hardness tests of the tooth steel with a 100 g load using microhardness tester (Shimadzu type M).

The properties of the rock obtained by sampling were estimated based on the analysis of Rock Lab 1.0.

Results

The results of our analysis show the way and the mechanisms that cause wear of the bit material at fixed or established rock properties in connection with the operating parameters of the drilling.

Drilling work

Drilling was carried out with a 1992 N-1000 drill rig. The interval in which we observed the performance of the IADC 136 roller cone drill bit included a length of drilling interval from 1535.15 m to 1623.04 m depth, corresponding to a length of 87.89 m. The penetration rate during the observed interval ranged from 0.2 m/h to 0.4 m/h. The remaining drilling regime parameters are shown in Table 1.

The 40 mass.% bentonite drilling fluid was used during drilling. The properties of the drilling fluid are shown in Table 2.

Table 1. *Drilling regime parameters*

Parameters	Units	Value	Value
Depth	m	1535.15–1600.00	1600.00–1623.04
Rotary speed	rpm	35	45
Load on drill bit	kN	30	40
Pump pressure	MPa	5.5	5.5
Pump capacity	m^3/min	0.845	0.845

Table 2. *The properties of drilling fluid*

Parameters	Units	Value
Density	kg/m^3	1150–1170
Viscosity (Fann Funnel)	s	45–48
Plastic viscosity (Fann Viscosimeter)	mPas	16–18
pH	–	9.5
Filtration	mL/30 min	9.8–10

Rock Material Properties

The rock material we drilled through was regularly sampled from drilling fluid. Each rock sample was examined and compared to a predetermined lithological column based on the results of geophysical and laboratory measurements in the surrounding boreholes.

As far as the lithology of the material of the drilled interval concerned, silty claystone is dominant and layers of carbonatic siltstone with sandstone plates and thin layers of clay and limestone occur in the lower and upper parts of the sequence.

The geomechanical properties of the drilled borehole section were evaluated based on experience. The strength properties were evaluated using the Hoek-Brown's criterion using RockScience software, Rock Lab 1.0.

The estimated rock properties values for the carbonate silt are shown in Table 3.

The estimated rock properties values for limestone are shown in Table 4.

Table 3. *Results of the rock properties – carbonatic siltstone*

Parameters	Units	Value
Cohesion	MPa	0.722
Elastic module	MPa	9375
Angle of internal friction	°	20.94
Compressive strength	MPa	25

Table 4. *Results of the rock properties – limestone*

Parameters	Units	Value
Cohesion	MPa	5.50
Elastic module	MPa	28125
Angle of internal friction	°	38.42
Compressive strength	MPa	75

Roller Cone Bit Investigation

After drilling and cleaning, the drill bit was examined using the IADC dull grading system. We found that the teeth of the drill bit were evenly worn out and several individual teeth were broken. There are no obvious erosion effects due to the rock particles in the drilling fluid that would result in erosion of the steel material of the bit. The condition of roller cone bit after the length of drilled interval of 87.89 m is shown by Figure 1.

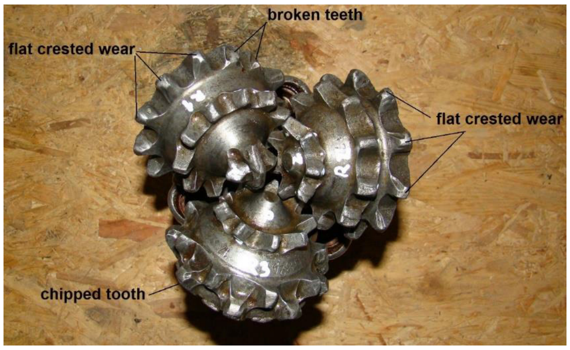

Figure 1. *Characteristic dull of the roller cone bit after drilled interval.*

Investigations of Tooth Steel Material

We examined the steel material and the carbide coating of the teeth.

The investigation of the chemical composition of the teeth material was carried out with an optical emission spectrometer (ICP). The results of the chemical composition of the examined steel (body) are shown in Table 5.

Table 5. *Chemical analysis of the tooth material – body*

Elements	Mas. %
Mn	0.79
Ni	0.74
Cr	0.60
Mo	0.50
Cu	0.27
Si	0.26
C	0.17
S	0.016
P	0.011

The results of the chemical analysis (Table 5) show that the steel material of the tooth body in this case is chromium, molybdenum, nickel low alloy steel, which is often used for case-hardened parts.

At SEM, we analysed metallographically the steel base of the tooth (chromium, molybdenum, nickel low alloy steel), the contact area between the tooth body and the carbide coating and the carbide coating itself. We have determined the chemical composition of the steel of each component of the tooth through the analysis of EDS. Figure 2 (SEM) shows the areas where metallographic tests are performed on the teeth. Tables 6–9 show the results of the EDS analyses for each component analysed.

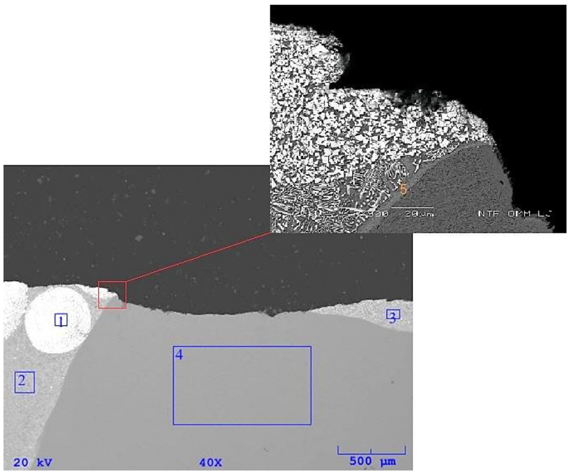

Figure 2. *Scanning electron microscope (SEM) image of tip of the bit tooth. Position 1 – carbide material; Positions 2 and 3 – carbide coating matrix; Position 4 – tooth body and Position 5 – mixed zone.*

Table 6. *The elemental composition of carbide coating material (Figure 2 – Position 1)*

Elements	Concentration	
	at.%	wt.%
W	55.415	79.539
Co	42.380	19.500
Fe	0.807	0.962

Table 7. *The elemental composition of the carbide coating matrix (Figure 2 – Position 2)*

Elements	Concentration	
	at.%	wt.%
Fe	86.096	68.599
W	1.709	29.094
Ni	1.921	1.608
Mn	0.892	0.699

Table 8. *The elemental composition of the carbide coating matrix (Figure 2 – Position 3)*

Elements	Concentration	
	at.%	wt.%
Fe	86.117	68.616
W	11.103	29.124
Ni	1.511	1.265
Mn	1.269	0.995

Table 9. *The elemental composition of the tooth body (Figure 2 – Position 4)*

Elements	Concentration	
	at.%	wt.%
Fe	95.427	95.385
Ni	3.164	3.323
Mn	0.660	0.649
Mo	0.218	0.375
Si	0.531	0.267

The elemental composition of the carbide coating material (Figure 2 – Position 1), which is determined by EDS, is shown in Table 6.

The elemental composition of the carbide coating matrix (Figure 2 – Position 2), which is determined by EDS, is shown in Table 7.

The elemental composition of the carbide coating matrix (Figure 2 – Position 3), which is determined by EDS, is shown in Table 8.

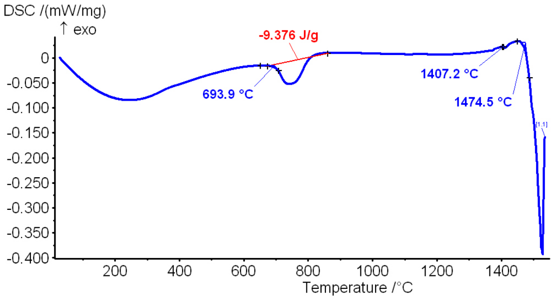

Figure 3. *DSC heating curve of the steel of the tooth body.*

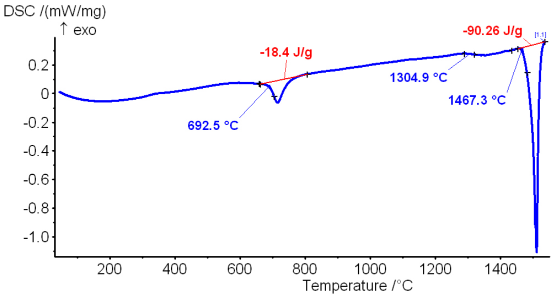

Figure 4. *DSC heating curve of carbide coating.*

The elemental composition of the tooth body (Figure 2 – Position 4), which is determined by EDS, is shown in Table 9.

We carried out a simultaneous thermal analysis (STA) (Figure 3) of the steel sample of the tooth body. The curve shows that eutectoid transformation in the solid state starts at a temperature of 693.9°C and also there is an endothermic peak. The process ends at 800°C when the metal matrix (iron) is transformed into a gamma-phase iron structure – austenite (g-Fe). The temperature 1407.2°C is the low temperature at which the eutectic structure or alloy begins to melt. The remaining material of the metal matrix (austenite) begins to melt at 1474.5°C. The temperature of 1474.5°C is also the solidus temperature of the steel from which the tooth body is made.

The DSC (Differential scanning calorimetry) heating curve of the carbide coating of the teeth in the roller cone bit is shown in Figure 4. The carbide coating contains a thin layer of the mixing zone. The mixing zone is the area formed during the welding of the carbide coating to the tooth. It contains the properties of the steel of the tooth body and the carbide coating. At the

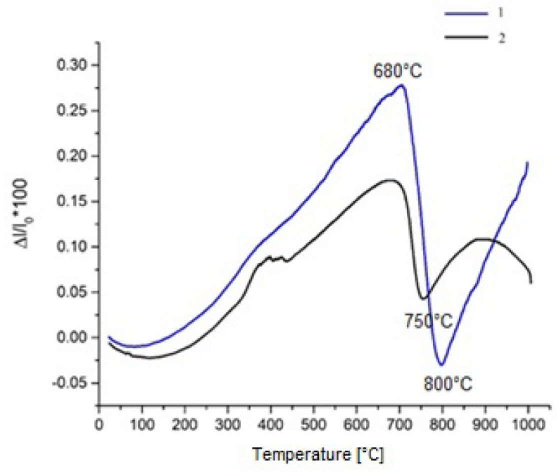

Figure 5. *Dilatometric heating curve of the steel of the carbide coating and the steel of the tooth: 1 – tooth steel material (blue), 2 – carbide coating (black).*

Table 10. *Results of the Vickers hardness test*

Diagonals (mm)		Hardness (HV0.5)	Average	Note
d1	d2			
37.23	46.24	532.3198	594.5670	Tip of the tooth
36.22	37.55	681.5125		
36.4	40.81	622.1374		
37.99	41.33	589.4786		
37.54	41.66	591.2662		
37.43	39.54	626.0232		
37.57	39.86	618.6071		
36.33	42.41	598.1947		
38.87	42.45	560.8396		
38.48	42.45	566.2580		
39.01	42.84	553.6000		
44.99	47.95	429.3664	433.5184	Tooth body
44.44	48.37	430.5701		
44.61	47.78	434.4937		
44.09	47.10	446.0042		
45.14	48.04	427.1575		
33.28	37.13	748.1087	784.1543	Carbide coating—matrix
31.73	34.04	857.3887		
33.64	36.53	753.2349		
34.58	36.51	733.8654		
30.41	36.51	828.1739		
24.67	25.96	1446.830	1458.984	Carbide coating—base
24.43	25.78	1471.137		

temperature 692.5°C, the starting of the eutectoid transformation was detected. This transformation is related to the layer of the mixed zone. Therefore, this curve is not typical for carbide alloys. At the temperature of 1467.3°C, the starting of melting process was detected.

Figure 5 shows the dilatometric curve of the steel of the carbide coating and the steel of the tooth body. It can be seen from the heating curve of the steel of the tooth body that the temperature of the eutectoid transformation increases linearly. The slope of the curve corresponds to the linear expansion coefficient for chromium, molybdenum and nickel low alloy steel, while the slope of the heating curve of the sample of the carbide coating containing a thin layer of the mixing zone is small. A lower curve angle of the carbide coating sample containing a thin layer of the mixing zone is the result of a lower coefficient of thermal expansion.

In view of the fact that the temperatures can locally reach up to 500°C during drilling despite intensive cooling, the curves show that the difference between the expansion properties is 0.05%. Because of this difference, the mixing zone is the preferred area for the formation of internal stresses and hence suitable for the formation and propagation of micro-fractures. The diagram shows the beginning of the eutectoid transformation of the tooth body steel sample, which starts at 680°C (A_{c1}) and ends at a temperature of 800°C (A_{c3}). For the carbide coating sample containing a thin layer of the mixed zone, eutectoid transformation starts at 750°C. On the curve of the carbide coating sample containing a thin layer of the mixing zone, a deviation is observed which can be associated with the eutectoid transformation of the thin layer of the mixing zone, but the temperature is slightly higher. The reason for this higher temperature is due to the chemical composition of the mixing zone.

A Vickers hardness test was performed to determine the changes in the hardness properties of the tooth due to the effects of drilling. The measurement points are shown in Figure 6 and the results of the tests are shown in Table 10. The average hardness of the steel of the tooth body is 433.5184 HV. The average hardness of

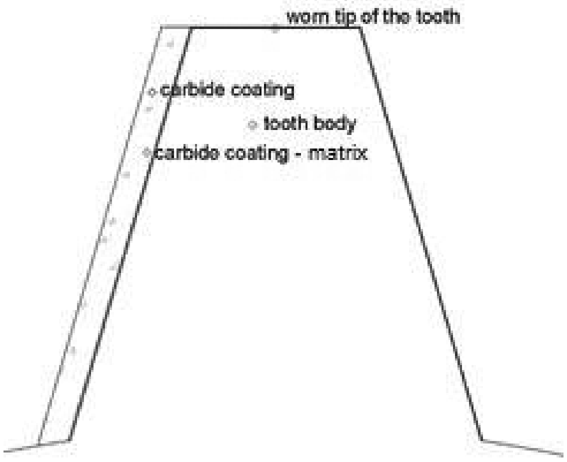

Figure 6. *Display of measurement positions of Vickers hardness tests.*

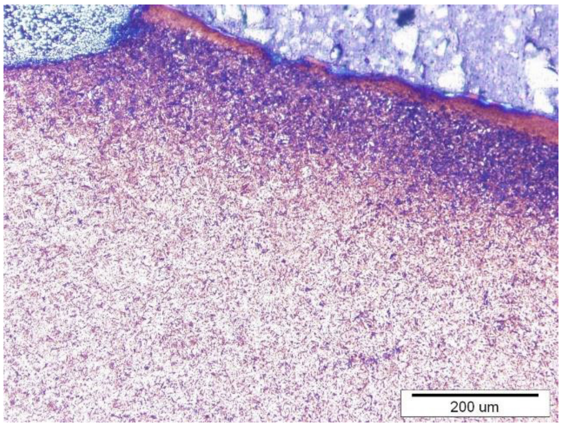

Figure 7. *Microscopic photo of the tip of the tooth.*

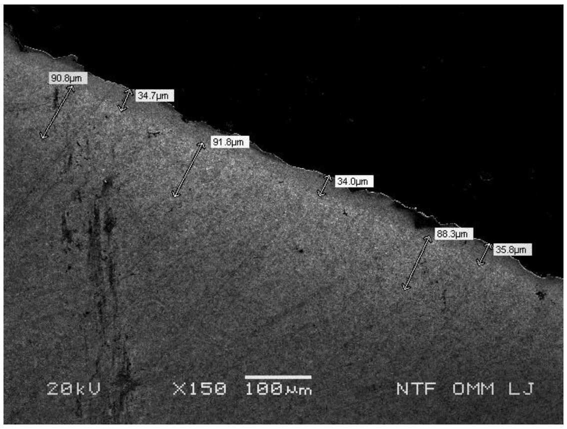

Figure 8. *A view at the tip of tooth that was in contact with the rock.*

the steel at the tip of the teeth is much higher and is 594.5670 HV. The hardness of the carbide coating is, as expected, much higher and reaches up to 1471,137 HV.

Discussion

Monitoring of the operating parameters during drilling revealed that the roller cone bit was not loaded in accordance with the manufacturer's recommendations, which recommends that the bit load should be in the range of 15–27 kN. The load on the bit during drilling was between 30 kN and 40 kN. In addition, the number of bit rotations was too low and they were between 35 rpm and 45 rpm. The recommended number of bit rotations for this type of tool is between 60 rpm and 100 rpm.

It can be noted that the bit was overloaded with weight and the number of bit rotations was too low.

Examination of the microscopic image showed that the tips of the teeth were exposed to high temperatures and stresses. The influence of high temperatures and loads is shown in Figure 7.

Figure 7 shows the tip of the tooth that was in contact with the rock. We can see changes in the colour of the steel, which changes from blue tones (at the point of contact between the rock and the steel) to brown tones that change the light from top to bottom.

Because of the apparent colour change previously observed under the optical microscope, the sample was examined with a scanning electron microscope (SEM). A characteristic view of the microstructure of the area with a SEM is shown in Figure 8.

Figure 8 shows the condition of the tooth tip that was in contact with the rock during drilling. A change in the microstructure of the steel on the surface was observed. The change in the steel structure can be observed in two layers. The first layer, where the change is noticeable, is up to a thickness of 36 µm. The second layer, in which the change in microstructure is less pronounced but still noticeable, moves to a depth of up to 92 µm.

The change in the steel microstructure of the tooth was due to the high temperatures and mechanical stresses that occurred during drilling when the tip of the tooth was in contact with the rock. When the roller cone bit is rotated around its axis, the teeth got cooled. The teeth that were not in contact with the rock were cooled by the drilling fluid flowing out from the nozzles of the bit. In this situation, a temperature change occurs on the surface of the teeth when their temperature is very high and they are washed with drilling fluid at a lower temperature. The other reason for microstructural changes in the steel is that the bit was overloaded during drilling and the number of revolutions was too low when compared to the load. The consequence of such a drilling regime is the increase in temperature of the material at the tooth tip, which in combination with the load results in the hardening of the material at the tooth tip. Because of this reason the hardness of the steel material increased. The measured hardness (Vickers hardness) at that time was on average about 160 HV higher than the hardness of the steel material in the middle of the tooth.

Using differential scanning calorimetry (DSC), we found that the temperature of the eutectoid point is 699.2°C and its completion occurs at a temperature of 800°C. Due to the intensive cooling of the teeth under the influence of the drilling fluid, the microstructural change process occurred only in the steel layer down to a depth of 92 μm. Microstructural changes are only noticeable on the upper side of the teeth, while no changes were observed on the sides.

The changes in the steel structure occurred mainly due to excessive operating temperatures and loads on the selected steel. As demonstrated by DSC and dilatometric analysis, the temperature at the beginning of the transformation from ferrite to austenite is about 680°C for the selected steel. This means that the temperature of 680°C (A_{c1}) is a point at which recrystallisation of the steel is rapidly accelerated. The recrystallisation temperature for steel, when calculated for theoretical information, is somewhere around 0.4 × T_L (T_L – liquidus temperature, °C) [25]. Using the software Thermo-Calc for thermodynamic modelling of the equilibrium phase, we calculated the liquidus temperature, which was 1511°C for the selected steel. Therefore, the recrystallisation temperature for the analysed steel is about 604°C. We also calculated the equilibrium eutectoid temperature A_{e1} and the transition temperature A_{e3} with the same software. The temperature of t6he former was 685°C and the latter was 811°C. The equilibrium eutectoid temperature A_{e1} and the transition temperature A_{e3} were also calculated. The calculated values are similar to the values obtained from the dilatometric analysis of the steel (680°C and 800°C), assuming that the temperatures obtained from the calculation are in equilibrium. This confirmed the results of the dilatometric analysis.

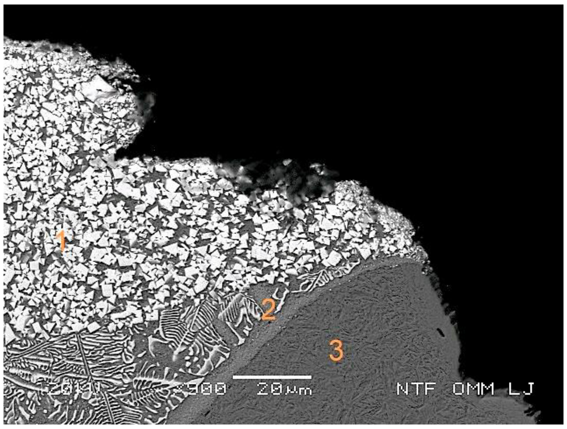

Figure 9. *Photography of tooth steel material. Position 1 – carbide coating; Position 2 – mixed zone and Position 3 – tooth steel (body).*

Due to the influence of high temperatures and rapid cooling, the carbide coating on the upper surface of the tooth gets decayed. The difference between the temperature-expansibility coefficients of the steel material and the carbide form was found by a dilatometric test at low temperature. This difference is significant as it causes increase in internal stress in the mixed zone. The mixed zone is formed by welding the carbide coating onto the tooth steel and represents a mixture of dissolved steel material of the tooth and the carbide coating (Figure 9). In the mixed zone, during the heating and cooling processes, internal stresses begin to increase due to the different temperature coefficients of the materials, which lead to initiation and propagation of cracks.

Cracks were observed on the edges of the teeth, which progressed through the carbide coating to the steel of the tooth (body) (Figure 10). The occurrence of such cracks can be attributed

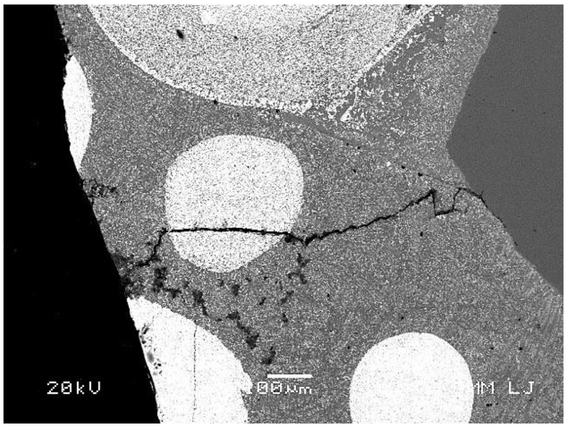

Figure 10. *Photography of cracks through carbide coating.*

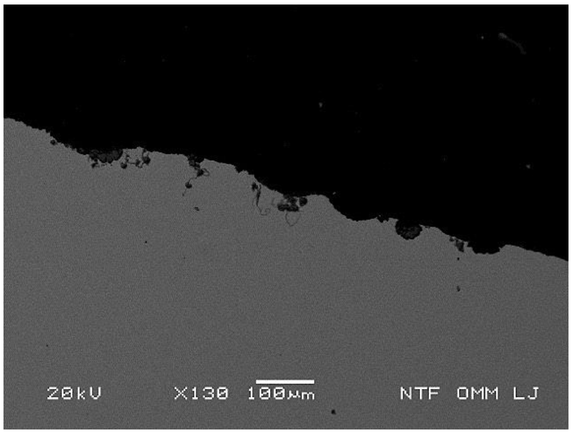

Figure 11. *Erosion channels at the top of the tooth.*

to the excessive load on the bit during drilling and the stress accumulation due to the weight load of the bit. The carbide coating is tough and erosion resistant, but brittle, which causes it to crack under excessive load and lateral forces. Due to the formation of such cracks at the tooth edges, the carbide coating is sheared or eroded, which resulted in a chipped tooth.

The erosion effect caused by aggressive particles in the drilling fluid could not be expressed comprehensively so far, as only a short length of 87.89 m was drilled with this drill bit. Microscopic images show smaller erosion microchannels, which are not largely pronounced (Figure 11). Erosion microchannels occur only in the area of the tooth tip. There are no erosion channels along the tooth edges that are not protected by carbide coatings, which is partly due to the geometry of the teeth. Here, the teeth sides are quite steep, which means that the drilling fluid with abrasive particles leaves the tooth area within a short time.

Conclusions

In this article, we have described the wear of the IADC 136 roller cone bit drilled into a known standard rock material. The bit wear was characterised by the analysis of the different metallurgical properties of the steel and the carbide coating of the teeth of the bit, which are related to the drilling regime and the properties of the rock material. During drilling, the teeth of the bit are heated when are in contact with the rock and then cooled by the influence of the drilling fluid. At this stage, there is a compressive load on both the steel of the tooth and its carbide coating. Internal stresses developed in the materials of the bit teeth due to the load on the bit can expand through the elastic zone and reach the plastic zone, which results in local dissolution of the carbide coating and a local increase in the hardness of the steel material.

Using an IADC 136 roller cone bit, the length of interval 87.89 m was drilled into a carbonatic siltstone with sandstone plates and thin layers of clay and limestone. The wear of the teeth of the roller cone bit was mainly observed at the tooth tip. During the systematic investigation of the steel structure of the teeth and the carbide coating, it was found that the structure of the steel material at the tip of the teeth was partially changed by the influence of high deformations. This change, which was reflected in the increase in the hardness of the steel material, was higher at the tip of the tooth which is in contact with the rock by 160 HV than at the tooth body. The change in the hardness of the steel material, expressed as a layer parallel to the tooth tip, extends to a depth of about 36 mm. The formation of this layer with a higher degree of hardness can be explained by the implementation of the weight on the drill bit (WOB), which was higher than the recommended and relatively low rotation (RPM), and it was lower than the recommended. The increase in the temperature of the tooth material during drilling was due to excessive loads and inefficient cooling, resulting in micro-fatigue reaching the plastic zone of the steel material at the tip of the tooth. The tip of the tooth was worn out by a modified microstructure due to friction along the rock, and underneath it, a new layer with a modified microstructure formed periodically. From this, it can be concluded that the correct choice of roller cone bit can be recommended for a specified type of rock and operating parameters (WOB, RPM, drilling fluid) since it has a significant influence on the wear of the roller cone bit and thus on the extension or reduction of the effective operating time of the roller cone bit.

The results of our investigation of the materials of the roller cone bits can provide a base and guidelines for the development of new steel alloys that can withstand higher temperatures and allow effective drilling without structural changes in the steel material.

References

[1] Al-Sudani, J.A. (2017): Real-time monitoring of mechanical specific energy and bit wear using control engineering systems. *Journal of Petroleum Science and Engineering*, 149, pp. 171–182, DOI: 10.1016/j.petrol.2016.10.038.

[2] Bingham, M.G. (1965): *A New Approach to Interpreting Rock Drillability*. Petroleum Publishing Co.: Tulsa, OK, USA, 93 p.

[3] Cheatham, J.B. (1958): An analytical study of rock penetration by a single bit tooth. In*: Proceedings of the 8th Drilling and Blasting Symposium*, Minnesota, MN, USA.

[4] Dagrain, F., Lamine, E., Delwiche, R., Golard, N. (2013): Characterization of the performances of small diameter drill bits for the optimization of the drilling parameters. In: *Proceedings of the 2nd International Conference on Stone and Concrete Machining (ICSCM)*, Dortmund, Germany.

[5] Dutta, P.K. (1972): A theory of percussive drill bit penetration. *International Journal of Rock Mechanics and Mining Sciences & Geomechanics Abstracts,* 9, pp. 543–567, DOI: 10.1016/0148-9062(72)90044-7.

[6] Eremin, E.N., Yurov, V.M., Guchenko, S.A., Laurynas, V.C., Kasymov, S.S. (2016): Antifriction Superhard Coatings for Drill Bits and Boring Cutters. *Procedia Engineering,* 152, pp. 608–612, DOI: 10.1016/j.proeng.2016.07.663.

[7] Evans, I., Murrell, S. (1962): Wedge penetration into coal. *Colliery Engineering*, 39, 11.

[8] He, W., Chen, Y., He, J., Xiong, W., Tang, T., OuYang, H. (2016): Spherical contact mechanical analysis of roller cone drill bits journal bearing. *Petroleum*, 2, pp. 208–214, DOI: 10.1016/j.petlm.2016.03.002.

[9] Jones, H.G., Norgren, S.M., Kritikos, M., Mingard, K.P., Gee, M.G. (2017): Examination of wear damage to rock-mining hardmetal drill bits. *International Journal of Refractory Metals and Hard Materials*, 66, pp. 1–10, DOI: 10.1016/j.ijrmhm.2017.01.013.

[10] Karasawa, H., Ohno, T., Miyazaki, K., Eko, A. (2016): Experimental results on the effect of Bit wear on torque response. *International Journal of Rock Mechanics and Mining Sciences*, 84, pp. 1–9, DOI: 10.1016/j.ijrmms.2016.01.013.

[11] Ma, D.K., Yang, S.L. (1985): Kinematics of the Cone Bit. *Society of Petroleum Engineers Journal*, 25, pp. 321–329, DOI: 10.2118/10563-PA.

[12] Maurer, W.C. (1965): Bit-Tooth Penetration Under Simulated Borehole Conditions. *Journal of Petroleum Technology*, 17, pp. 1433–1442, DOI: 10.2118/1260-PA.

[13] Naganawa, S. (2005): Dynamics modeling of roller cone bit axial vibration. *Journal of the Japanese Association for Petroleum Technology*, 70, pp. 333–346, DOI: 10.3720/japt.70.333.

[14] Naganawa, S. (2012): Feasibility study on roller-cone bit wear detection from axial bit vibration. *Journal of Petroleum Science and Engineering*, 82–83, pp. 140–150, DOI: 10.1016/j.petrol.2012.01.014.

[15] Njobuenwu, D.O., Wobo, C.A. (2007): Effect of drilled solids on drilling rate and performance. *Journal of Petroleum Science and Engineering*, 55, pp. 271–276, DOI: 10.1016/j.petrol.2006.08.012.

[16] Olsson, M., Yvell, K., Heinrichs, J., Bengtsson, M., Jacobson, S. (2017): Surface degradation mechanisms of cemented carbide drill buttons in iron ore rock drilling. *Wear*, 388–389, pp. 81–92, DOI: 10.1016/j.wear.2017.03.004.

[17] Paul, B., Sikarskie, D.L. (1965): A preliminary model for wedge penetration in brittle materials. *Transactions of the American Institute of Mining Engineers*, 232, pp. 373–383.

[18] Warren, T.M. (1981): Drilling Model for Soft-Formation Bits. *Journal of Petroleum Technology*, 33, pp. 963–970, DOI: 10.2118/8438-PA.

[19] Warren, T.M. (1987): Penetration Rate Performance of Roller Cone Bits. *Society of Petroleum Engineers*, *2*, pp. 9–18, DOI: 10.2118/13259-PA.

[20] Zhao, J., Zhang, G., Xu, Y., Wang, R., Zhou, W., Yang, D. (2018): Experimental and theoretical evaluation of solid particle erosion in an internal flow passage within a drilling bit. *Journal of Petroleum Science and Engineering*, 160, pp. 582–596, DOI: 10.1016/j.petrol.2017.10.068.

[21] Hareland, G., Wu, A., Rashidi, B.A. (2010): New Drilling Rate Model for Tricone Bit and Its Application to Predict Rock Compressive Strength. In: *44th US Rock Mechanic Symposium and 5th U.S.-Canada Rock Mechanics Symposium*, Salt Lake City, UT, USA.

[22] Rashidi, B., Hareland, G., Wu, Z. (2015): Performance, simulation and field application modeling of rollercone bits. *Journal of Petroleum Science and Engineering*, 133, pp. 507–517, DOI: 10.1016/j.petrol.2015.06.003.

[23] Bourgoyne, A.T., Young, F.S. (1974): A Multiple Regression Approach to Optimal Drilling and Abnormal Pressure Detection. *Society of Petroleum Engineers Journal*, 14, pp. 371–384, DOI: 10.2118/4238-PA.

[24] Bourgoyne, A.T., Millheim, K.K., Chenevert, M.E., Young, F.S. (1991): Rotary Drilling Bits. In: *Applied Drilling Engineering*. SPE: Richardson, TX, USA, pp. 190–245.

[25] Totten, G.E. (2006): *Steel Heat Treatment: Metallurgy and Technologies*, 2nd ed. CRC Press: Boca Raton, Florida, USA, 848 p.

Review paper

Received: Aug 17, 2020
Accepted: Sep 07, 2020
DOI: 10.2478/rmzmag-2020-0012

Laboratory Test Methods for Assessing the Abrasivity of Rocks and Soils in Geotechnology and Mining Applications

Laboratorijske preiskave abrazivnosti kamnin in zemljin na področju geotehnologije in rudarstva

B. Janc*, V. Jovičić, Ž. Vukelić
University of Ljubljana, Faculty of Natural Sciences and Engineering, Department of Geotechnology, Mining and Environment, Aškerčeva 12, Ljubljana, Slovenia
* blaz.janc@ntf.uni-lj.si

Abstract

In geotechnology and mining, tools and equipment interact with aggressive geological material, causing the wear of these components. For this reason, it is important to determine the rate of abrasivity of individual geological materials, depending on the type of interaction with the tool. Various abrasivity tests have been developed in laboratories. Some of them are general, while others are special. What they all have in common is that they attempt to determine the abrasivity of rocks or soils in relation to the wear of the test specimens. This article gives an overview of the laboratory test methods for assessing the abrasivity of geological materials, which are useful in the field of geotechnology and mining engineering. General and special abrasivity tests are presented in detail. The aim of the article is to present existing laboratory tests to assess the abrasivity of rocks and soils, based on which further investigations of wear can be considered as part of a comprehensive approach to this tribological problem. Understanding of the wear mechanisms is the basis for the development of wear-resistant tools and models for predicting the tool life.

Key words: laboratory testing, abrasivity, wear, geotechnology, mining.

Povzetek

V geotehnologiji in rudarstvu so orodja in oprema v interakciji z agresivnim geološkim materialom, ki povzroča obrabo omenjenih komponent. Zaradi tega obstaja težnja po določevanju stopnje abrazivnosti posameznih geoloških materialov glede na vrsto interakcije z orodjem. V laboratorijih so bile razvite različne preiskave abrazivnosti. Ene od njih so splošne, druge namenske. Vsem pa je skupno to, da skušajo določiti abrazivnost kamnin ali zemljin glede na obrabo preizkušanca. V članku je predstavljen pregled laboratorijskih preiskav abrazivnosti geoloških materialov, ki so uporabne na področju geotehnologije in rudarstva. Splošne in namenske preiskave abrazivnosti so podrobno predstavljene. Namen članka je predstaviti obstoječe laboratorijske preiskave abrazivnosti kamnin in zemljin, na podlagi katerih je mogoče nadaljnje preiskovanje obrabe kot del celovitega pristopa pri tem tribološkem problemu. Razumevanje mehanizmov obrabe je podlaga za razvijanje orodij, odpornih proti obrabi ter modelov za napovedovanje njihove življenjske dobe.

Ključne besede: laboratorijsko preiskovanje, abrazivnost, obraba, geotehnologija, rudarstvo

Introduction

Geotechnology as an engineering discipline is confronted with many cases in which tools and equipment in dynamic contact with geological material get worn out. They are exposed to high compression, shear and impact loads. The result of these loads is material damage to the tools and equipment used in the technological process, which gradually reduces their functionality.

The areas of geotechnology where the wear of tools and equipment are most pronounced (Figure 1) can be divided into the following four main groups:

1) Tunnelling
2) Drilling
3) Mining
4) Mineral processing

The first group includes the tunnelling sector, which deals with the construction of road and rail tunnels, as well as tunnels for water transport and sewerage. Tunnelling can be carried out conventionally by drilling and blasting or mechanised with tunnel boring machines (TBMs) or excavation machines (roadheaders). Both the excavation methods lead to tool wear. In the conventional method, the drill bits are worn out when drilling boreholes, whereas in the mechanised method the disc cutters on the TBM or the teeth on the head of the excavation machine (roadheader) are worn out.

The second group includes the drilling sector, which deals with the drilling of production, exploratory or technical boreholes. Production wells are intended for the production of minerals and energy, such as oil, gas and geothermal energy. Exploratory boreholes are used for geological–geomechanical investigations. Technical boreholes are used for rock blasting and anchoring geotechnical constructions. All these operations, during which percussion or rotary drilling is performed, cause wear on the teeth or inserts of the drill bits, which are the main tool for drilling boreholes.

The third group includes the mining sector, which deals with the surface or underground extraction of mineral resources, including metals, non-metals and energy resources. In the mining sector, wear occurs mainly in two areas: the extraction and transport sectors. In the extraction sector, tools are worn on mechanised mining excavation machines such as the longwall shearer, continuous miner and bucket wheel excavator. In the transport sector, wear occurs on transport machines and equipment.

The fourth group includes the mineral processing sector, which deals with the processing and preparation of mineral resources for use in various industrial processes. Most pronounced is the wear of equipment used to increase the specific surface area of the mineral resources. This includes crushing and grinding machines. Wear occurs on parts of the equipment that are in contact with the mineral. These are usually plates in various crushers and grinding media in mills.

In all the four groups described above, it is possible to find the occurrence of material wear that forms a tool or equipment that is in dynamic contact with geological material. In most cases, the materials of the tools and equipment are steels which, due to their wide availability and economic acceptance, currently have the most suitable wear resistance.

Abrasivity and Tribological System

Abrasivity plays an important role in the process of wear. It is a property that reflects the ability of a rock (geological material) to cause wear on materials [1]. The tribological system combines all components necessary for the wear process. These components are as follows:

1) Geological material
2) Tool material
3) Surrounding medium
4) Type of load (dynamic interaction)

A change in any of the above components also changes the mode and rate of wear. Figure 2 schematically shows a tribological system with all four components.

There are several methods for estimating the abrasivity of rocks and soils. In general, three categories can be distinguished [2]:

1) Indirect methods – assessment of abrasivity by a combination of different geomechanical properties such as hardness, uniaxial compressive strength, tensile strength and other fundamental properties.

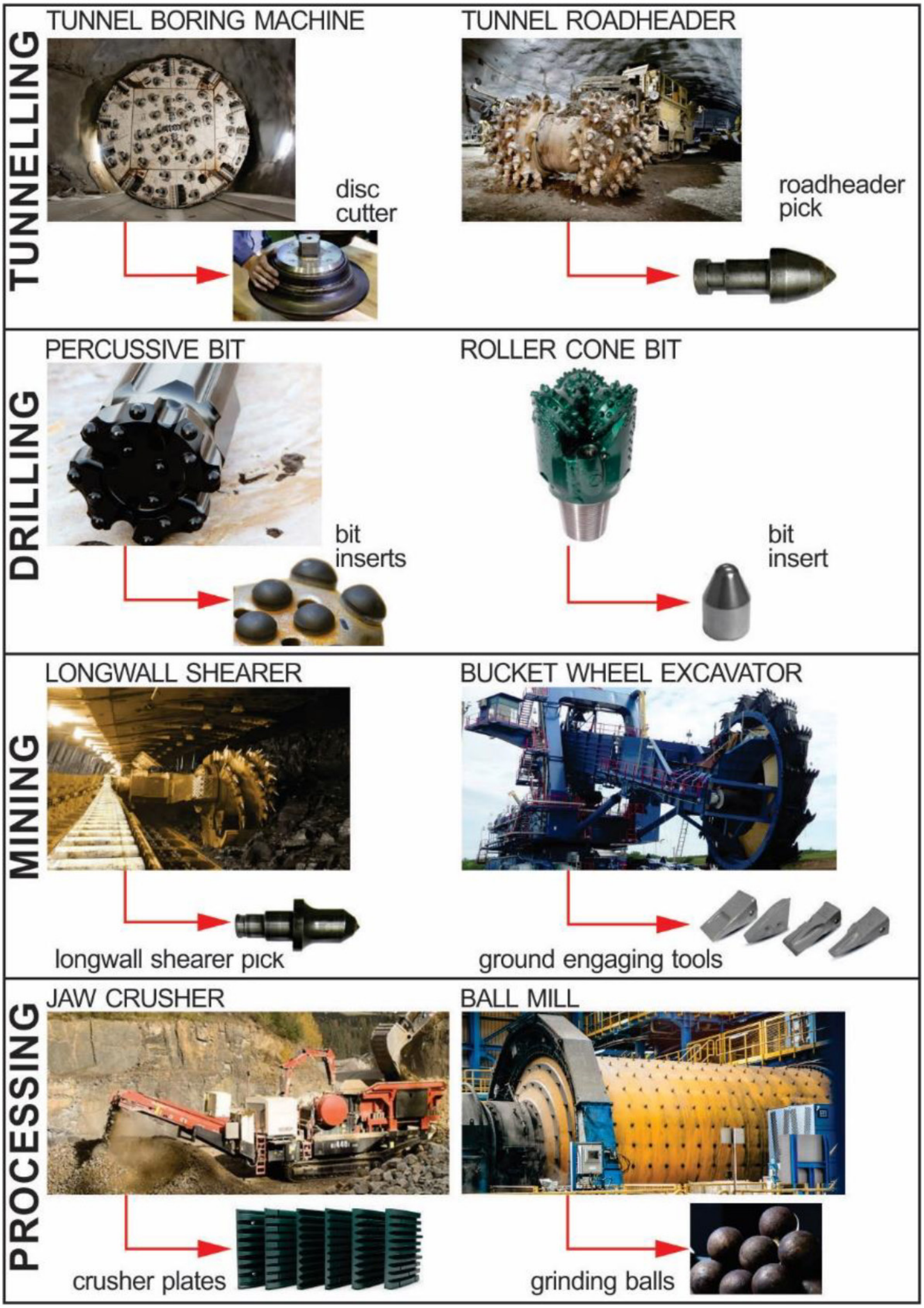

Figure 1: *Wear of tools in geotechnology and mining engineering. The most typical devices for each field are shown (adapted from [3–16]).*

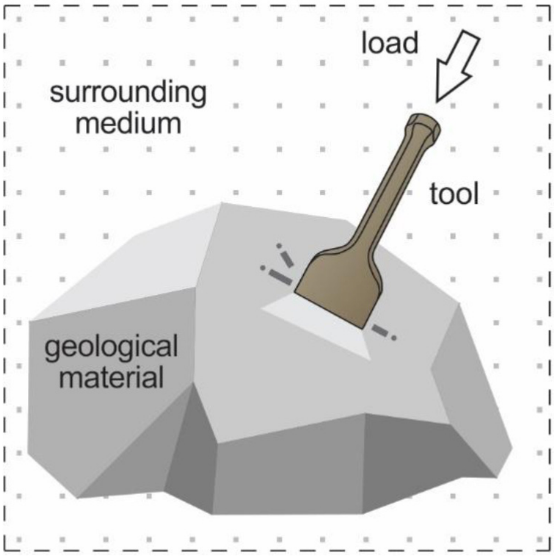

Figure 2: *Tribological system (schematic).*

2) Direct methods – assessment of abrasivity by laboratory test methods where there is relative movement between the geological sample and the wear tool in contact under the influence of controlled standard conditions.
3) Holistic methods – assessment of abrasivity by a combination of the fundamental geomechanical properties of the geological material and other parameters of the process and environment in which the wear occurs.

Indirect methods for assessing abrasivity have the advantage of using data that are already available or are relatively easy to obtain. However, they do not take into account the process variables for certain types of wear. Therefore, they are usually not used individually but in combination with direct or holistic methods.

The holistic methods for assessing abrasivity are very much related to certain equipment and processes and, therefore, have less value for other applications.

The direct methods for assessing abrasivity use the standard conditions to determine the abrasivity for a specific type of wear, either low or high stress or impact abrasion. The tests investigate the effects of relative movements between the geological sample and a wear tool in contact [2].

Laboratory Test Methods for Assessing the Abrasivity of Geological Material

Researchers have developed various laboratory devices to test the abrasivity of individual rocks and soils directly in the laboratory. The test methods differ depending on the design of the device or apparatus, the duration of the test, the method of causing wear, the shape and size of the abrasive material and the wear tool, and the purpose of the test. Some abrasivity tests are general and standardised to some extent. However, most of the tests are special and were intentionally developed for certain technological processes described in the introductory part of this article. It is worth noting that by far the largest number of abrasivity tests have been developed for mechanised tunnelling.

A general test method for assessing the abrasivity of geological material includes the CERCHAR abrasivity test for rocks and the LCPC abrasivity test for soils or grain materials. Both tests have been developed in France and are standardised. Special test methods for assessing the abrasivity of geological material are those developed for a specific application, such as tunnelling, drilling and mineral processing. The group of tests for tunnelling includes NTNU/SINTEF (AV, AVS and SAT™) and RIAT (rolling indentation abrasion test) abrasivity tests, which were developed for the estimation of tool wear in mechanised tunnelling. These abrasivity tests are not yet standardised. Miller abrasive test is used to determine the abrasivity of slurries and is standardised (ASTM G75 standard). The Gouging abrasion test can be used to estimate the wear of machine parts during crushing and grinding processes. The test is not standardised. It is also worth mentioning some other abrasivity tests that fall within the field of road construction. These are the (standardised) Los Angeles abrasion test, the Nordic ball mill test and the Dorry abrasion test, which all test the wear resistance of road aggregates.

CERCHAR Abrasivity Test

The CERCHAR abrasivity test was originally developed by a French laboratory (Laboratoire du Center d’Etudes et Recherches des Charbonnages de France) for mechanised coal mining.

This method is described by two standards, the French standard AFNOR NF P 94-430-1 and the International standard ASTM D7625-10 [17].

Apparatus

There are two types of testing apparatus. The first is the original design as developed at the CERCHAR centre and the second is a modified design as reported by West [17].

In the CERCHAR apparatus (Figure 3), the loaded stylus moves across the surface of a stationary rock sample. In the case of the West design (Figure 4), however, the rock sample moves under the loaded stationary stylus. Different implementations of the apparatus design lead to a test duration [17].

Both apparatus have a rigid vice for firmly clamping the rock sample. Sufficient rigidity of the apparatus ensures that there is no lateral movement during the test. The stylus is loaded with a weight of 70 N [17].

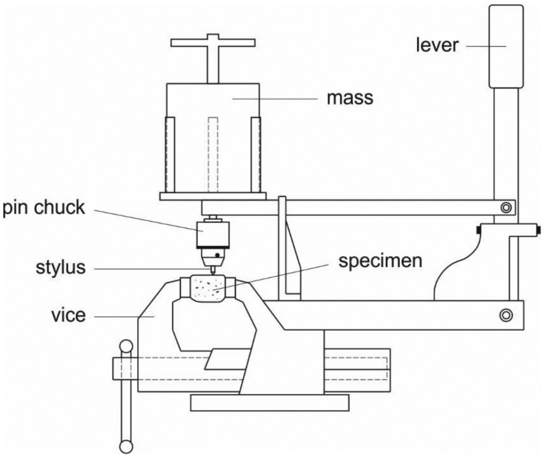

Figure 3: *CERCHAR-type testing apparatus (adapted from [17]).*

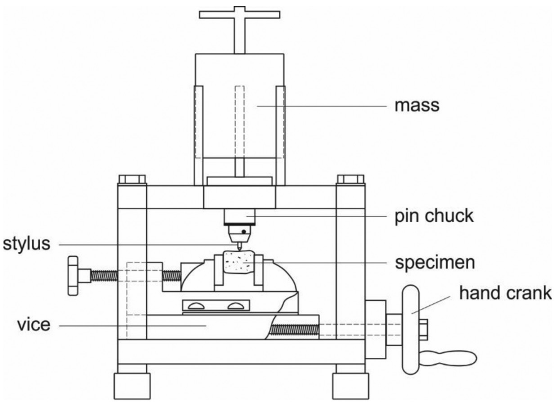

Figure 4: *West-type testing apparatus (adapted from [17]).*

Stylus

The stylus is made of standard chrome–vanadium cold-work tool steel and is hardened to Rockwell hardness HRC 55 ± 1. The stylus diameter should be at least 6 mm. The length of the stylus should be such that the visible part of the stylus between the pin chuck and the surface of the rock sample is at least 15 mm. The pin of the stylus (Figure 5) has a conical shape with an angle of 90°. The worn pin should be resharpened and examined under a microscope before being used for further testing [17].

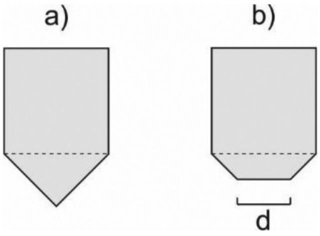

Figure 5: *Steel pin. (a) Before the test. (b) After the test (d is the wear flat) (adapted from [18]).*

Test Sample

The rock sample can be circular or irregularly shaped. A test on freshly broken rock surface is recommended. The rough surface can be obtained by a Brazilian tensile test (Figure 6) on the rock disc or by firm hammer blows on a rock core or rock sample. Alternatively, the sample can be prepared with a water-cooled diamond saw blade. The surface to be tested should be cleared of debris or loose grains of rock. The size of the rock surface should be suf-

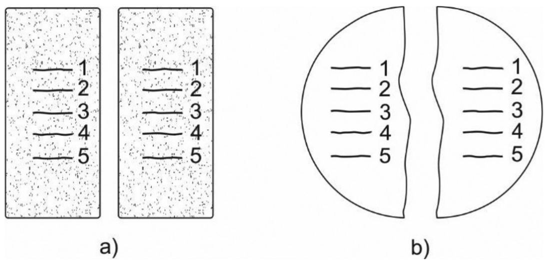

Figure 6: *The two halves of the sample disc with test scratches (1–5) after Brazilian tensile test. (a) Rough surface. (b) Smooth surface (adapted from [20]).*

ficient to allow five test scratches at a minimum distance of 5 mm and 5 mm from the edge of the rock surface [17].

Test Procedure

A microscopic inspection of the stylus should be performed before the test. The rock sample should be firmly clamped in the vice with the rock surface as horizontal as possible. The stylus should be carefully lowered onto the rock surface. The length of a test scratch in the rock sample must be exactly 10 mm. Depending on the apparatus design used, the test duration is 1 (CERCHAR version) or 10 s (West version). The stylus pin must be in constant contact with the rock surface during the test [17]. The main parameters of the CERCHAR abrasivity test are summarised in Table 1.

Table 1: *Main parameters of the CERCHAR abrasivity test.*

Parameters	Value	
Load (N)	70	
Stylus hardness (HRC)	55 ± 1	
Test scratch length (mm)	10	
Sample material	Rock (freshly broken surface)	
	CERCHAR	WEST
Test duration (s)	1	10
Test result	CERCHAR abrasivity index (CAI)	

At least five test repetitions must be carried out on the rock surface, each time with a new or resharpened pin [17].

Stylus Wear Measurement

The measurement of the length or diameter of the pin wear (d) is carried out with optical and digital methods (microscope). The measurement of the pin can be performed in the side or top view. However, it is recommended to measure in the side view [19]. Figure 7 shows the possible measurements of pin wear. When measuring in the top view, the mean value between d_1 and d_2 is taken for d.

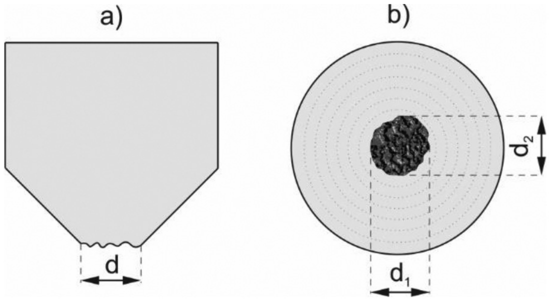

Figure 7: *Measurements of pin wear. (a) Side view (d is the distance between the edges of the worn surface). (b) Top view (d_1 and d_2 are diameters of the worn pin, measured from two orthogonal directions) (adapted from [17]).*

Calculation of CERCHAR Abrasivity Index

For each measurement of pin wear (d), the CERCHAR abrasivity index (CAI) is calculated as

$$CAI = d \times 10 \tag{1}$$

where d is the length of the wear pin surface measured with an accuracy of 0.01 mm [17]. The dimensionless CAI value is given as the arithmetic mean of five or more test repetitions together with the standard deviation [17].

Classification System

The system for classifying abrasivity after ISRM [17] is given in Table 2. This system differs slightly from that proposed by the CERCHAR centre.

Table 2: *Classification of the CERCHAR abrasivity index (CAI) [17].*

Mean value of CAI	Classification/abrasivity description
0.1–0.4	Extremely low
0.5–0.9	Very low
1.0–1.9	Low
2.0–2.9	Medium
3.0–3.9	High
4.0–4.9	Very high
≥5	Extremely high

LCPC Abrasivity Test

The LCPC abrasivity test was developed in the 1980s by a French laboratory (Laboratoire Central des Ponts et Chaussées) to test soil abrasivity. The method is described in French Standard P18-579 [21].

Test Device

The main components of the test device for determining abrasivity are the frame, the motor, the funnel tube, the metal impeller and the sample container. The device is shown schematically in Figure 8. The 750 W motor ensures the rotation of the axle. A metal impeller is attached to the end of the axle and is immersed in a sample container, which is cylindrical in shape with a diameter of 93 mm and a height of 100 mm. The metal impeller (test specimen) has a rectangular shape with dimensions 50 mm x 25 mm x 5 mm. The impeller is made of standardised steel with a Rockwell hardness of HRB 60–75. The steel impeller must be replaced after each test [21].

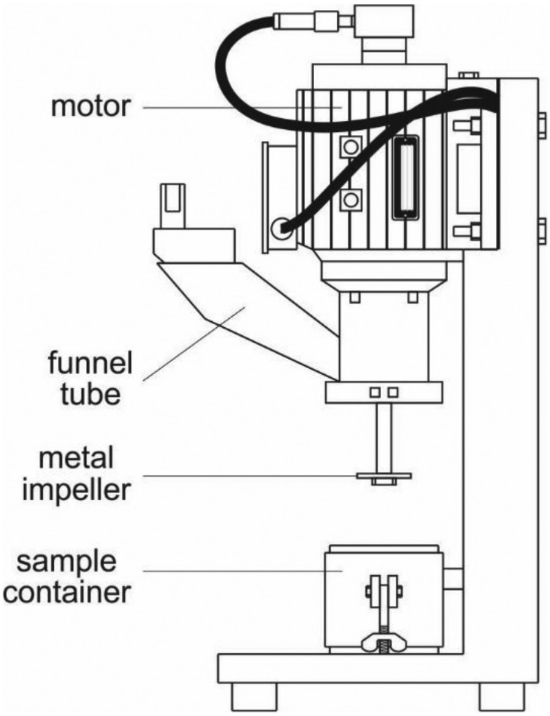

Figure 8: *LCPC abrasivity testing device with main components (adapted from [18]).*

Test Sample

The LCPC testing device is designed to investigate the abrasivity of granular materials with a grain size of 4–6.3 mm. According to French Standard P18-579 a sample of 500 g ± 2 g of a dry material with a grain size of 4–6.3 mm is required. The required grain size of the sample is achieved by sieving. Fractions below 4 mm and above 6.3 mm must not be used in the test [21].

Test Procedure

The sample container is filled with the required granular material through the funnel tube of the testing device. The rectangular metal impeller rotates for 5 min in a sample container at 4,500 rpm. To determine the abrasivity of the sample material, it is necessary to determine the mass of the metal impeller before and after the test. The mass loss of a metal impeller is a measure of the abrasivity of the sample. With the loss of mass, the metal plate also deforms. The more abrasive the material sample is the greater the deformation and mass loss of the impeller [21]. Figure 9 shows schematically the metal impeller before and after the LCPC test. The main parameters of the LCPC abrasivity test are summarised in Table 3.

Table 3: *Main parameters of the LCPC abrasivity test.*

Parameters	Value
Rotational speed (min^{-1})	4,500
Sample material	Soil/granular material
Grain size of the sample (mm)	4–6.3
Sample mass (g)	500 ± 2
Test duration (min)	5
Test result	LCPC abrasivity coefficient (LAC)
	LCPC breakability coefficient (LBC)

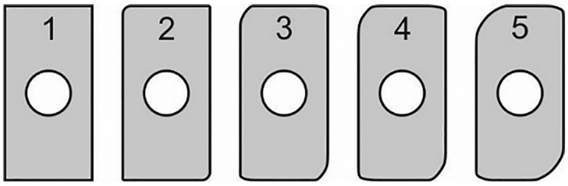

Figure 9: *Schematic representation of metal impeller before and after the LCPC test: 1 new impeller, 2 not abrasive, 3 abrasive/very abrasive, 4 very abrasive and 5 extremely abrasive (adapted from [21]).*

Calculation of LCPC Abrasivity Coefficient

The LCPC abrasivity coefficient (LAC) is calculated as the coefficient of mass loss of the metal impeller and the sample mass [21] as

$$LAC = \frac{m_0 - m}{M} \tag{2}$$

where LAC is the LCPC abrasivity coefficient (g/t), m_0 is the mass of the steel impeller before the LCPC test (g), m is the mass of the steel impeller after the LCPC test (g) and M is the mass of the sample material (=0.0005 t).

The LAC for natural rocks and soils varies between 0 and 2,000 g/t. The value range can be divided into five classes. As there is a close linear correlation (Figure 10) between the LAC and the CAI index, the CAI abrasivity classification can be used [21].

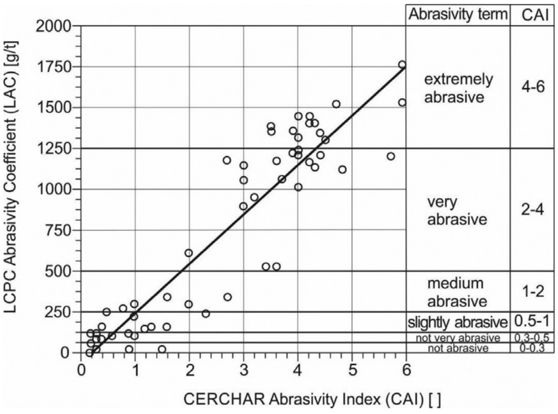

Figure 10: *Correlation between LAC and CAI [21].*

Classification System

The abrasivity classification system in relation to the CAI is given in Table 4 [21].

Table 4: *Classification of LCPC abrasivity coefficient (LAC) in relation to the CERCHAR abrasivity index (CAI) [21].*

LAC (g/t)	CAI (0.1 mm)	Abrasivity term
0–50	0–0.3	Not abrasive
50–100	0.3–0.5	Not very abrasive
100–250	0.5–1.0	Slightly abrasive
250–500	1.0–2.0	(Medium) abrasive
500–1,250	2.0–4.0	Very abrasive
1,250–2,000	4.0–6.0	Extremely abrasive

NTNU/SINTEF Abrasivity Tests

NTNU/SINTEF abrasivity tests have been developed at the Norwegian University of Science and Technology in Trondheim (NTNU-Norges teknish-naturvitenskapelige universitet) in cooperation with the research organisation SINTEF (Stiftelsen for industriell og teknisk forskning).

The AV abrasivity test was developed in the 1960s to evaluate the wear of drill bits. It provides a measure of rock abrasion or the ability to induce wear on a tungsten carbide specimen [22].

The AVS abrasivity test was developed between 1980 and 1983 based on the AV test. The purpose of the test is to evaluate the tool life of mechanised rock TBM tunnelling. Compared to the AV test, the AVS test differs in the specimen material and the duration of the test. The AVS is a measure of rock abrasion or the ability to induce wear on cutter ring steel [22].

Soil abrasion test (SAT^{TM}) was introduced in 2005 to evaluate the tool life of mechanised TBM tunnelling in soft ground and in soil. The test is a further development of the NTNU/SINTEF abrasion tests for rock. The test device for the soil abrasion test is identical to the device for AV and AVS abrasivity tests. The difference is in the sample material [23].

The abrasivity tests are quite similar, except that the AV test measures the wear of a tungsten carbide specimen and the AVS and SAT^{TM} tests measure the wear of a specimen made of TBM cutter ring steel [22, 23].

Device

The device is identical for all three abrasivity tests. In the individual tests, the grain size of the rock or soil sample and the material of the test specimen are different.

The device, which is shown schematically in Figure 11, consists of a drive, a rotating steel disc, a test specimen, a weight, a sample material feeder and a suction device.

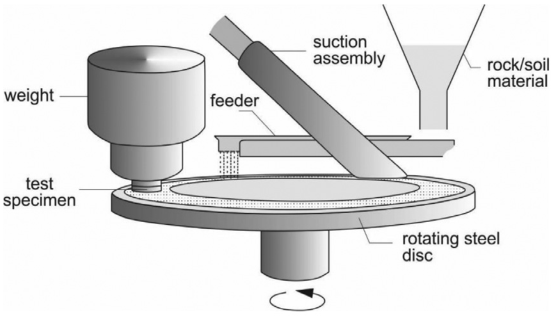

Figure 11: *NTNU/SINTEF abrasivity device (adapted from [22]).*

Test Specimen

The material of the specimen in the AV test is tungsten carbide. The specimen in the AVS and SAT™ tests is steel taken from the TBM cutter ring. The test specimen is cuboidal with a rounded surface in shape. The length of the test specimen for the AV and AVS tests is 30 mm, the width is 10 mm and the radius is 15 mm. The test specimen for the AV and AVS tests is shown in Figure 12.

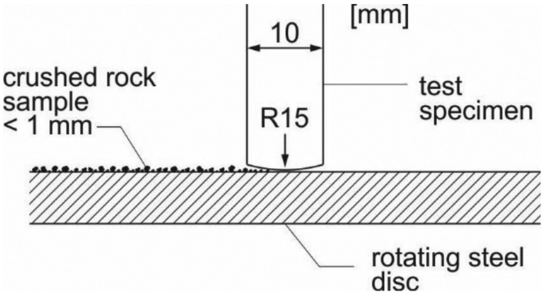

Figure 12: *Test specimen for rock abrasivity test AV and AVS (adapted from [23]).*

The length of the test specimen for the SAT™ test is 30 mm, the width 20 mm and the radius 15 mm. The test specimen for the SAT™ test is shown in Figure 13. During the rotation of the steel plate the rock or soil sample passes under the rounded part of the stationary test specimen.

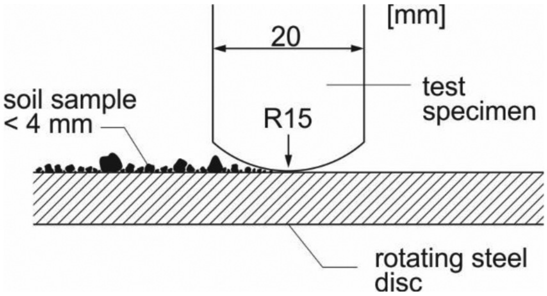

Figure 13: *Test specimen for soil abrasivity test SAT™ (adapted from [23]).*

Sample Material

Crushed rock powder with a grain size of less than 1 mm is used for the AV and the AVS tests. Therefore the sample material has to be crushed and/or ground and sieved before the test.

For the SAT™ test, a dry and gently crushed soil sample with a grain size of less than 4 mm is used. The SAT™ test is applicable for the investigation of clay, silt and sand fractions [23].

Test Procedure

Abrasivity tests AV, AVS and SAT™ represent the time-dependent abrasion of tungsten carbide (AV) or TBM cutter ring steel (AV, SAT™), caused by rock powder or soil grains. The same test device is used for all the three tests.

A circular steel disc with a circumference of 1,000 mm (318.3 mm diameter) is set horizontally and rotates around its axis at a speed of 20 rpm. A rock or soil sample falls via the feeder onto the upper outer part of the steel disc and forms a material belt. The mass flow rate of the sample material is approximately 80 g/min. In front of the feeder (in the direction of rotation) a test specimen is mounted and loaded with a normal force of 100 N. The test specimen is firmly clamped and is stationary during the test. The contact between the test specimen and the sample material causes abrasive wear of the test specimen. A suction device is installed behind the feeder (in the direction of rotation) to remove the sample material from the steel disc. This allows the test specimen to remain in contact with new material during the entire test. The length of the path that the test specimen travels on the sample material is 100 m for the AV test and 20 m for the AVS and SAT™ test [22, 23].

The duration of the AV test is 5 min or 100 disc rotations, that is, 100 m.

The duration of the AVS and SAT™ test is 1 min or 20 disc rotations, that is, 20 m.

The tests AV, AVS and SAT™ are normally carried out on 2–4 test specimens. The deviation is very small and should not exceed 5 mg of weight loss if the test is performed correctly. The reported AV, AVS and SAT™ values are the main values of 2–4 parallel tests [22]. The main parameters of the NTNU/SINTEF abrasivity tests are listed in Table 5.

Table 5: *Main parameters of the NTNU/SINTEF abrasivity tests.*

Parameters	Value		
Load (N)	100		
Rotational speed (min^{-1})	20		
Material mass flow (g/min)	80		
	AV	AVS	SAT™
Test duration (min)	5	1	1
Sample material	Crushed rock powder	Crushed rock powder	soil
Grain size of the sample (mm)	<1	<1	<4
Test specimen material	Tungsten carbide	Cutter ring steel	Cutter ring steel
Test result	AV value	AVS value	SAT™ value

AV, AVS and SAT™ values

To determine the abrasivity, it is necessary to measure the mass of the test specimen before and after the test. The loss of mass of the test specimen is a measure of the abrasivity of the rock or soil sample.

Classification System

The classification given in Table 6 is based on the distribution of the recorded results of the 2,621 samples used to determine AV, 1,590 samples tested to determine AVS and 254 abrasivity measurements on soil samples for the determination of SAT™. The reason for proposing only three classification categories for SAT™ is the relatively small amount of data compared to AV and AVS measurements [23].

Table 6: *Classification of rock and soil abrasion on tungsten carbide (AV) and cutter steel (AVS, SAT™) test specimen [22].*

Abrasion	AV (mg)	AVS (mg)	SAT™ (mg)
Extremely high	≥58.0	≥44.0	
Very high	42.0–57.9	36.0–44.0	
High	28.0–41.9	26.0–35.9	≥22.0
Medium	11.0–27.9	13.0–25.9	7.0–22.0
Low	4.0–10.9	4.0–12.9	≤7.0
Very low	1.1–3.9	1.1–3.9	
Extremely low	≤1.0	≤1.0	

RIAT Abrasivity Test

The RIAT was developed at the Norwegian University of Science and Technology in Trondheim (NTNU-Norges teknish-naturvitenskapelige universitet). The aim of the test is to imitate the wear behaviour of TBM cutter discs in mechanised tunnelling.

The rock and soil abrasivity tests described previously (CERCHAR, LCPC, NTNU) use sliding and impact contacts to induce wear. In contrast to the tests described above, the RIAT is based on a rolling contact that is more realistic for assessing disc cutter wear. Another difference between some abrasivity tests and the RIAT is that these tests use crushed rock samples instead of intact samples [24].

Device

The RIAT device, schematically shown in Figure 14, consists of two interchangeable miniature rolling discs that roll over and penetrate the surface of an intact rock sample. Rotation, torque and vertical thrust are provided by a drive unit [24].

The rolling diameter or the distance between two miniature discs is 60 mm. The diameter of the miniature rolling disc is 30 mm and the tip width is 4 mm [24].

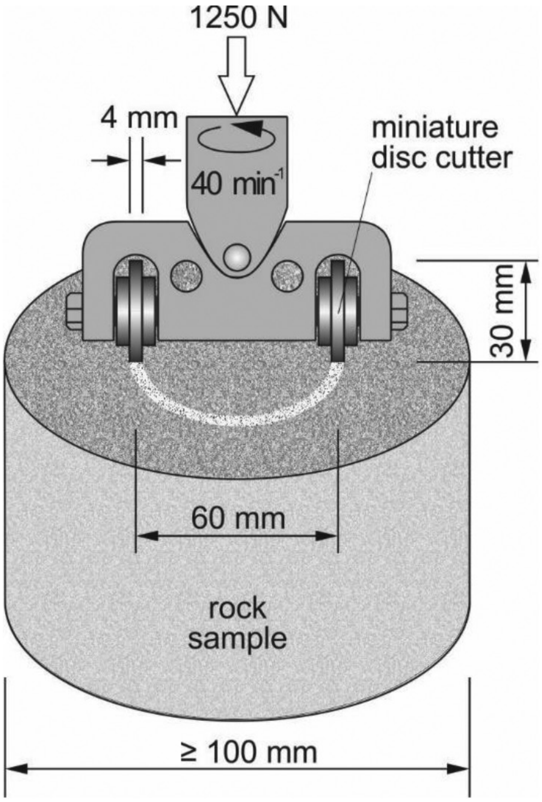

Figure 14: *RIAT device (adapted from [24]).*

Test Sample

The test sample is intact rock that can have any shape. It is recommended that the surface of the rock sample is smooth and horizontal. Usually a circular rock core is used for the test. In such a case the minimum diameter of the rock sample is 100 mm [24].

Miniature Rolling Discs

Miniature rolling discs are made of hot work tool steel AISI type H13, which is normally used for the actual TBM cutter rings. The miniature discs have a constant tip width of 4 mm. The diameter of the discs is 30 mm. The Rockwell hardness of the steel is HRC 50 ± 1 [24].

Test Procedure

The test is carried out in such a way that two miniature discs roll over a rock sample under the influence of the normal thrust of 1,250 N at a speed of 40 rpm and a center distance of 60 mm. The test parameters were determined in relation to real cutter parameters in mechanised TBM tunnelling in hard rock. The test duration is 30 min. Rock dust and debris formed during the test should be removed from the surface of the rock to be tested to ensure that the miniature rolling disc is in constant contact with the rock sample. A combination of compressed air and suction is used for this purpose [24]. The main parameters of the RIAT are listed in Table 7.

Table 7: *Main parameters of the RIAT [24].*

Parameters	Value
Thrust (N)	1,250
Rolling velocity (min^{-1})	40
Test duration (min)	30
Disc hardness (HRC)	50 ± 1
Sample material	Rock (smooth surface)
Test result	RIAT abrasivity index (RIAT$_a$)
	RIAT indentation index (RIAT$_i$)

Determination of the RIAT Abrasivity Index and the RIAT Indentation Index

The result of RIAT is the RIAT abrasivity index (RIAT$_a$) and the RIAT indentation index (RIAT$_i$). RIAT$_a$ is defined as the mass loss of the miniature rolling disc, measured in milligrams after the test. A representative mean value is determined by at least three tests [24].

RIAT$_i$ is defined as the mean value of 10 evenly distributed measurements of the penetration depth of the miniature rolling disc into the rock surface in 1/100 mm. The RIAT$_i$ value is an indication of the penetration resistance of the rock or the hardness of the rock surface [24].

In the study reported by Macias et al. [24], eight types of rocks were selected for the RIAT. At least three parallel tests were carried out for each rock type, so that a total of 29 were performed. The lowest and highest RIAT$_a$ of the test performed is 3 for limestone and 104 for quartzite. The lowest and highest RIAT$_i$ of the test carried out is 5 for quartzite and 380 for limestone.

As the study shows, RIAT$_a$ and RIAT$_i$ are inversely correlated. A higher RIAT$_a$ means a lower RIAT$_i$ [24].

Due to a small number of tests carried out, the classification for the RIAT has not yet been determined.

Gouging Abrasion Test

The gouging abrasion test was developed to assess rock abrasivity in environments where high stress loads are expected at high speeds and at different angles of incidence. These conditions can be achieved in many mineral processing and mining equipment. Abrasion under such conditions causes considerable wear of the tool material [2].

Apparatus

A gouging abrasion test simulates very high stress abrasion under high-energy impact conditions [2].

The rock sample with a rectangular shape and flat surface is clamped in the sample holder. A steel pin with a 90° angle is attached to the end of the pendulum arm. The length of the pendulum arm is such that the steel pin forcibly touches the surface of the rock sample as it swings past, creating a scratch along the entire length of the rock sample [2].

The apparatus is shown schematically in Figure 15. The rock sample is held securely in the sample holder, which can be moved vertically and horizontally by means of the transfer screw or spring mechanism. The wear tool is rigidly positioned in the tool holder of the pendulum arm, which is released from its working position. The steel pin scratches over the rock surface as it moves. The pendulum has 300 J available impact energy. The impact speed is 5.2 m/s [2].

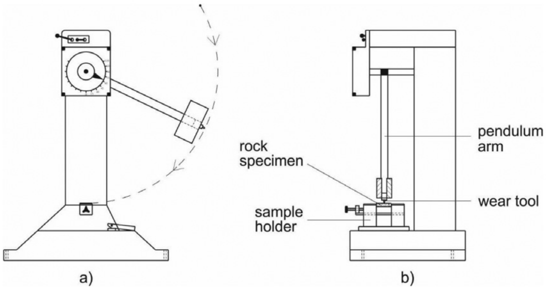

Figure 15: *Gouging abrasion test apparatus. (a) Front view. (b) Side view (adapted from [2]).*

Test Sample

The rock sample has a rectangular shape with a length of 80 ± 0.5 mm. Due to irregularities in the samples, the width can vary and take on values between 25 and 50 mm. The thickness of the sample is between 10 and 16 mm. The examined surface of the rock sample is flat and smooth, as is the case with a diamond saw cut. This eliminates the influence of the different surface roughness of the rock sample on the test results [2].

Wear Tool

According to Golovanevskiy and Bearman [2], a wear tool of Rockwell hardness HRC 40–42 is recommended for the gouging abrasion test. The wear tool is made of steel AS 1444/4340-Y. The tool is 25 mm long with a diameter of 9.375 ± 0.25 mm. The tool pin has a 90° angle.

Test Procedure

The prepared rock sample is placed in the sample holder. It is necessary to ensure the horizontal surface of the sample to be examined. The apparatus is equipped with a screw device for fine adjustment of the sample height and a spring system for rapid horizontal movement [2].

The wear tool is carefully inserted into the wear tool holder of the pendulum arm. When the pendulum arm is fully vertical, the pin of the wear tool is directed vertically into the test surface of the rock sample in the holder. At this point, there are a few millimetres of clearance

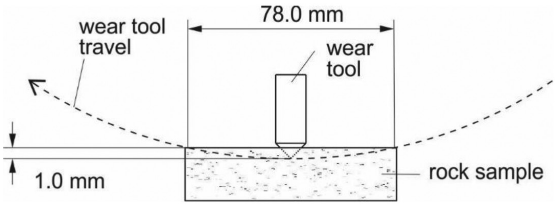

Figure 16: *Wear contact between tool and rock sample (adapted from [2]).*

between the pin of the wear tool and the surface of the rock sample [2].

The sample holder is then lifted together with the sample via a screw assembly to achieve a slight contact between the surface of the rock sample and the wear tool pin [2].

The pendulum arm is lifted to its initial position. The sample holder with the rock sample is then raised by 1.0 mm. The accuracy is measured with a micrometre. This allows a 1.0-mm deep wear tool cut in the rock sample. The wear tool is allowed to make a 78-mm long arc-shaped cut on the surface of the rock sample, as shown in Figure 16 [2].

The pendulum arm is released. The pin of a wear tool produces a cut or scratch when it moves over a rock surface. The pendulum arm continues to move to the highest point of the path even as it passes the rock sample. When the pin of the wear tool is no longer in contact with the rock surface after the first swing, the sample holder moves quickly in a horizontal direction perpendicular to the plane of the pendulum motion via the spring mechanism. Due to this displacement of the rock sample, the wear tool and the rock surface no longer come into contact when the arm is moved back. The sample after several tests is schematically shown in Figure 17. When the pendulum stops, the wear tool is removed from the holder and the pin wear is measured. The rock sample holder is returned to its original working position and is moved about 5 mm to provide a fresh surface in the rock sample for further testing. The described procedure is valid for a single test run. For each further test run, a wear tool with an unused pin is inserted into the wear tool holder of the pendulum arm and the procedure described above is repeated [2]. The main parameters of the gouging abrasion test are listed in Table 8.

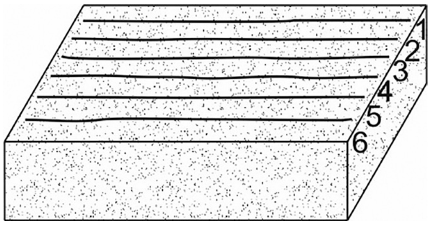

Figure 17: *Rock sample after testing (schematic). Numbers 1–6 represent individual scratches from the test (adapted from [2]).*

Table 8: *Main parameters of the gouging abrasion test.*

Parameters	Value
Impact energy (J)	300
Wear tool hardness (HRC)	40–42
Test scratch length (mm)	78
Sample material	Rock (smooth surface)
Test result	Gouging abrasion index (Gi)

Gouging Abrasion Index

The gouging abrasion index (Gi) is determined in the same way as the CAI, that is, the average distance of pin wear in millimetres multiplied by a factor of 10 [2].

For the representative value of the Gi, several tests should be carried out on a single rock sample. In practice, it is advisable to perform at least three test runs on a single rock sample, using a new wear tool and a fresh wear surface of the rock sample. This can be done with three wear tools and a 25–30-mm wide rock sample [2].

Conclusion

The wear of tools and equipment during technological processes in geotechnology and mining is associated with high economic costs. On the one hand, there are the material costs associated with the replacement of worn tools or equipment, and on the other hand, there are the costs of downtime of the work process. The abrasivity is directly related to tool wear. Knowledge of the tribological system and wear mechanisms helps us to understand this complex problem. However, once the basics are known and the problem is understood, the next step can be taken, that is, the attempt to prevent it at least partially and the possibility to model or predict tool wear. It is not possible to prevent the abrasive wear of geotechnology and mining application tools in such an aggressive environment as the geological one. However, with the knowledge of the problem it is possible to develop materials that build tools. Every small step to improve the wear resistance of a material is very valuable. The four main components of the tribological system are the geological material, surrounding medium, tools and load type. It should be considered that the first two components mentioned above cannot be modified. However, the tool (and the material it is made of) and the load type can be modified. Any change to the component of the tribological system is reflected in the wear. Therefore, a detailed study of the wear mechanisms for a specific technological process (be it mechanised tunnelling, drilling, crushing or grinding of mineral raw materials) should be carried out, and on this basis an optimisation of the geometry and material of the tool in dynamic contact with the geological material and the type of loading should be carried out.

Two factors are of particular importance for a comprehensive understanding of tool wear. These are the wear rate and the mode of wear. In a comprehensive approach, the wear rate can be defined as the first stage and the wear mode as the second stage of wear investigation. Laboratory test methods for assessing the abrasivity of rocks and soils are important because they allow the wear rate of tools that interact dynamically with the abrasive geological material to be determined. The wear rate can be determined immediately after the test is performed, for example, by weighing the loss of mass of the test specimen or by microscopic examination of the pin wear, depending on the test set-up. However, the second stage of the comprehensive approach is to determine the mode of wear, which can be derived from the first stage.

This article presents a review of the laboratory tests to assess the abrasivity of rocks and soils, which are useful in the field of geotechnology and mining. These abrasivity tests can help us to gain a comprehensive understanding of tool wear, especially in the first stage, for determination of the wear rate. However, it is recommended that starting from the first stage, the study of wear be continued in the second stage, which is concerned with determining the mode of wear. Compared to the first stage, the second stage is more demanding and time-consuming, as it requires interdisciplinary material knowledge and several individual geochemical and metallurgical investigations at the microscopic level. A comprehensive approach to the investigation of wear is the basis for the development of wear resistant tools and models for the prediction of tool life in individual areas of geotechnology and mining.

References

[1] Petrica, M., Painsi, M., Badisch, E., Peinsitt, T. (2014): Wear Mechanisms on Martensitic Steels Generated by Different Rock Types in Two-Body Conditions. *Tribology Letters*, 53(3), pp. 607–616, DOI: 10.1007/s11249-014-0298-z.

[2] Golovanevskiy, V.A., Bearman, R.A. (2008): Gouging abrasion test for rock abrasiveness testing. *International Journal of Mineral Processing*, 85(4), pp. 111–120, DOI: 10.1016/j.minpro.2007.08.004.

[3] BBT Brenner Base Tunnel [online]. Galleria di Base del Brennero – Brenner Basistunnel BBT SE [cited 3/5/2020]. Available on: *https://www.bbt-se.com*.

[4] Marti Group [online, cited 3/5/2020]. Available on: *https://www.marti.com*.

[5] Robbins [online]. The Robbins company [cited 3/5/2020]. Available on: *https://www.therobbinscompany.com*.

[6] Krauze, K., Bołoz, Ł., Wydro, T. (2015): Parametric Factors for the Tangential-Rotary Picks Quality Assessment. *Archives of Mining* Sciences, 60(1), pp. 265–281, DOI: 10.1515/amsc-2015-0018.

[7] Boart Longyear [online]. Boart Longyear company [cited 3/5/2020]. Available on: *https://www.boartlongyear.com*.

[8] Varel [online]. Varel International Energy Services [cited 3/5/2020]. Available on: *http://www.vareloilandgas.com*.

[9] Tkalich, D., Yastrebov, V.A., Cailletaud, G., Kane, A. (2017): Multiscale modeling of cemented tungsten carbide in hard rock drilling. *International Journal of Solids and* Structures, 128, pp. 282–295, DOI: 10.1016/j.ijsolstr.2017.08.034.

[10] Yahiaoui, M., Paris, J.Y., Denape, J., Dourfaye, A. (2015): Multiscale and Comparative Study of WC-Co Tribological Behavior. In: *Procédés et Génie civil: 27ème Journées Internationales Francophones de Tribologie: JIFT*, Nantes, France, Do, M.T., Cérézo, V., Kapsa, P. (eds.). Presses des Mines: Paris, pp. 219–226.

[11] Cavpower [online, cited 3/5/2020]. Available on: *https://www.cavpower.com*.

[12] RWE [online]. RWE Group [cited 3/5/2020]. Available on: *https://www.group.rwe*.

[13] Blumaq [online, cited 3/5/2020]. Available on: *https://www.blumaq.com*.

[14] Sandvik [online, cited 3/5/2020]. Available on: *https://www.rocktechnology.sandvik*.

[15] Metso [online, cited 3/5/2020]. Available on: *https://www.metso.com*.

[16] Energosteel [online, cited 3/5/2020]. Available on: *https://energosteel.com*.

[17] Alber, M., Yarah, O., Dahl, F., Bruland, A., Käsling, H., Michalakopoulos, T.N., Cardu, M., Hagan, P., Aydin, H., Özarslan, A. (2013): ISRM Suggested Method for Determining the Abrasivity of Rock by the CERCHAR Abrasivity Test. *Rock Mechanics and Rock Engineering*, 47(1), pp. 261–266, DOI: 10.1007/s00603-013-0518-0.

[18] Käsling, H., Thuro, K. (2010): Determining rock abrasivity in the laboratory. In: *Rock mechanics in civil and environmental engineering: proceedings of the European Rock Mechanics Symposium (EUROCK) 2010*, Lausanne, Switzerland, Zhao, J. (ed.). CRC Press: Leiden.

[19] Plinninger, R., Käsling, H., Thuro, K., Spaun, G. (2003): Testing conditions and geomechanical properties influencing the CERCHAR abrasiveness index (CAI) value. *International Journal of Rock Mechanics & Mining Sciences*, 40(2), pp. 259–263, DOI: 10.1016/S1365-1609(02)00140-5.

[20] Aydin, H. (2019): Investigating the effects of various testing parameters on Cerchar abrasivity index and its repeatability. *Wear*, 418–419, pp. 61–74, DOI: 10.1016/j.wear.2018.11.001.

[21] Thuro, K., Singer, J., Käsling, H., Bauer, M. (2006): Soil Abrasivity Assessment Using the LCPC Testing Device. *Felsbau*, 24(6), pp. 37–45, DOI: 10.1201/NOE0415444019-c103.

[22] Dahl, F., Bruland, A., Jakobsen, P.D., Nilsen, B., Grøv, E. (2012): Classification of properties influencing the drillability of rocks, based on the NTNU/SINTEF test method. *Tunnelling and Underground Space Technology*, 28, pp. 150–158, DOI: 10.1016/j.tust.2011.10.006.

[23] Jakobsen, P.D., Bruland, A., Dahl, F. (2013): Review and assessment of the NTNU/SINTEF Soil Abrasion Test (SAT™) for determination of abrasiveness of soil and soft ground. *Tunnelling and Underground Space Technology*, 37, pp. 107–114, DOI: 10.1016/j.tust.2013.04.003.

[24] Macias, F.J., Dahl, F., Bruland, A. (2016): New Rock Abrasivity Test Method for Tool Life Assessments on Hard Rock Tunnel Boring: The Rolling Indentation Abrasion Test (RIAT). *Rock Mechanics and Rock Engineering*, 49(5), pp. 1679–1693, DOI: 10.1007/s00603-015-0854-3.

Original scientific paper

Received: Jun 04, 2020
Accepted: Jun 16, 2020
DOI: 10.2478/rmzmag-2020-0009

Retrogression of Orthopyroxene-bearing Gneiss of Iboropa Akoko, Southwestern Nigeria

Retrogresija gnajsa z ortopiroksenom iz območja Iboropa Akoko, jugozahodna Nigerija

E.J. Oziegbe[1,*], V.O. Olarewaju[2], O.O. Ocan[3], G.Costin[4]
[1] Department of Geosciences, Faculty of Science, University of Lagos, Nigeria
[2] Department of Geology, Obafemi Awolowo University, Nigeria
[3] Department of Geological Science, College of Science, Engineering and Technology, Osun State University, Nigeria
[4] Earth, Environmental and Planetary Sciences, Rice University, Texas, USA
* eoziegbe@unilag.edu.ng

Abstract

In this article, we report the mineral chemistry and petrographic features of charnockitic exposure of Iboropa within Precambrian Basement Complex of Nigeria. The mineral assemblages are pyroxene, plagioclase, biotite, hornblende, alkali feldspars, microperthite, quartz and ilmenite, with apatite occurring as accessory mineral. Apatite occurs in abundance as euhedral crystals. Orthopyroxene observed is strongly pleochroic and has numerous microfractures, and it is hypersthene ($En_{45}Fs_{54}Wo_1$) with low TiO_2 and MnO, having extremely low percentage of CaO. Hypersthene is mantled by a complex corona of amphibole, and the amphibole is hornblende with a chemical formula: $(K,Na)(Ca,Fe)_2(Fe,Mg,Al,Ti)_5(Al,Si)_8O_{22}(OH)_2$. Plagioclase occurs as inclusions in both pyroxene and biotite. Biotite has high concentration of TiO_2 and extremely low CaO. The opaque mineral observed is ilmenite and it is concentrated around hypersthene and amphibole. Rare earth element (REE) displays negative Eu anomaly with enrichment of light REE over heavy REE. Amphiboles surrounding orthopyroxene are evidences of retrograde reactions and are formed at the expense of orthopyroxene reacting with plagioclase and quartz in the presence of fluid. The relationship between the mineral assemblages suggests the retrogression of the gneiss that might be as a result of rehydration process, and it is a transition from granulite facies to amphibolite facies during a retrogressive form of metamorphism.

Keywords: Hypersthene, microfractures, retrograde, microperthite, rehydration.

Povzetek

V tem članku predstavljamo mineraloško-kemične in petrografske značilnosti charnokita, ki se pojavlja na območju Iboropa znotraj predkambrijske podlage Nigerije. Opazovani minerali so: piroksen, plagioklaz, biotit, rogovača, alkalijski glinenec, mikropertit, kremen in ilmenit, z apatitom ki se pojavlja kot akcesorni mineral. Apatit je akcesorni mineral in se pojavlja v obilju kot evhedralni kristal. Opazovan ortopiroksen je močno pleokroičen in ima številne mikrorazpoke. Je hipersten ($En_{45}Fs_{54}Wo_1$) z nizkim TiO_2 in MnO in ima ekstremno nizek delež CaO. Hipersten je oplaščen s kompleksno korono amfibola, ki je rogovača s kemijsko formulo $(K,Na)(Ca,Fe)_2(Fe,Mg,Al,Ti)_5(Al,Si)_8O_{22}(OH)_2$. Plagioklaz se pojavlja kot inkluzije v piroksenu in biotitu. Biotit ima visoko koncentracijo TiO_2 in ekstremno nizko CaO. Opazovan nepreseven mineral je ilmenit in je koncentriran okoli hiperstena in amfibola. REE kaže na negativno Eu anomalijo z obogatitvijo LREE nad HREE. Amfiboli, ki obkrožajo ortopiroksene, so dokaz retrogradne reakcije in nastanejo pri reakciji ortopiroksena s plagioklazom in kremenom v prisotnosti fluida. Razmerje med mineralno sestavo predlaga retrogresijo gnajsa, ki bi lahko bila rezultat rehidracijskega procesa in je prehod granulitnega faciesa v amfibolitni facies med retrogresivno obliko metamorfizma.

Ključne besede: hipersten, mikro razpoke, retrogradno, mokropertit, rehidracija.

Introduction

Orthopyroxene-bearing gneiss is usually referred to as charnockitic gneiss or granulite, most especially if the orthopyroxene is hypersthene. In this article, the use of the term charnockitic gneiss will be adhered to. Charnockite are hypersthene-bearing rocks [1]. There has been an extensive study on charnockites and charnockitic rocks in India [2–5]. Charnockites are orthopyroxene-bearing anhydrous granitoids [1, 6], and they are of magmatic or metamorphic origin [7]. Charnockites are restricted to high-grade belt and those that are of metamorphic origin take their source either from igneous or from sedimentary protoliths during high-grade metamorphism under anhydrous conditions [8]. In some parts of south India and Sri Lanka, 'patchy' charnockites have been termed as 'arrested growth', 'in situ' charnockites or charnockitisation of amphibolite facies [9–15]. For the patchy charnockites of east Gondwana, metamorphic transformation from amphibolite facies gneiss occurred by two mechanisms: CO_2 ingress from deep level and a drop in the pressure of fluid [11, 16–18]. The process of charnockitisation is propagated by the influx of the CO_2–H_2O fluid, which results in the migration of most basic elements from the initial rock towards the transition zones [19]. Touret and Huizenga [20] studied charnockite microstructures from magmatic to metamorphic and realised that microstructures alone cannot always provide solution to the igneous or metamorphic origin of charnockites due to high temperature of recrystallisation. In their study, further evidence for the presence of brine fluids includes the high-temperature fluid–mineral reactions at inter-grain boundaries (K-feldspar microveins and myrmekites) observed in both igneous and metamorphic charnockites. Yang et al. [21] gave the first report of Paleoproterozoic incipient charnockite from the North China Cratons. They documented centimetre- to decimetre-scale anhydrous zones of incipient charnockite within tonalite–trondhjemite–granodiorite (TTG) rocks that are adjacent to an intrusive charnockite. From their study, they concluded that the incipient charnockite formed at ultrahigh-temperature conditions of 890°C–970°C.

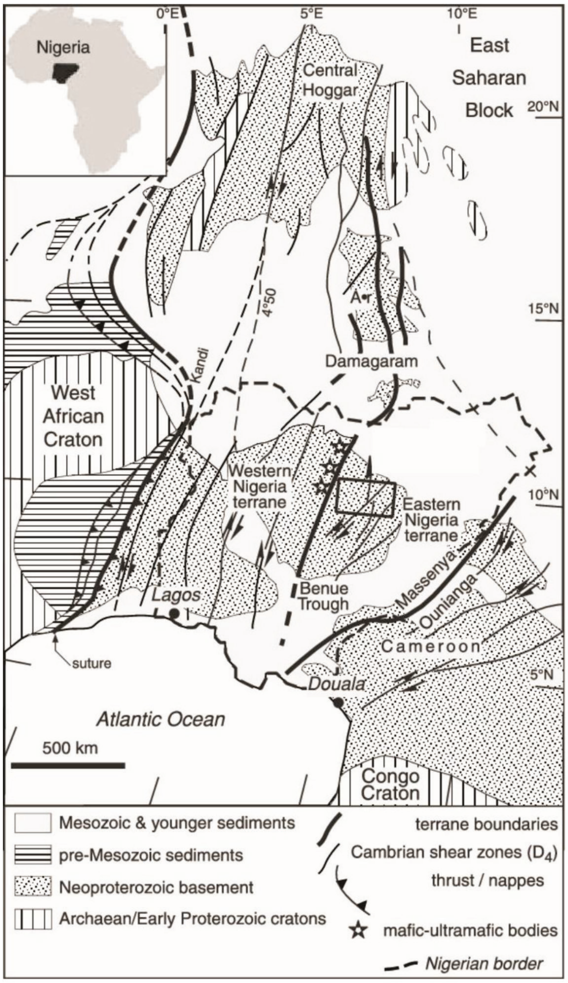

Figure 1. *Sketch geological map of the Hoggar-Aïr-Nigeria Province showing the Neoproterozoic Trans-Saharan belt, resulting from terrane amalgamation between the cratons of West Africa and Congo and the East Saharan block [26].*

The study area for this research is part of the Neoproterozoic basement of Nigeria (Figure 1). Rocks of the Basement Complex of Nigeria are made up of predominantly migmatitic and granitic gneisses; quartzites; slightly migmatised to unmigmatised meta-sedimentary schists and meta-igneous rocks; charnockitic, gabbroic and dioritic rocks and members of the Older Granite suite mainly granites, granodiorites and syenites [22]. The migmatite gneisses of South-Western Nigeria are usually composed of three components, all of which sometimes may be present in a single outcrop [22]. These components are (a) early gneiss, (b) mafic–ultramafic bands and (c) granitic or felsic components. Iboropa Akoko is about 10 km from

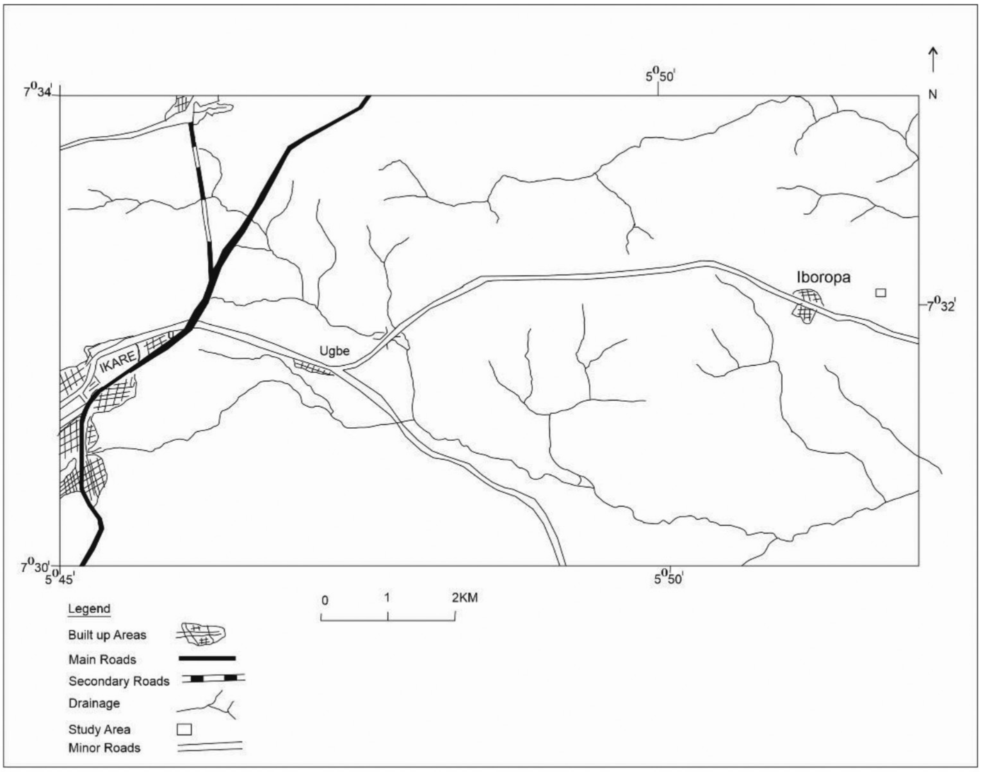

Figure 2. *Location map of the study area.*

Figure 3. *Field photograph of charnockitic gneiss with quartzo-feldspathic material at Iboropa Akoko.*

Ikare (Figure 2), and Ikare area is dominated by migmatite gneiss–quartzite complex, making up 90% of the rock units [23]. The charnockitic gneiss of Iboropa is dark grey in colour (Figure 3), and it is poorly foliated. Other associated rocks in this area are grey gneiss, granitic gneiss, pelitic gneiss and pegmatite. Almost all granulite facies rocks described so far from the Nigerian Basement Complex are of charnockitic affinity. Rocks of the granulite facies are found in all crystalline basement of the world [24]. Hubbard [25] suggested that these granulite facies rocks represent relicts of an earlier and more widespread granulite facies metamorphism of unspecified age, predating the Pan-African Orogeny.

However, Rahaman and Ocan [23] suggested that the charnockitic rocks were original igneous rocks that retained their anhydrous affinity during the Pan-African Orogeny. Most of the other rocks of the basement complex described so far range in metamorphic grades from greenschist to upper amphibolite facies. Metamorphic rocks that have attained higher grades of metamorphism are probably the cordierite–sillimanite gneisses at Bena village in northern Nigeria, which Sacchi [27] ascribed to the granulite facies. On the published 1:250,000 G.S.N. Sheets 61, Akure, some localities within the migmatite gneiss–quarzite complex were indicated by Dempster [28] as containing granulite facies mineral paragenesis. Petrographic evidence presented strongly suggests that the granulite facies mineral paragenesis in Ikare area is a result of prograde metamorphism [29]. In this respect, rocks of the granulite facies mineralogy in Ikare area are different from others of similar mineralogy described so far [23], as original igneous rocks, because of composition, especially low water content, retained their original (igneous) granulite facies mineralogy. Data used for this work are from the PhD thesis of the first author.

Materials and Methods

Detailed petrography was carried out using Petrographic Microscopes, both at the Department of Geology, Obafemi Awolowo University and Department of Geology, Rhodes University, South Africa. Major elements and trace elements were determined at the Central Analytical Facility (CAF), Stellenbosch University, South Africa, using X-ray fluorescence (XRF) and laser ablation ICP-MS, respectively. The mineral chemistry of the minerals was done using electron microprobe analysis (EPMA) at the Department of Geology, Rhodes University South Africa by a JEOL JXA 8230 Superprobe, using 4 WD spectrometers. Equipment operating conditions employed for the EPMA were 15 kV acceleration voltage, 20 nA probe current, beam size of ~1 μm and counting time 10 s on peak and 5 s on each lower and upper background, respectively. Natural standards were used for measuring the characteristic X-rays, and the ZAF matrix correction method was employed for quantification.

Results

Petrography

The charnockitic gneiss is granoblastic in texture. The minerals that are present in the charnockitic gneiss include pyroxenes, amphiboles, biotite, plagioclase feldspar, K-feldspar quartz, opaque minerals, while apatite occur as accessory mineral. Orthopyroxene occur as porphyroblasts, changing from colourless to grey, highly pleochroic and changing from grey to pinkish, a property indicative of hypersthene (Figure 4). Some of the porphyroblasts have inclusions of plagioclase and biotite (Figure 4) which make them poikiloblastic in texture. There is rimming of pyroxene by amphibole (Figure 5a). Back scattered electron (BSE) image and elemental maps in Figure 5a are also presented (Figures 5b and 6). There are small patches of pale-coloured biotite along the cleavage planes of pyroxenes (Figure 4a). Amphibole occurs as large, xenoblastic, dark green crystals and it is strongly pleochroic with inclusions of pyroxene (Figure 7a and 7b). Also, amphiboles have close association with opaque minerals. Biotite observed is of two varieties, namely the light brown and the deep brown, and both are strongly pleochroic. The longer axes of biotite are slightly aligned in preferred orientations

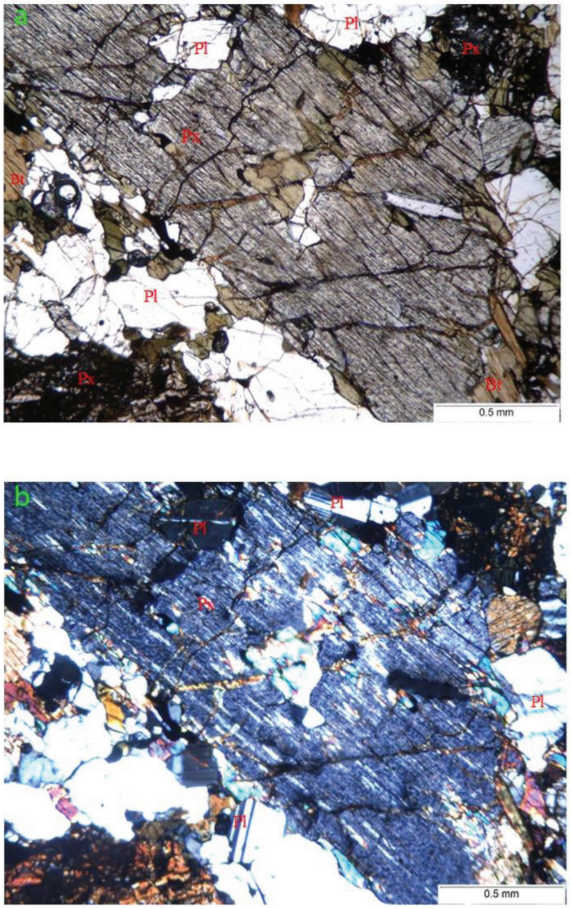

Figure 4. *Photomicrographs showing (a) porphyroblast of pyroxene (Px) having numerous fractures. Pale biotite (Bt) along cleavage planes (PPL). (b) Plagioclase (Pl) occurring as inclusions in pyroxene (XPL). PPL, plane polarised light; XPL, crossed polarised light.*

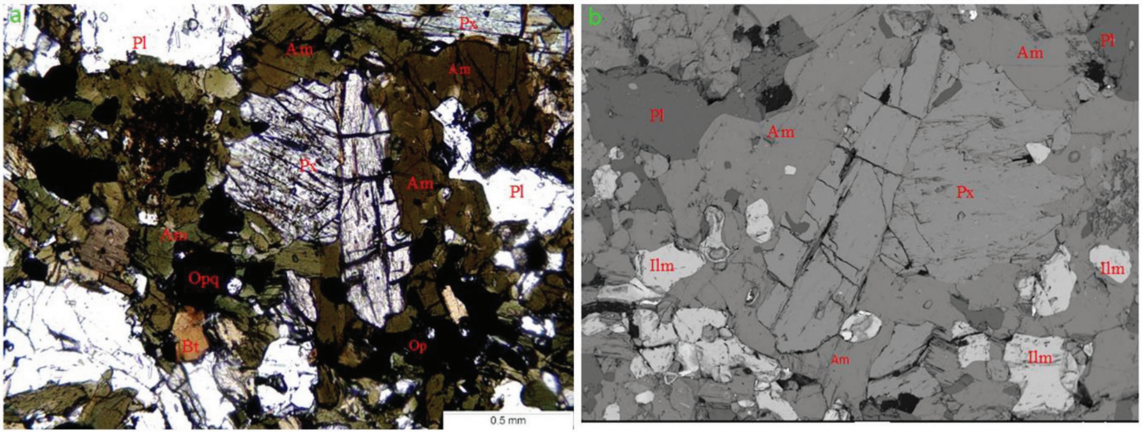

Figure 5. *(a) Photomicrograph showing pyroxene (Px) rimmed by amphibole (Am). The opaque mineral (Opq) (PPL). (b) Back-scattered electron image of minerals shown in (a). PPL, plane polarised light; XPL, crossed polarised light.*

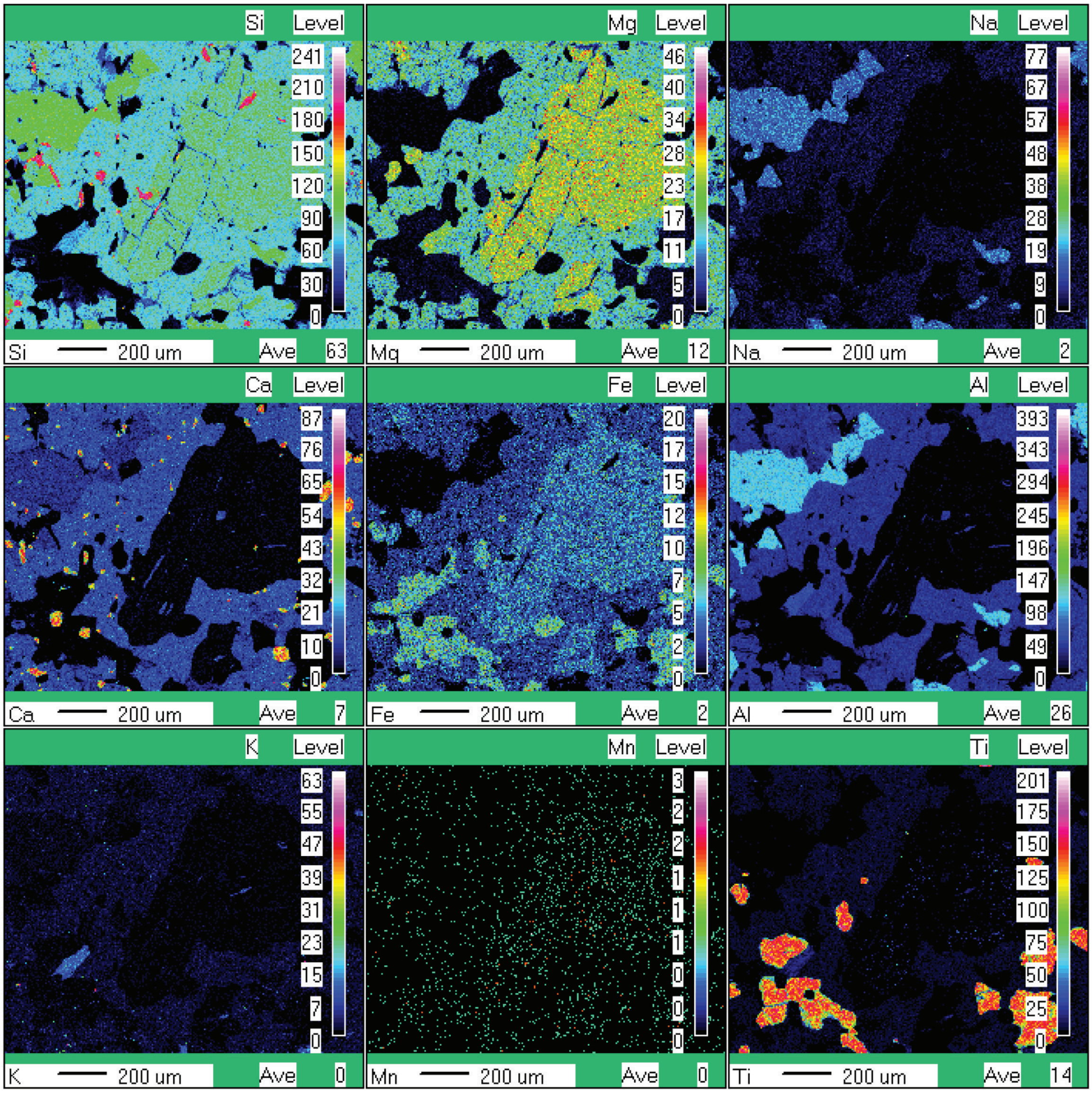

Figure 6. *The compositional maps of minerals shown in Figure 5, showing elemental levels of Si, Mg, Na, Ca, Fe, Al, K, Mn and Ti.*

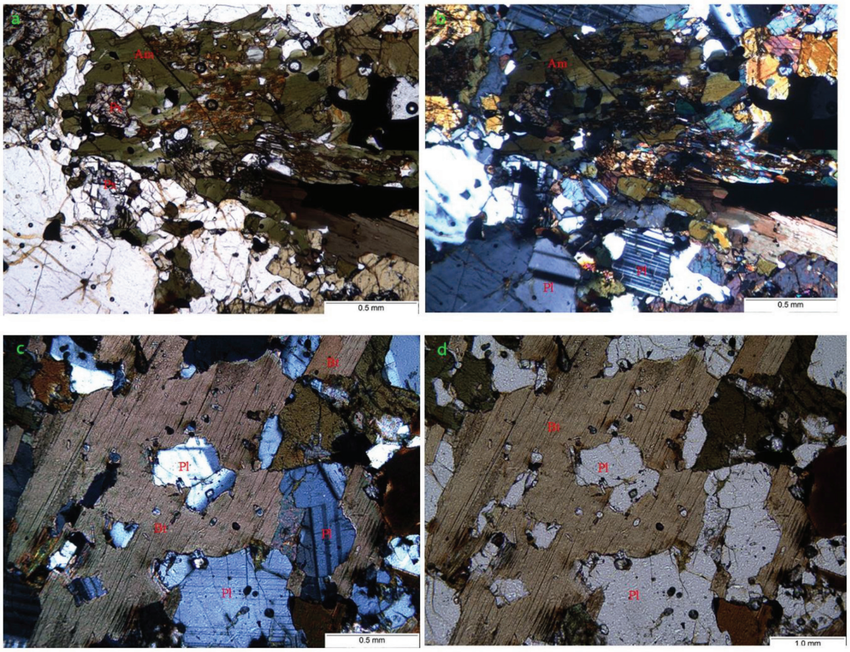

Figure 7. *Photomicrographs showing: (a) amphiboles (Am) with inclusions of pyroxene (Px) (PPL). (b) Amphiboles with inclusions of pyroxene, surrounded by plagioclase (Pl) (XPL). (c) Biotite having inclusions of plagioclase feldspar (XPL). (d) Biotite having inclusions of plagioclase feldspar (PPL). PPL, plane polarised light; XPL, crossed polarised light.*

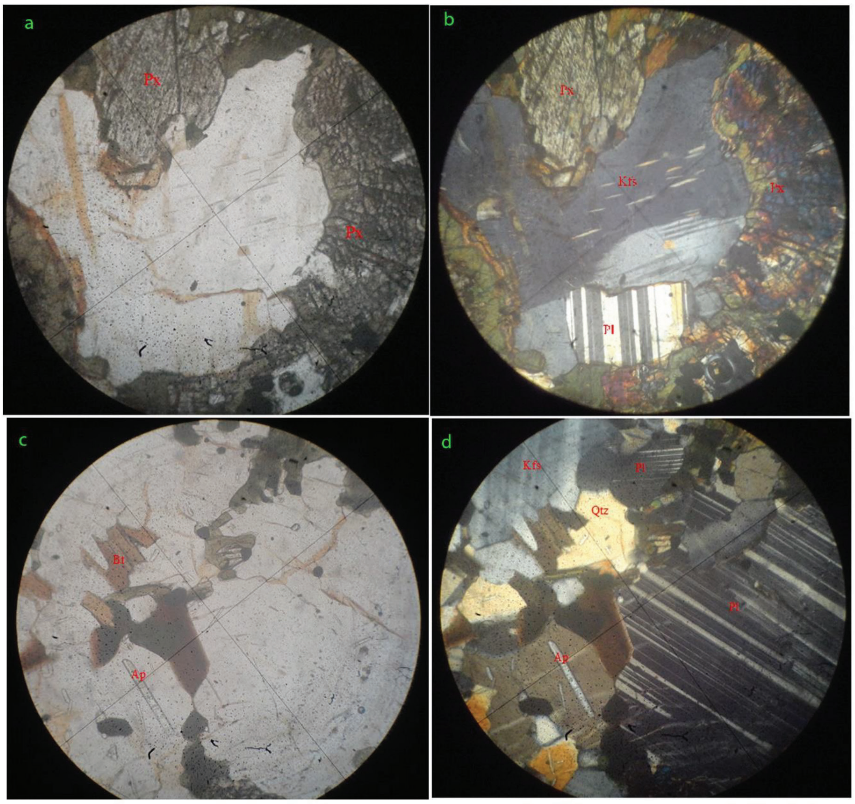

Figure 8. *Photomicrographs showing: (a) pyroxene in close contact with areas occupied by transparent minerals: plagioclase and K-feldspar. Altered biotite (brownish mineral) surrounded by transparent mineral (PPL). (b) Pyroxene (Px), perthitic K-feldspar (Kfs) and plagioclase feldspar (Pl). The straight lamellae in the perthite (XPL). (c) Biotite (Bt) and apatite. The smaller needle-shaped apatite crystals (PPL). (d) K-feldspar (Kfs), quartz (Qtz), apatite (Ap) and plagioclase (Pl) (XPL). PPL, plane polarised light; XPL, crossed polarised light.*

which thus defines the foliation. The biotite grains have inclusions of plagioclase and apatite (Figure 7c and 7d). Plagioclase occurs as porphyroblasts, and grains are almost equidimensional. Plagioclase crystals observed exhibit both ablite and carlsbard twinning. There is a close association between plagioclase and pyroxene. Plagioclase occurs as inclusions in both pyroxene and biotite, and plagioclase crystals occur at the margins of amphiboles. K-feldspar has perthitic texture and is in close contact with pyroxene (Figure 8a and 8b). Apatite is needle-like and colourless, occurring as inclusions in feldspars (Figures 8c and 8d).

Mineral Chemistry

Pyroxene: The mineral composition of pyroxene in charnockitic gneiss shows a slight variation from core to rim (Table 1). The range in composition for both the core and rim is: SiO_2: 49.68–49.82%, MgO: 15.20–15.07%, FeO: 31.91–32.19% and CaO: 0.495–0.618%. This result confirms the orthopyroxene as hypersthene and the formula can be written as $MgFeSi_2O_6$ (Table 1). In terms of the pyroxene end members, the formula can be written as $En_{45}Fs_{54}Wo_1$ (Table 1). The BSE image shows no form of zoning (Figure 5b), while the compositional maps show the levels of element in the minerals (Figure 6). The compositional maps show high levels of magnesium (Mg) and iron (Fe), but a very low level of calcium (Ca) in the pyroxene (Px).

Amphibole: The composition of the various oxides is (Table 1): SiO_2: 42.45%, TiO_2: 2.038%, FeO: 18.10%, Al_2O_3: 10.39%, MgO: 9.16%, CaO: 11.30%, Na_2O: 1.53%, K_2O: 1.41% and Cl: 0.071%. The compositional maps (Figure 6) show amphibole with an appreciable amount of Fe, Ca and Mg but very low Na content. The formula of the amphibole is $(K,Na)(Ca,Fe)_2(Mg,Fe,Ti,Al)_5(Al,Si)_8O_{22}(OH)_2$ that is named as hornblende (Table 1).

Biotite: The chemical composition of biotite crystals is (Table 2): SiO_2: 34.71–35.95%, FeO: 19.97–20.97%, MgO: 9.64–10.15%, Al_2O_3: 13.35–14.14%, TiO_2: 4.84–5.23%, CaO: 0–0.07% and K_2O: 8.54–9.74%. The elemental composition of the biotite shows that it is annite.

Plagioclase: The chemical composition of 14 crystals of plagioclase shows the following range of values: SiO_2: 58.14–60.19%, Al_2O_3: 24.06–25.77%, CaO: 7.18–8.58%, Na_2O: 5.99–7.35% and K_2O: 0.34–0.49%, and in terms of anorthite content it can be written as $Ab_{59}An_{39}Or_{2,}$ that is known as andesine (Figure 9). The chemical formula of the plagioclase based on cations is $(Na,Ca)AlSi_3O_8$ (Table 3).

Table 1. *The chemical composition of pyroxene and amphibole*

	Pyroxene			Amphibole					
Sample	**1c**	**1r**	**Crystal**	**1**	**2**	**3**	**4**	**5**	**6**
SiO_2	49.680	49.830	SiO_2	42.453	41.804	43.680	42.904	43.139	42.786
TiO_2	0.037	0.114	TiO_2	2.038	1.450	1.505	1.669	1.826	1.993
Al_2O_3	0.618	0.682	Al_2O_3	10.389	10.342	9.819	10.039	10.174	10.186
FeO	32.470	31.910	FeO	18.095	17.894	17.156	18.178	18.975	18.580
Cr_2O_3	0.000	0.010	Cr_2O_3	0.000	0.000	0.043	0.132	0.053	0.101
MnO	0.585	0.712	MnO	0.058	0.016	0.111	0.132	0.049	0.054
MgO	15.200	15.070	MgO	9.163	9.361	9.943	9.474	9.399	9.622
CaO	0.618	0.495	CaO	11.305	11.394	11.575	11.465	11.431	11.455
Na_2O	0.014	0.055	Na_2O	1.533	1.338	1.108	1.386	1.406	1.443
K_2O	0.057	0.030	K_2O	1.409	1.430	1.215	1.411	1.347	1.349
Total	99.290	98.900	Cl	0.071	0.085	0.063	0.077	0.043	0.140
TSi	1.958	1.970	Total	96.510	95.110	96.180	96.740	97.79	97.610

Table 1. *The chemical composition of pyroxene and amphibole (continue)*

Pyroxene			Amphibole						
Sample	**1c**	**1r**	**Crystal**	**1**	**2**	**3**	**4**	**5**	**6**
TAl	0.029	0.030	O_Cl	0.020	0.020	0.010	0.020	0.010	0.030
TFe^{3+}	0.014	0.000	TSi	6.553	6.517	6.681	6.580	6.556	6.512
M1Al	0.000	0.002	TAl	1.447	1.483	1.319	1.420	1.444	1.488
M1Ti	0.001	0.003	Sum_T	8	8	8	8	8	8
M1Fe^{3+}	0.044	0.026	CAl	0.442	0.416	0.449	0.393	0.377	0.337
M1Fe^{2+}	0.062	0.080	CFe^{+3}	0.000	0.038	0	0	0	0
M1Cr	0.000	0.000	CTi	0.237	0.170	0.173	0.193	0.209	0.228
M1Mg	0.893	0.888	CMg	2.109	2.176	2.267	2.166	2.129	2.183
M2Mg	0.000	0.000	CFe^{+2}	2.213	2.201	2.106	2.232	2.279	2.240
M2Fe^{2}	0.950	0.949	Sum_C	5	5	5	5	5	5
M2Mn	0.020	0.024	BFe^{+2}	0.123	0.095	0.089	0.099	0.132	0.125
M2Ca	0.026	0.021	BMn	0.008	0.002	0.014	0.017	0.006	0.007
M2Na	0.001	0.004	BCa	1.870	1.903	1.897	1.884	1.861	1.868
M2K	0.003	0.002	Sum_B	2	2	2	2	2	2
Sum (cat)	3.997	3.998	ANa	0.459	0.404	0.329	0.412	0.414	0.426
Ca	1.337	1.069	AK	0.277	0.284	0.237	0.276	0.261	0.262
Mg	45.770	45.260	Sum_A	0.736	0.689	0.566	0.688	0.675	0.688
Fe2_Mn	52.890	53.670	Sum_cat	15.736	15.689	15.566	15.688	15.675	15.688
JD1	0.000	0.108	CCl	0.019	0.022	0.016	0.020	0.011	0.036
AE1	0.202	0.186	Sum_oxy	23.102	23.000	23.023	23.031	23.016	23.002
CFTS1	2.056	1.168							
CTTS1	0.056	0.174							
CATS1	0.000	0.000							
WO1	0.000	0.000							
EN1	45.780	45.560							
FS1	51.902	52.800							
Q	1.931	1.939							
J	0.002	0.008							
WO	1.299	1.055							
EN	44.460	44.670							
FS	54.240	54.280							
WEF	99.890	99.570							
JD	0.000	0.032							
AE	0.100	0.396							

M1, third octahedral site; M2, second octahedral site; M3, first octahedral site; T, tetrahedral site; JD, jadeite; AE, aegirine; WO, wollastonite; EN, enstatite; FS, ferrosilite; CAT, cation.

Table 2. *Chemical composition of biotite crystals*

Crystal	1	2	3	4	5	6	7	8
SiO_2	35.20	35.10	35.19	34.71	35.52	35.34	35.95	35.42
TiO_2	5.23	5.15	4.97	4.84	4.84	4.97	5.09	5.00
Al_2O_3	13.63	13.79	14.14	13.75	13.92	13.35	13.82	13.83
Cr_2O_3	0.04	0.06	0.00	0.03	0.02	0.05	0.03	0.00
FeO	21.02	20.48	20.75	20.96	19.97	20.59	20.41	20.72
MnO	0.00	0.04	0.03	0.03	0.00	0.01	0.00	0.02
MgO	9.88	9.95	10.15	9.93	10.00	10.07	9.99	9.64
CaO	0.01	0.07	0.00	0.04	0.02	0.00	0.00	0.04
Na_2O	0.13	0.11	0.09	0.14	0.09	0.08	0.14	0.11
K_2O	9.74	9.71	9.57	9.62	9.56	8.54	9.63	9.74
Cl	0.15	0.11	0.12	0.15	0.09	0.09	0.10	0.10
H_2O	1.80	1.81	1.81	1.78	1.81	1.80	1.83	1.81
Total	95.03	94.57	95.01	94.2	94.03	93.09	95.16	94.62
Si	5.739	5.735	5.717	5.714	5.803	5.823	5.812	5.782
AlIV	2.261	2.265	2.283	2.286	2.197	2.177	2.188	2.218
AlVI	0.356	0.388	0.423	0.380	0.481	0.414	0.443	0.441
Ti	0.641	0.633	0.607	0.599	0.595	0.616	0.619	0.614
Fe^{2+}	2.866	2.798	2.819	2.885	2.729	2.837	2.759	2.829
Cr	0.005	0.008	0.000	0.004	0.003	0.007	0.004	0.000
Mn	0.000	0.006	0.004	0.004	0.000	0.001	0.000	0.003
Mg	2.401	2.423	2.458	2.437	2.436	2.474	2.408	2.346
Ca	0.002	0.012	0.000	0.007	0.004	0.000	0.000	0.007
Na	0.041	0.035	0.028	0.045	0.029	0.026	0.044	0.035
K	2.026	2.024	1.984	2.020	1.993	1.795	1.986	2.028
Cations	16.338	16.327	16.323	16.381	16.270	16.170	16.263	16.303
CCl	0.083	0.061	0.066	0.084	0.050	0.050	0.055	0.055
OH	1.959	1.970	1.967	1.958	1.975	1.975	1.973	1.972
O	24	24	24	24	24	24	24	24
Fe/(Fe + Mg)	0.5400	0.54	0.530	0.540	0.530	0.530	0.530	0.550
Mg/(Fe + Mg)	0.460	0.460	0.470	0.460	0.470	0.470	0.470	0.450

AlIV, aluminium in tetrahedral site; AlVI, aluminium in octahedral site.

Table 3. *The chemical composition of plagioclase crystals*

Crystal	1	2	3	4	5	6	7	8	9	10	11	12	13	14
SiO_2	58.96	59.05	59.39	59.47	58.84	58.19	58.45	59.22	59.23	58.7	59.76	60.19	58.14	58.57
TiO_2	0.02	0	0	0	0.04	0	0.37	0.01	0	0	0.04	0	0.03	0
Al_2O_3	25.53	25.59	25.55	25.03	25.72	25.77	25.8	25.65	25.34	25.26	24.06	24.78	25.24	25.49
FeO	0.12	0.07	0.05	0.15	0.02	0.07	0.24	0.07	0.11	0.17	0	0.08	0.01	0.01
MnO	0.01	0.01	0.05	0.02	0.01	0.04	0	0.03	0	0.04	0.02	0	0	0
MgO	0	0.01	0	0	0.01	0	0	0	0.02	0	0	0.01	0	0
BaO	0.01	0.04	0.08	0.05	0.07	0	0.07	0.03	0.09	0	0.06	0.01	0.08	0.03
CaO	8.05	8.04	7.98	7.82	8.13	8.58	8.49	8.21	7.78	7.88	7.18	7.3	8.34	8.15
Na_2O	6.87	6.88	5.99	7.04	6.75	6.7	6.26	6.62	6.93	7.01	7.35	7.35	6.07	6.53
K_2O	0.38	0.37	0.39	0.39	0.34	0.37	0.36	0.34	0.37	0.36	0.49	0.41	0.37	0.39
Total	99.95	100.06	99.48	99.97	99.93	99.72	100.04	100.18	99.87	99.42	98.96	100.13	98.28	99.17
Si	2.639	2.64	2.659	2.661	2.633	2.616	2.617	2.642	2.651	2.642	2.697	2.683	2.642	2.639
Al	1.346	1.347	1.347	1.319	1.356	1.364	1.36	1.347	1.336	1.339	1.279	1.301	1.351	1.353
Fe3$^+$	0	0	0	0	0	0	0	0	0	0	0	0	0	0
Ti	0.001	0	0	0	0.001	0	0.012	0	0	0	0.001	0	0.001	0
Fe2$^+$	0.004	0.003	0.002	0.006	0.001	0.003	0.009	0.003	0.004	0.006	0	0.003	0	0
Mn	0	0	0.002	0.001	0	0.002	0	0.001	0	0.002	0.001	0	0	0
Mg	0	0.001	0	0	0.001	0	0	0	0.001	0	0	0.001	0	0
Ba	0	0.001	0.001	0.001	0.001	0	0.001	0.001	0.002	0	0.001	0	0.001	0.001
Ca	0.386	0.385	0.383	0.375	0.39	0.413	0.407	0.392	0.373	0.38	0.347	0.349	0.406	0.393
Na	0.596	0.596	0.52	0.611	0.586	0.584	0.543	0.573	0.602	0.612	0.643	0.635	0.535	0.571
K	0.022	0.021	0.022	0.022	0.019	0.021	0.021	0.019	0.021	0.021	0.028	0.023	0.021	0.022
Cations	4.994	4.995	4.937	4.997	4.989	5.003	4.971	4.979	4.992	5.002	4.998	4.995	4.958	4.98
X	3.986	3.987	4.006	3.98	3.99	3.98	3.989	3.989	3.987	3.981	3.977	3.984	3.994	3.992
Z	1.008	1.007	0.93	1.016	0.998	1.023	0.981	0.989	1.003	1.021	1.02	1.011	0.963	0.987
Ab	59.4	59.5	56.2	60.6	58.9	57.4	55.9	58.2	60.4	60.4	63.2	63.1	55.6	57.9
An	38.4	38.4	41.4	37.2	39.2	40.6	41.9	39.8	37.4	37.5	34.1	34.7	42.2	39.9
Or	2.2	2.1	2.4	2.2	1.9	2.1	2.2	1.9	2.1	2.1	2.8	2.3	2.2	2.2

Ab, albite; An, anorthite; Or: orthoclase.

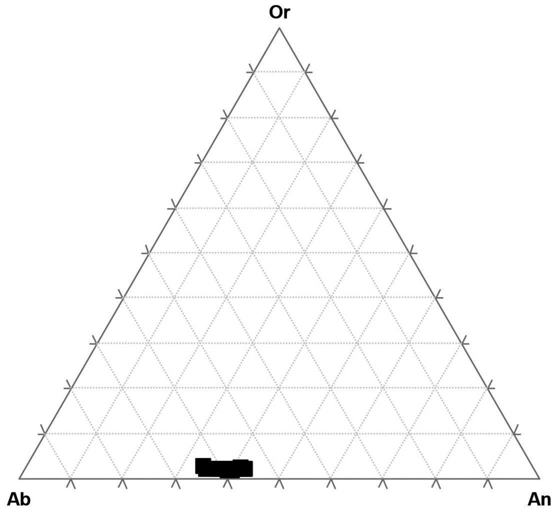

Figure 9. *Ternary diagram showing feldspar solid solution.*

Ilmenite: The result of the chemical composition of ilmenite for charnockitic gneiss shows the following values (Table 4): TiO_2: 50.79%, FeO: 46.37% and SiO_2: 0.046%.

Major Element Geochemistry

The composition of the major oxides is as follows (Table 5): SiO_2 (50.93 wt%), Al_2O_3 (15.51 wt%), CaO (7.79 wt%), Fe_2O_3 (12.3 wt%), MgO (5.14 wt%), K_2O (1.01 wt%), MnO (0.15 wt%), Na_2O (3.33 wt%), TiO_2 (2.15 wt%), P_2O_5 (0.65 wt%), and Cr_2O_3 (0.02 wt%).

Trace Element Geochemistry

For the compatible elements Zn, Cr and V, the value ranges are as follows (Table 5): Zn (124.1 ppm), Cr (95.31 ppm) and V (188.28 ppm). The immobile transition elements Co and Ni have values of 107.09 and 52.36 ppm, respectively. The incompatible elements show a wide variation, and the large ion lithophile elements (LILE) have the values of Cs (0.31 ppm), Sr (583.8 ppm), Rb (18.36 ppm) and Ba (479.77 ppm).

Rare Earth Elements Geochemistry

The rare earth elemental (REE) composition of the charnockitic gneiss shows light REE (LREE) enrichment and depletion of heavy REE (HREE) (Table 5). The samples display a pattern of negative Eu anomaly.

Discussion

The orthopyroxene found in the charnockitic gneiss of Iboropa is hypersthene, that is Fe-Mg-rich (Table 1) and it is associated with amphibole (hornblende) and plagioclase. Pyroxene analysed is a solid solution between enstatite and ferrosilite ($En_{45}Fs_{54}Wo_1$), and because of the high Fe content it can be referred to as ferrohypersthene. Orthopyroxene is an essential mineral for all rocks in the charnockite suite.

Table 4. *The composition of ilmenite in a charnockitic gneiss*

Sample	1
SiO_2	0.046
TiO_2	50.787
Al_2O_3	0.02
FeO	46.372
Cr_2O_3	0.075
MnO	0.477
MgO	0.267
CaO	0
Na_2O	0.061
Total	98.11
Si	0.001
Al	0.001
Ti	0.986
Fe^{2+}	1.001
Cr	0.002
Mn	0.01
Mg	0.01
Ca	0
Na	0.003
Cations	2.014

The percentage of CaO in the analysed pyroxene is very low (0.5–0.6%), a value which is less than 1.0 and is consistent with the fact that Ca atoms per formula does not exceed 1.0, which occurs only in the M2 site [30]. The aluminium oxide content of the pyroxene is also low. Orthopyroxene can be found to be metamorphic because the weight percentage of MgO + FeO_T is greater than 44.00% [31]. Orthopyroxene present could have formed during increase in grade of metamorphism from either hornblende or biotite. In Northern Nigeria, charnockite has been derived from the transformation of biotite by the addition of ferrous iron-rich juvenile

Table 5. *Bulk rock composition of charnockitic gneiss; major elements (%), trace elements (ppm), REE (ppm)*

Major element	1	Trace element	1	REE	1
Wt%		ppm		ppm	
SiO_2	50.93	V	188.28	La	57.71
Al_2O_3	15.51	Cr	95.31	Ce	119.2
CaO	7.79	Co	107.09	Pr	14.13
Fe_2O_3	12.3	Ni	52.36	Nd	54.64
MgO	5.14	Cu	41.17	Sm	9.05
K_2O	1.01	Zn	124.1	Eu	2.27
MnO	0.15	Rb	18.36	Gd	7.325
Na_2O	3.33	Sr	583.8	Tb	0.856
TiO_2	2.15	Zr	294.09	Dy	4.365
P_2O_5	0.65	Nb	20.61	Ho	0.8
Cr_2O_3	0.02	Mo	1.54	Er	2.02
LOI	0.34	Cs	0.31	Tm	0.251
Total	99.32	Ba	479.77	Yb	1.63
		Hf	6.49	Lu	0.22
		Ta	1.08	Total	274.4
		Pb	8.51	La_N/Yb_N	25.39
		Th	2.89	Gd_N/Yb_N	3.72
		U	0.45	Eu_N/Eu_N^*	0.852
				Ce/Ce*	1.153

solution [32]. Orthopyroxene could be formed by any of the following reactions:

Hornblende + Quartz =>
Clinopyroxene + Orthopyroxene + (1)
Plagioclase + K-feldspar + H_2O

Biotite + Quartz => (2)
Orthopyroxene + K-feldspar + H_2O

The earlier reactions are dehydration reactions resulting in a decrease in the activity of water and an increase in alkali activity [19]. Mineral assemblage show altered form of biotite (first-generation biotite) in close association with K-feldspar (Figure 8a). This process is a high-grade dehydration of rocks of the amphibolite facies to granulite facies and it can involve partial melting and in some cases fluid solid-state dehydration [33–35]. Orthopyroxene mantled by amphibole is an indication of retrogressive metamorphic event (Figure 5). The retrogression of the charnockite could be due to various dehydration processes [36]. Retrogression involving the breakdown of orthopyroxene is quite common in granulite complexes [37, 38]. Orthopyroxene replaced by amphibole has been described in the granulite facies of gneiss in the granite Falls-Montevideo [39]. The hypersthene observed has numerous microfractures that may serve as a pathway for the movement of fluids (Figure 4a). The development of biotite along cleavage planes (Figure 4a) is also an indication of retrogression [40]. Amphibole could have been formed by a process in which orthopyroxene reacts with plagioclase (anorthite-rich) and quartz in the presence of water, and this can be represented by the following equation:

Orthopyroxene + Plagioclase 1 + (3)
Quartz + H_2O => Amphibole + Plagioclase 2

In this process, amphibole replaces orthopyroxene in a rehydration reaction. Biotite (second-generation biotite) that is in close contact with orthopyroxene (Figure 4a) could have been a product of a reaction in which K-feldspar is consumed by a rehydration process, and thus it can be represented by the following equation:

Orthopyroxene + K-feldspar + H_2O => Biotite (4)

The biotite is annite-rich, an iron end member of biotite as indicated by the mineral chemistry (Table 2). Such retrogressive reactions have been found to result from fluid (CO_2 and H_2O) activity and oxygen fugacity in the later stages of dehydration zone [41]. Based on the BSE image and elemental maps (Figures 5b and 6), there is no evidence of zoning in the pyroxene crystals. Hornblende and biotite in charnockites have been found to be due to retrogressive metamorphism of pyroxene granulite facies rocks [42, 43], and retrograde form of metamorphism has been found to obliterate the mineralogy of the granulite facies [24]. Plagioclase occurring as inclusions in pyroxene and biotite is an indication that it was formed very early enough as primary minerals. Opaque minerals that are concentrated along the cleavage planes of amphiboles crystals are evidences of metamorphic alteration. The Al_2O_3 content of the amphibole is fairly high, and chornockitic rocks usually have Al_2O_3 higher than that of the normal igneous rocks. Hornblende has less magnesium than the coexisting orthopyroxene and a moderate composition of TiO_2 (2.04%). Hornblende has high TiO_2 (>2) which some authors have linked to the increase in the grade of metamorphism, and this link between temperature and Ti content of amphibole has been reported [44, 45]. There is a high value of TiO_2 (4.84–5.23%) in biotite, an indication that it is uniformly rich in Ti, and a higher value of X_{Fe} to X_{Mg}. Biotite could have reacted with quartz to give the Fe-Ti ilmenite. There has been suggestion that increasing Ti content leads to increase in the stability field of biotite [46]. The crystals of biotite have MgO of nearly the same range of composition as that of amphiboles but far less than that of orthopyroxene. Plagioclase is the dominant feldspar observed and it is albite-enriched ($Ab_{55.9}An_{41.9}Or_{2.2}$–$Ab_{63.2}An_{34.1}Or_{2.8}$) that is andesine and is indicative of amphibolite zone. The K-feldspar has perthitic texture (Figure 8b). Perthite is an intergrowth of one feldspar within another, albite in orthoclase [47], and it is common in high-grade metamorphic rocks [48] due to the high temperature involved. The perthite observed has straight lamellae (Figure 7b), an indication of granulite facies. Based on the association of orthopyroxene and plagioclase, the granulite can be said to be of intermediate pressure [24], and one of the feature of this facies is the depletion of Th and U. The values of Cs have also been found to be depleted in high-grade metamorphosed rocks [24]. There is a depletion in the values of K, Rb, Th and U, and pyroxene gneiss with values of this nature has been suggested as a residue of partial melting in which there has been the removal of these elements from the original rocks [49]. The elements Th, U, Rb and Cs are usually present in the lattices of micas of the amphibolite facies but there is breaking down of micas to K-feldspar in the granulite facies, and K-feldspar do not concentrate Rb and Cs [24]. The Sr value in this rock is high, which might compound the low value of Rb, thus giving rise to low Rb/Sr ratio. REE patterns show LREE enrichment, and HREE-depleted patterns with negative Eu anomaly (Table 5), suggesting that this charnockitic gneiss of Iboropa could have been formed by partial melting and crystallisation. The enrichment of LREE and negative Eu anomaly are similar to the charnockitic rocks of Ado-Ekiti area of Nigeria [50]. The negative Eu anomaly reflects an intracrustal form of differentiation of the original igneous parent rock [51].

Conclusion

The detailed petrographic observation and the mineral assemblage suggest a retrograde metamorphic reaction. There are two generations each for biotite and plagioclase feldspar. The first-generation biotite is altered and it is concentrated in and around plagioclase as well as K-feldpar, while the second-generation biotite surrounds orthopyroxene. The high-grade minerals such as hypersthene and plagioclase gave rise to hydrous minerals amphiboles and biotite. Fluids responsible for the hydration reaction could have been transported along the numerous microfractures within the hypersthene grains. The presence of straight lamellae in the perthite is an evidence of granulite facies. The charnockitic gneiss could have been resulted from a partial melting process.

Acknowledgements

The use of JEOL JXA 8230 Superprobe, instrument sponsored by NRF/NEP grant 40113 (UID 74464) at Rhodes University, Grahamstown South Africa, is kindly acknowledged. The financial support from Tertiary Education Trust Fund (TETFUND) is recognised.

References

[1] Holland, T.H. (1900): The charnockite series, a group of Archean hypersthenic rocks in Peninsular India. *Memoir Geological Survey of India*, 28, 192–249.

[2] Anantha, I., T.R., N.K. (1978): Geochemical Comparison of Archaean Granulites in India with Proterozoic Granulites in Canada.

[3] Dobmeier, C., Raith, M.M. (2000): On the origin of 'arrested' charnockitization in the Chilka Lake area, Eastern Ghats Belt, India: a reappraisal. *Geological Magazine*, 137(1), pp. 27–37.

[4] Ghosh, J.G., de Wit, M.J., Zartman, R.E. (2004): Age and tectonic evolution of Neoproterozoic ductile shear zones in the Southern Granulite Terrain of India, with implications for Gondwana studies. *Tectonics*, 23(3), pp. 1–38.

[5] Rajesh, H.M., Santosh, M. (2004): Charnockitic magmatism in southern India. *Proceedings of the Indian Academy of Sciences - Earth & Planetary Sciences*, 113(4), pp. 565–585.

[6] Le Maitre, R.W. (2002): *Igneous Rocks: A Classification and Glossary of Terms*. Cambridge University Press: Cambridge, 256 p.

[7] Frost, B.R., Frost, C.D. (2008): On charnockites. *Gondwana Research*, 13, pp. 30–44.

[8] Rajesh, H.M., Santosh, M. (2012): Charnockites and charnockites. *Geoscience Frontiers,* 3, pp. 737 –744.

[9] Janardhan, A.S., Jayananda, M., Shankara, M.A. (1994): Formation and tectonic evolution of granulites from Biligirirangam and Nilgiri Hills, south India: Geochemical and isotopic constraints. *Journal of the Geological Society of India*, 44, pp. 27–40.

[10] Friend, C.R.L. (1981): Charnockite and granite formation and influx of CO_2 at Kabbaldurga. *Nature*, 294, pp. 550–552.

[11] Hansen, E.C., Janardhan, A.S., Newton, R.C., Prame, W.K.B., Kumar, G.R.R. (1987): Arrested charnockite formation in southern India and Sri Lanka. *Contributions to Mineralogy and Petrology*, 96, pp. 225–244.

[12] Srikantappa, C., Raith, M., Touret, J.L.R. (1992): Synmetamorphic high-density carbonic fluids in the lower crust: evidence from the Nilgiri granulites, Southern India. *Journal of Petrology*, 33(4), pp. 733–760.

[13] Raith, M., Srikantappa, C. (1993): Arrested charnockite formation at Kottavattam, Southern India. *Journal of Metamorphic Geology*, 11(6), pp. 815–832.

[14] Harley, S.L., Santosh, M. (1995): Wollastonite at Nuliyam, Kerala, South India: A reassessment of CO_2 infiltration and charnockite formation at a classic locality. *Contributions to Mineralogy and Petrology*, 120, pp. 83–94.

[15] Yoshida, M., Santosh, M. (1994): A tectonic perspective of incipient charnockites in East Gondwana. *Precambrian Research*, 66(1–4), pp. 379–392.

[16] Newton, R.C., Hansen, E.C. (1983): The origin of Proterozoic and late Archaean charnockites-evidence from field relations and experimental petrology. *Geological Society of America Memorials,* 161, pp. 167–178.

[17] Condie, K.C., Bowling, G.P., Allen, P. (1986): Origin of granites in an Archean high-grade terrane, southern India. *Contributions to Mineralogy and Petrology*, 92(1), pp. 93–103.

[18] Bhattacharya, S. (2010): The charnockite problem, a twenty first century perspective. *Natural Science*, 2(04), p. 402.

[19] Perchuk, L.L., Gerya, T.V. (1993): Fliud control of charnockitization. *Chemical Geology*, 108, pp 175–186.

[20] Touret, J.L., Huizenga, J.M. (2012): Fluid-assisted granulite metamorphism: a continental journey. *Gondwana Research*, 21(1), pp. 224–235.

[21] Yang, Q.Y., Santosha, M., Tsunogaec, T. (2014): First report of Paleoproterozoic incipient charnockite from the North China Craton: Implications for ultrahigh-temperature metasomatism. *Precambrian Research*, 243, pp. 168–180.

[22] Rahaman, M.A. (1976): Review of the basement geology of Southwestern Nigeria. In: *Geology of Ni-*

geria, C.A. Kogbe (ed.). Elizabethan Publishing Co.: Lagos, pp. 41–58.

[23] Rahaman, M.A., Ocan, O. (1978): On relationships in the Precambrian migmatitic gneisses of Nigeria. *Nigerian Journal of Mining and Geology*, 15, pp. 23–32.

[24] Heier, K.S. (1973): A Discussion on the evolution of the Precambrian crust-Geochemistry of granulite facies rocks and problems of their origin. *Philosophical Transactions of the Royal Society of London. Series A, Mathematical and Physical Sciences*, 273(1235), pp. 429–442.

[25] Hubbard, F.H. (1975): Precambrian crustal development in western Nigeria: indications from the Iwo region. *Bulletin of the Geological Society of America*, 86, pp. 548–554.

[26] Ferré, E.C., Caby, R. (2007): Granulite facies metamorphism and charnockite plutonism: examples from the Neoproterozoic Belt of northern Nigeria. *Proceedings of "the Geologists' Association,* US, 47–54.

[27] Sacchi, R. (1968): The geology of Kabba-Lokoja region in south-western Nigeria. *Bolletino della Società geologica italiana*, 87, 341–367.

[28] Dempster A.N. (1967): (GSN). 1:250,000 Sheet 61, Akure.

[29] Rahaman, M.A., Ocan, O. (1988): The Nature of Granulite of Granulite Facies Metamorphism in Ikare Area, Southwestern Nigeria. In: *Precambrian Geology of Nigeria*. GSN pub., pp. 157–163.

[30] Cameron, M., Papike, J.J. (1981). Structural and chemical variations in pyroxenes. *American Mineralogist*, 66(1–2), pp. 1–50.

[31] Bhattacharyya, C. (1971): An evaluation of the chemical distinctions between igneous and metamorphic orthopyroxenes. *American Mineralogist: Journal of Earth and Planetary Materials*, 56(3–4_Part_1), pp. 499–506.

[32] Oyawoye, M.O. (1964): The contact relationship of charnockite and granite gneiss at Bauchi, Northern Nigeria: *Geological Magazine*, v. 101, pp. 138–144.

[33] Harlov, D.E., Johansson, L., Van Den Kerkhof, A., Förster, H.J. (2006a): The role of advective fluid flow and diffusion during localized, solid-state dehydration: Söndrum Stenhuggeriet, Halmstad, SW Sweden. *Journal of Petrology*, 47(1), pp. 3–33.

[34] Rigby, M.J., Droop, G.T.R. (2011): Fluid-absent melting versus CO2 streaming during the formation of pelitic granulites: A review of insights from the cordierite fluid monitor. *Origin and evolution of Precambrian high-grade gneiss terranes, with special emphasis on the Limpopo complex of Southern Africa*, 207, p. 39.

[35] Harlov, D.E. (2012): The potential role of fluids during regional granulite-facies dehydration in the lower crust. *Geoscience Frontiers*, 3(6), pp. 813–827.

[36] Ravindra Kumar, G.R., Chacko, T. (1986): Mechanisms of charnockite formation and breakdown in southern Kerala: implications for the origin of the southern Indian granulite terrain. *Journal of the Geological Society of India*, 28(4), pp. 277–288.

[37] Lasnier, B. (1977): *Persistance d'une série granulitique au coeur du Massif Central français, Haut-Allier: les termes basiques, ultrabasiques et carbonates*. Ph.D. Thesis. Université de Nantes, laboratoire de pétrologie et de minéralogie: Nantes, 351 p.

[38] Srikantappa, C., Prakash Narasimha, K.N. (1988): Retrogression of charnockites in Moyar Shear Zone, Tamil Nadu. *Journal of the Geological Society of India*, 11, pp. 117–124.

[39] Himmelberg, G.R., Phinney, W.C. (1967): Granulite-Facies Metamorphism, Granite Falls-Montevideo Area, Minnesota. *Journal of Petrology*, 8(3), pp. 325–348.

[40] Allen, P., Condie, K.C., Narayana, B.L. (1985): The geochemistry of prograde and retrograde charnockite-gneiss reactions in southern India. *Geochimica et Cosmochimica Acta*, 49(2), pp. 323–336.

[41] Oyawale, A.A., Ocan O.O. (2020): Migmatization process and the nature of transition from amphibolite to granulite facies metamorphism in Ikare area Southwestern Nigeria. *Journal of Geology and Mining Research*, 12(2), pp. 45–64.

[42] Cooray, P.G. (1961): The Geology of the area around Rangala: *Ceylon Geol. Survey Mem*., 2, 138 p.

[43] Cooray, P.G. (1962): Charnockites and their associated gneisses in the Pre-Cambrian of Ceylon. *The Quarterly journal of the Geological Society of London*, 118, pp. 239–273.

[44] Raase, P. (1974): Al and Ti contents of hornblende, indicators of pressure and temperature of regional metamorphism. *Contributions to mineralogy and petrology*, 45(3), pp. 231–236.

[45] Spear, F.S. (1981): An experimental study of hornblende stability and compositional variability in amphibolite. *American Journal of Science*, 281(6), pp. 697–734.

[46] Dymek, R.F. (1983): Titanium, aluminum and interlayer cation substitutions in biotite from high-grade gneisses, West Greenland. *American Mineralogist*, 68(9–10), pp. 880–899.

[47] Spry, A. (1969): *Metamorphic Textures*. Pergamon Press, Oxford: England, 358 p.

[48] Cayzer, N. (2002): *Feldspar microtextures and the cooling histories of high-grade terrains.* Ph.D. Thesis. University of Edinburgh, U.K., 300 p.

[49] Fyfe, W.S. (1973): The granulite facies, partial melting and the Archaean crust. *Philosophical Transactions of the Royal Society of London. Series A*, 273, pp. 457–461.

[50] Olarewaju, V.O. (1987): Charnockite-granite association in SW Nigeria: rapakavi granite type and charnockitic plutonism in Nigeria? *Journal of African Earth Sciences*, 6(1), pp. 67–77.

[51] Bhattacharya, S. Chaudhary, A.K., Basei, M. (2012): Original nature and source of Khondalites in the Eastern Ghats Province, India. *Geological Society, London, Special Publications*, 365, 147–159.

Original scientific article

Received: Dec 02, 2020
Received: Dec 07, 2020
DOI: 10.2478/rmzmag-2020-0014

High-resolution Biostratigraphic Studies of Step-1 Well, Offshore, Western Niger Delta

Visoko resolucijske biostratigrafske preiskave morske vrtine Step-1 na območju zahodne delte reke Niger

M. E. Nton* and S. O. Famori*
Department of Geology, University of Ibadan, Ibadan, Nigeria
*Corresponding author: E-mail: ntonme2009@gmail.com, sfamori@yahoo.com

Abstract

A high-resolution biostratigraphic study of the STEP-1 well, offshore Western Niger Delta Basin, Nigeria, was carried out using foraminifera, calcareous nannofossils and palynomorphs. The study was aimed at identifying the biostratigraphic zones, age deductions as well as palaeoenvironmental and palaeoclimatic reconstructions. From the studied well section of 609 m (1,829–2,438 m), 50 ditch cuttings were used for foraminifera and calcareous nannofossils, while 25 samples were used for palynological studies at 12 m and 24 m intervals, respectively. Standard laboratory preparation techniques were employed for the three microfossil groups. Due to the occurrence of some forms such as *Globigerina praebulloides*, *Haplophragmoides spp, Bolivina scalprata miocenica, Valvulina flexilis and Cyclammina cf.* minima, two planktonic and one benthonic foraminifera zones were identified as follows: Lower N18, Upper N17 zone (early Pliocene, late Pliocene) and *Cyclammina minima* zone (late Miocene), respectively. Two biozones were recognized for the nannofossils and include NN12 (*Ceratolithus cristatus zone*) and NN11 (*Discoaster berggrenii* zone). These zones were assigned to early Pliocene and late Miocene, respectively. Other forms include *Discoaster pentaradiatus, Sphenolithus abies* and *Ceratolithus armatus. Echitricolporites spinosus*/ P800zone has been assigned for the Palynomorph assemblages and was dated late Miocene due to the quantitative occurrence of *Cyperaceaepollis spp*. Four identified major condensed sections include intervals at 1,926, 1,987, 2,097 and 2,316 m, which have been dated 5.0, 5.8, 6.3 and 7.0 Ma, respectively. Based on the benthonic foraminiferal species and Palynological Marine Index, a shallow marine environment is deduced for the studied interval which was interpreted to be deposited under both wet and dry palaeoclimatic conditions. The findings, no doubt could serve as a template for a sequence stratigraphic model, generally beyond the resolution of seismic stratigraphy.

Keywords: drilling regime, roller cone bit, wear, reduced penetration rate, change of the material properties.

Izvleček

Z uporabo alg luknjičark, apnenčastih nanofosilov in palinomorf so bile na območju zahodne delte reke Niger izvedene visoko resolucijske biostratigrafske preiskave morske vrtine STEP-1. Namen preiskave je bilo prepoznavanje biostratigrafskih območij, starosti ter paleookoljskih in paleoklimatskih rekonstrukcij. Iz 609 m dolgega preiskovanega odseka vrtine (1829–2438 m) je bilo uporabljenih 50 vzorcev za preiskave alg luknjičark ter apnenčastih nanofosilov ter 25 vzorcev za palinološke preiskave na intervalih dolžin 12 m in 24 m. Uporabljene so bile standardne laboratorijske tehnike priprave za tri skupine mikrofosilov. Zaradi pojavljanja nekaterih oblik, kot so *Globigerina praebulloides*, *Haplophragmoides spp, Bolivina scalprata miocenica, Valvulina flexilis in Cyclammina cf. minima* sta bili identificirani dve planktonski ter ena bentonska cona alg luknjičark. To sta coni: lower N18, Upper N17 (zgodnji Pliocen, pozni Pliocen) in cona *Cyclammina minima* (pozni Miocen). Za nanofosile sta bili prepoznani dve bioconi, in sicer NN12 (cona *Ceratolithus cristatus*) in NN11 (cona *Discoaster berggrenii*). Omenjeni coni sta bili dodeljeni zgodnjemu Pliocenu ter poznemu Miocenu. Ostale forme vključujejo: *Discoaster pentaradiatus, Sphenolithus* *abies* in *Ceratolithus armatus. Echitricolporites spinosus*/ cona P800 je bila dodeljena sklopom palinomorfa in je bila datirana kot pozni Miocen zaradi kvantitativnega pojavljanja *Cyperaceaepollis spp.* Štiri identificirani glavni zgoščeni odseki vključujejo intervale 1926 m, 1987 m, 2097 m in 2316 m, ki so bili datirani kot 5.0 Ma, 5.8 Ma, 6.3 Ma in 7.0 Ma. Na osnovi bentonske vrste alg luknjičark in palinološkega morskega indeksa, je plitvo morsko območje izbrano za preučevan interval ki je nastal pod mokrimi in suhimi paleoklimatskimi pogoji. Izsledki preiskave lahko brez dvoma služijo kot osnova za zaporedni stratigrafski model, ki v splošnem presega ločljivost seizmične stratigrafije.

Ključne besede: biostratigrafija, paleoklima, paleookolje, palinološki morski indeks

Introduction

The Niger Delta Basin is one of the rift-generated sedimentary basins on the continental margin of the Gulf of Guinea in Nigeria [1]. The study area lies approximately between latitudes 4°23′30″N and 6°24′00″N and longitudes 2°45′30″E and 6°46′30″E (Figure 1). As the Niger delta basin matures, most of its subsurface uncertainties lie at reservoir scale, and hence the need for application of biostratigraphy. Oil companies which invest hugely in this high-risk business of oil exploration have undoubtedly gained much from biostratigraphic studies. Apart from assigning ages to rocks, the prediction of water depths and palaeodepositional environments is vital for the understanding and deduction of depositional models with reasonable productiveness [2]. Previous studies include those on foraminifera biostratigraphy from offshore Western Niger Delta [3]. Fajemila [3] recognized five foraminiferal zones and inferred that the sediments were of normal salinity and belonged to early Pliocene to late Miocene age.

Sanuade [4] carried out calcareous nannofossil biostratigraphy of Well 'K-2', in the deep offshore, Niger Delta. Two major zones were identified, while one condensed section was believed to be associated with 2.0 Ma maximum flooding surface (MFS).

Aturamu [6] reported on integrated biostratigraphic studies using foraminiferal and palynomorph assemblages within the Niger Delta. They established two planktonic foraminiferal zones, *Globigerinoidies obliquus* and *Globigerinoides ruber*, aged Miocene–Pliocene and four benthic foraminiferal biozones. They proposed *Echiperioporities* cf. *estelae*, *Psilatricolpites okeizeis* and *Foeveotricolpites* sp. palynological zones which are correlatable with the Pantropical zones. Ukpabi and Osterloff [7] integrated microflora and nannoflora for biostratigraphic and palaeoenvironmental study of the Niger Delta sediments. They documented the occurrence of *Belskipolliselegans* which revealed the influence of climate, sea-level changes and/or sediment influx in the Niger Delta during the middle Miocene. The transgressive and regressive trends were interpreted and correlated based on the general distribution of *Belskipolliselegans* within the palynological zones in the middle Miocene Agbada Formation of the Niger Delta Basin.

The present study gives an account of integrated foraminiferal, calcareous nannofossils and palynostratigraphy of the STEP-1 well, offshore western Niger delta, in order to deduce the age of the penetrated interval, and provide detailed information on the paleoenvironment of deposition and palaeoclimatic conditions of the sediments. Such information, no doubt, could serve as a sequence stratigraphic model, generally beyond the resolution of seismic stratigraphy.

Geologic setting and stratigraphy

The Niger Delta basin is situated between latitudes 3° and 6°N and longitudes 5° and 8°E in the Gulf of Guinea on the margin of West Africa, and is one of the largest deltaic systems in the world. Doust and Omatsola [8] and Short and Stauble [9] classified the subsurface Niger Delta into three stratigraphic units from the oldest to the youngest: Akata, Agbada and Benin Formations (Figure 2). The Akata Formation is the basal unit of the Tertiary Delta Complex and comprised shales, clays and silts at the base of the known delta sequence. They contain a few

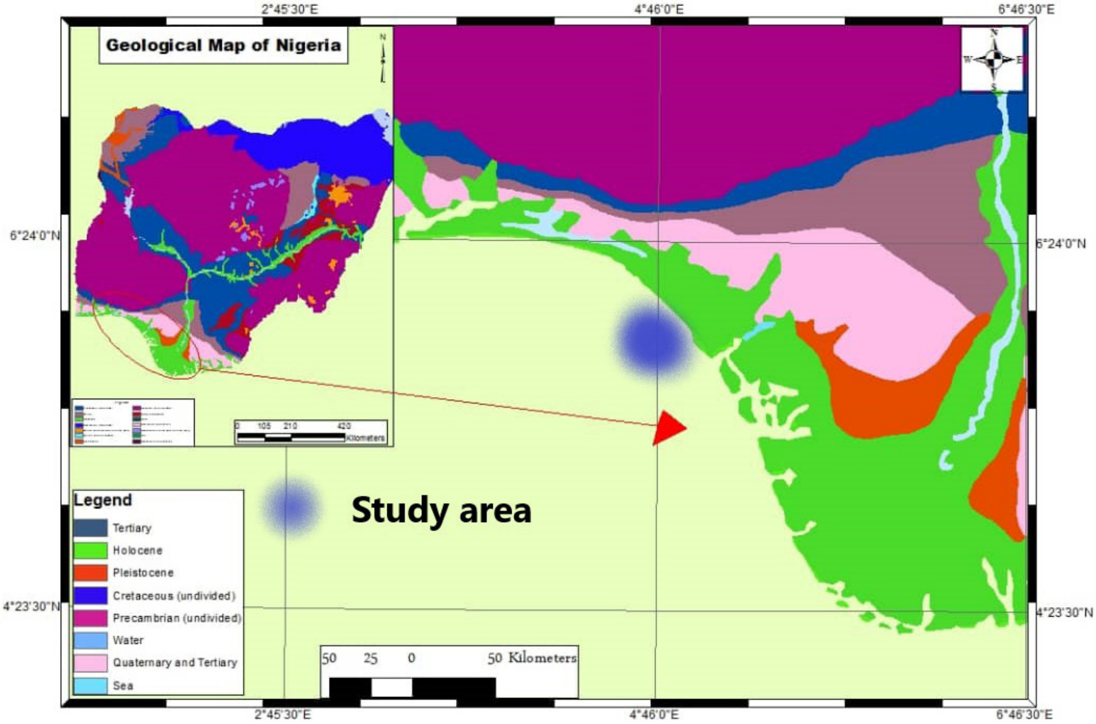

Figure 1: *Geological map of Western Niger Delta showing the approximate study area (modified from [5]).*

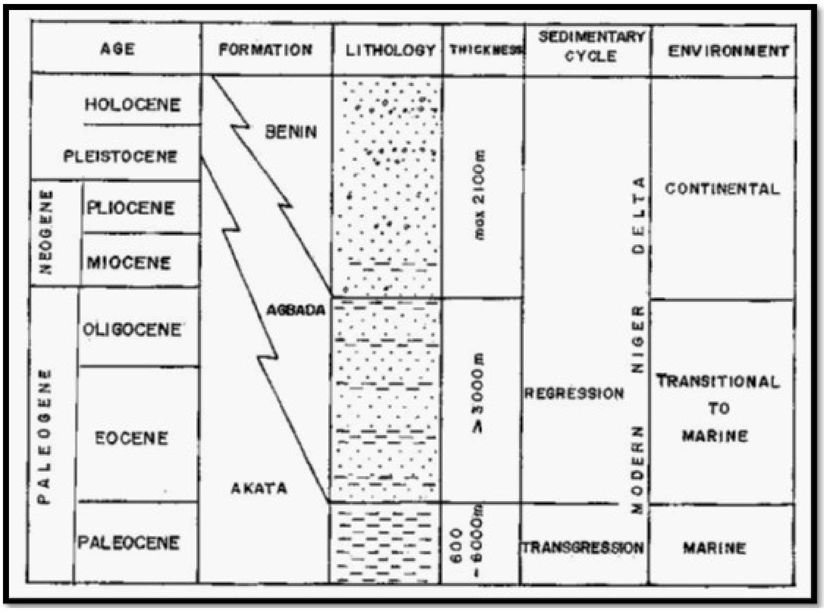

Figure 2: *Stratigraphic succession of the Niger Delta [7].*

streaks of sand, possibly of turbiditic origin [10]. The Agbada Formation is the hydrocarbon-prospective sequence, a paralic clastic sequence which lies above the Akata Formation. The upper part of the Agbada Formation often has sand percentages ranging from 50% to 75%, becoming increasingly sandy towards the overlying Benin Formation, while the basal part is more of shale sequence [8]. The Benin Formation is the freshwater-bearing formation in the Niger Delta. It comprises the top part of the Niger Delta Basin, from the Benin-Onitsha area in the north to beyond the present coastline [9].

Materials and methods

Materials used in this study include ditch cuttings and gamma ray log. Because of the proprietary nature of the well, the exact location information was not provided, hence it was code-named STEP-1 well. The samples were selected and composited at intervals of 12 m and 24 m, respectively, which was then prepared and analysed based on fauna and flora contents. The biostratigraphic analyses were carried out while the other analysis was achieved using the STRATABUG software.

Lithologic description

The lithologic description was carried out by examining the samples under a hand lens in order to identify the constituents, describe and name the lithology. This was supported by the GR log to complement the lithologic description based on its deflection away from the Shale Baseline (SBL).

Sample preparation

The ditch cuttings were prepared for foraminifera, calcareous nannofossils and palynomorph contents using standard preparatory methods. Fifty samples were selected at 12 m intervals for foraminifera preparation; the standard weight (20 g) of each sample was soaked overnight to ensure proper disaggregation and liberation of microfossils present within the cuttings. The disaggregated samples were then washed under a shower of water over a 63 µm sieve, rinsed in liquid detergent to remove drilling mud and dried over a hot plate. The forms were picked with a picking needle under an Olympus binocular microscope. Preparation and identification of individual foraminifera were guided following the works of [11–13], among others.

Fifty samples were selected at 12 m interval for calcareous nannofossils; about 2 g of each of the samples were scraped onto a glass microscope slide. The slides were labelled sequentially and two blobs of Norland Optical Adhesive were affixed onto the cover-slip. The slides were dried and later studied under a transmitting light microscope in polarized light. This was done following Martini [14].

Twenty-five samples were selected and composited at 24 m intervals for palynological analysis. A constant weight (30 g) of each sample was initially given a 5% dilute hydrochloric acid treatment to remove carbonates prior to complete digestion in concentrated hydrofluoric acid (HF) under a fume cupboard. The samples were decanted thrice at an interval of 1 h each through the Branson Sonifier and with the aid of a 5 µm sieve to filter away the inorganic matter. A LOCTITE mounting medium was used for the residues, which are the palynomorphs. Identification and preparation of the specimen was done following Germeraad et al. [15].

Results and discussion

Lithologic description

The lithostratigraphic section of the studied well was produced from ditch sample descriptions and the deflection away from the shale base line on the gamma ray log. The total thickness of the analysed sample is 609.6 m (i.e. between 1,828.8 m and 2,438.4 m intervals). From the lithologic description, the samples are mainly shale with a little sand. The shale is fissile, greyish to black, while the sand is fine to medium grained. The observation revealed that the studied well is largely made up of a sequence of fine-grained shale alternating with fine- to medium-grained sandstone in the lower part while the upper part is mainly shale (Figure 3).

Foraminifera biostratigraphy

The well recorded fairly rich and diverse assemblages of planktonic and benthonic foraminifera at the upper part (1,902–2,109 m), with 55 species recorded. Of these, 22 (40%) species are calcareous, while 27 (49%) are arenaceous. Two foraminiferal “zones” were recognized in the studied section. The Cenozoic chronostratigraphic scheme of Berggreni et al. [13] and the Global Sequence Cycle Chart of Hardenbol et al. [16] were adopted for this study. The zones are characterized briefly below.\

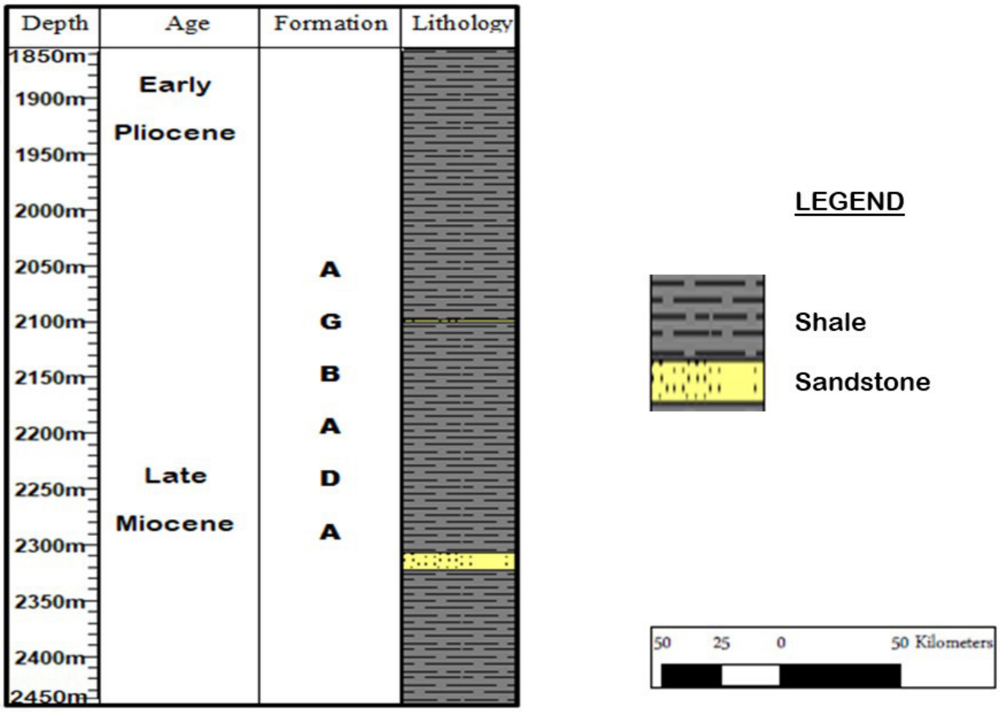

Figure 3: *Lithological description of STEP-1 well.*

1. *Globorotalia tumida/Cyclammina minima zone*
   Stratigraphic interval: 1,841–1,987 m
   Equivalent planktic foraminiferal zone: “Lower” N18–“Upper” N17 zone.
   Age: Late Miocene (5.99–5.47 Ma)
   Diagnosis: The top of this zone is placed at the 5.47 Ma MFS, recognized at 1,926 m, while the base is defined by the 5.8 Ma MFS, recognized at 1,987 m (Figure 4). The First Downhole Occurrence (FDO) of the zonal marker, *Cyclammina cf. minima* was recorded at 1,926 m (Table 1). The zone correlates with the “Lower” N18–“Upper” N17 planktic foraminiferal zone of Berggreni et al.[13] and Hardenbol et al. [16]. The age is late Miocene.

2. *Globoquadrina dehiscens/Haplophragmoides narivaensis zone*
   Stratigraphic interval: 1,987–2,438 m.
   Equivalent planktic foraminiferal zone: “Middle-Lower” N17 zone.
   Age: Late Miocene
   Diagnosis: Undiagnosed

Calcareous nannofossil biostratigraphy

The results of calcareous nannofossil analysis show high abundance and diversity of species (Figure 5). Biozonation and age determination of the well was based largely on calcareous nannofossils assemblages, abundance and diversity. The chronostratigraphic scheme adopted follows the usage of the worldwide zonation schemes of Okada and Bukry [17] and Haq et al. [18]. Considerable effort was made to identify and define zonal tops with the FDOs of diagnostic marker species, abundance and species diversity peak as these form the most reliable events [14]. The highest nannofossil peaks were dated using important marker species such as *Sphenolithus abies, Discoaster pentaradiatus, Ceratolithus cristatus, Ceratolithus armatus, Discoaster quinqueramus* and *Discoaster berggrenni* (Table 2). The stratigraphic distribution of the recorded species along with the significant datum, MFSs, nannofossil zones and age interpretations are presented in distribution charts (Figure 5). The highlights of the results are summarized below.

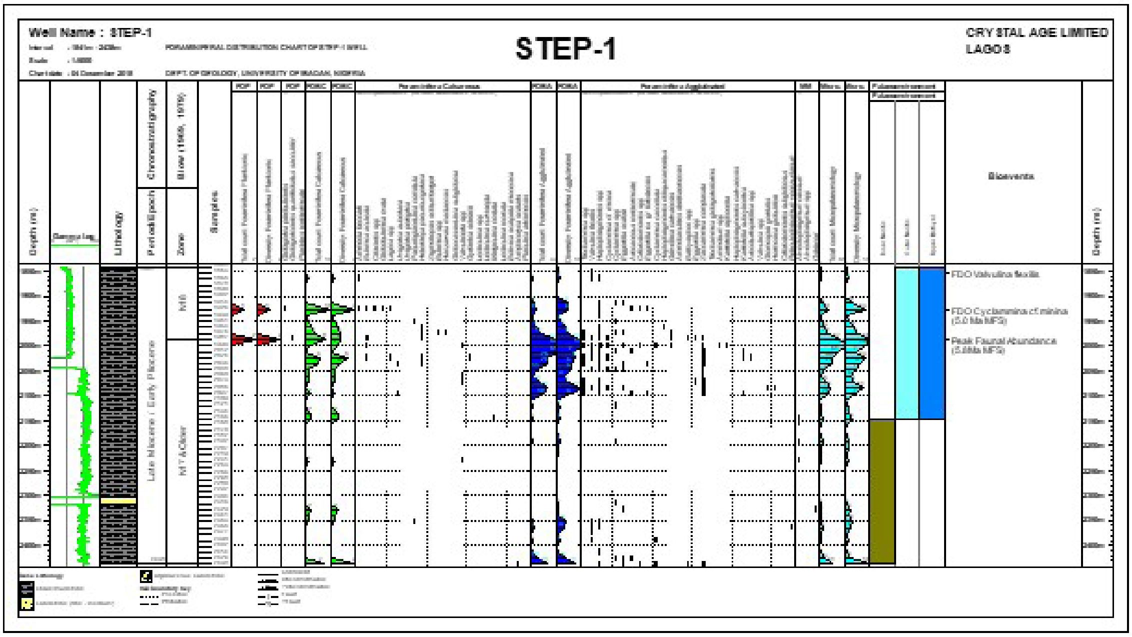

Figure 4: *Foraminiferal distribution chart of STEP-1 well.*

Table 1: *Foraminferal biostatigraphy of STEP-1 well*

Depth (m)	Age	Planktonic zone	Benthonic foram zone	Bioevents
1,853	Early Pliocene	N18	Indeterminate	FDO *Valvulina flexilis*
1,926				Cyclamina cf. minima 5.0 Ma MFS
1,987	Late Pliocene	N17 and older	*Cyclamina cf. minina*	Peak fauna abundance 5.8Ma MFS
2,097				
2,438			Indeterminate	

1. Interval: 1,841–1,926 m
   Zone: NN12
   Age: Early Pliocene
   Diagnosis: This interval is dated based on the presence of *Ceratolithus cristatus* at 1,902 m and the presence of *Ceratolithus armatus* at 1,914 m. These records of nannofossils represent the early Pliocene.
2. Interval: 1,926–2,438 m
   Zone: NN11
   Age: Late Miocene
   Diagnosis: This interval is characterized by an increase in nannofossil abundance and diversity. Its nannofossil peak at 1,963 m represents the 5.8 Ma MFS [18] late Miocene NN11 zone. This is confirmed by the FDO of *Discoster quinqueramus* at 1,939 m. The presence of *Discoaster berggrenii* at 2,292 m further confirmed the 7.0 Ma MFS [18] age assigned to the lower section.

Palynostratigraphy

Twenty-five palynomorphs were selected at 24 m intervals. The palynomorphs are well preserved and fairly diverse (Figure 6). These include *Zonocostites ramonae*, *Monoporites annulatus, Sapotaceae, Retitricolporites irregularis, Pachydemites diederixi, Acrostichum aureum, Pteris spp, Laevigatosporites spp, Verucatosporites spp, Stereisporites spp, Cyperaceaepollis spp, Sapotaceae* and *Psilatricolporites crassus.* Dinoflagellate cysts recorded are *Selenopemphix spp*, *Polysphaeridium zoharyi* and *Leiosphaeridia spp.*

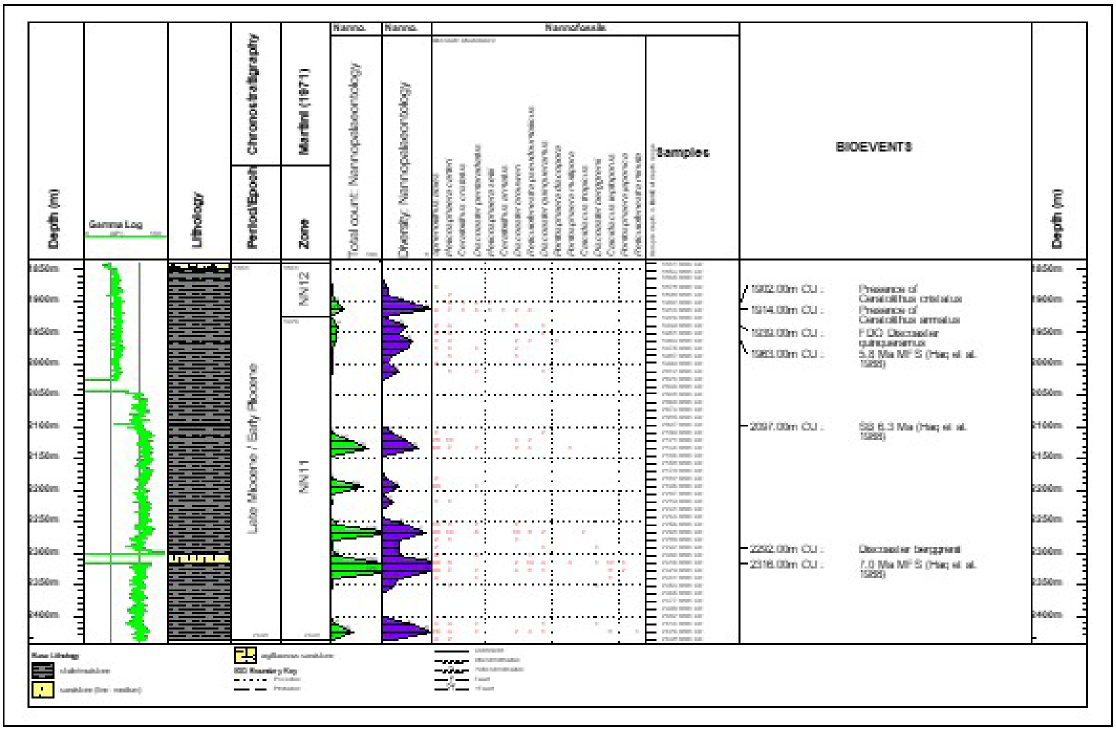

Figure 5: *Calcareous nannofossil distribution chart of STEP-1 well.*

Table 2: *Calcareous nannofossils biostratigraphy of STEP-1 well*

Depth (m)	Downhole occurrence of calcareous nannofossils	Age (Ma) Haq et al. (1988)	NP zones (Martini, 1971)	Inferred relative ages
1,841	First sample analysed			Late Miocene to early Pliocene
1,902	Presence of *Ceratolithus cristatus*		NN 12	
1,914	Presence of *Ceratolithus cristatus*			
1,926				
1,939	FDO: *Discoaster quinqueramus*	5.8	NN 11	
1,963	Maximum flooding surface			
2,292	FDO: *Discoaster berggrenii*			
2,316	Maximum flooding surface, Presence: Discoaster quinqueramus	7.0		
2,438 TD				

The STEP-1 sediments are assigned to the section within the Pantropical *Echitricolporites spinosus* zone of Germeraad et al. [15] and the P800 zone of Evamy et al. [1]. The zone was further subdivided into P840 and P830 sub-zones. Details of the zone and sub-zone identified are represented in Tables 3 and 4, and explained briefly below.

1. Zone: P800
   Sub-zone: P840
   Interval: 1,829–2,204 m
   Discussion: The top of this sub-zone is placed at 1,829 m of the first sample analysed. The base is defined by the quantitative occurrence of *Cyperaceaepollis spp* at 2,204 m. The P840 sub-zone is further confirmed and characterized by the presence of *Stereisporites*

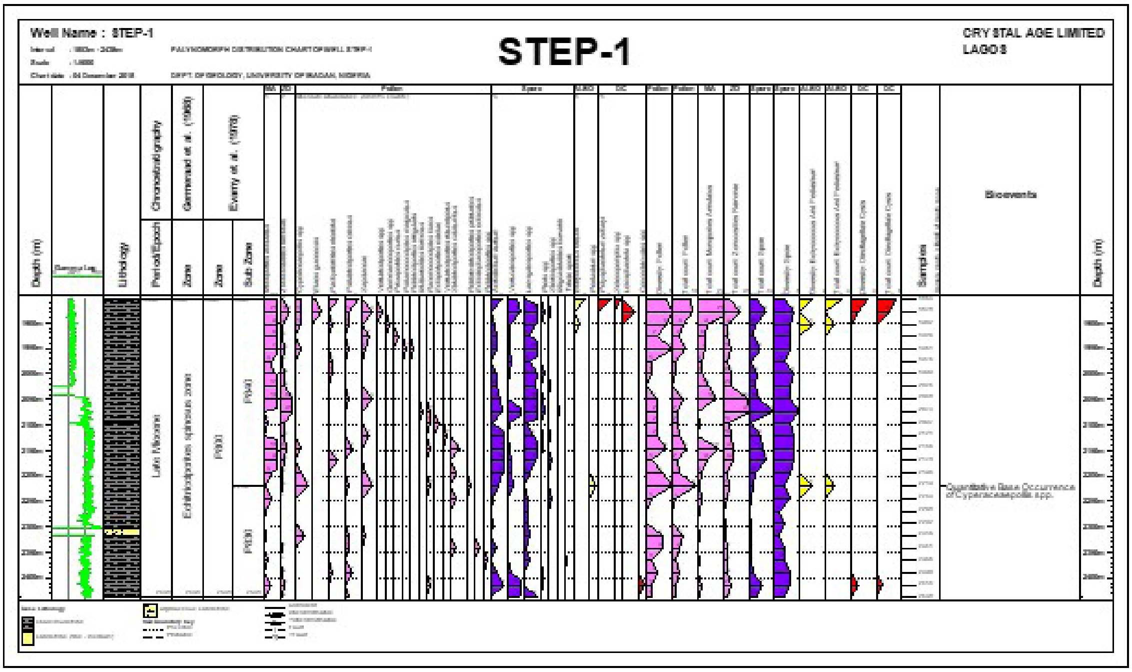

Figure 6: *Palynomorphs distribution chart of STEP-1 well.*

Table 3: *Palynostratigraphy of STEP-1 well*

Depth (m)	series	Sub-series	Gemeraad et al. (1968)	Evamy et al. (1978)		Bioevents
				Zone	Sub-zone	
1,829	Miocene	Late Miocene	*Echitricolporites Spinosus* zone	P 800	P 840	Quantitative base occurrence of *Cyperaceaepollis spp*
1,981						
2,134					P 830	
2,204						
2,286						
2,438						

spp, abundant mangrove pollen *Zonocostites ramonae* and *Monoporites annulatus.* The age assigned to this sub-zone is late Miocene.

2. Zone: P800
   Sub-zone: P830
   Interval: 2,204–2,438 m
   Discussion: The top of this sub-zone is placed at 2,204 m defined by the quantitative base occurrence of *Cyperaceaepollis spp* while the base was not penetrated. This sub-zone is further characterized by the presence of *Cyperaceaepollis spp, Stereisporites spp and Racemonocolpites hians.* The age of this sub-zone is late Miocene.

Age deductions

The ages for this well were established using three bioevents (Table 5): these include recorded peak faunal abundance (MFS), sequence boundary (SB) and the occurrence of some index fossils such as *Cyclammina cf. minima* and *Discoaster beggrenii.* The chronostratigraphic position of STEP-1 well is given in Table 6.

Palaeoenviroment of deposition

1. The presence of some benthonic foraminifera such as *Uvigerina auberiana, Lenticulina spp, Valvulineria spp, Haplophragmoides spp, Cyclamina cf. inina and Bolivina scalprata*

indicates a shallow marine environment (inner neritic).

2. With land-derived palynomorphs such as *Monoporites annulatus, Laevigatosporites spp, Zonocostites ramonae*, *Acrostichum aureum, Pachydemites diederixi, Pteris spp, Striatricolpites catatumbus* and *Cyperaceaepollis spp* (from 1,853–2,438 m). It can be deduced that the sediments were deposited within a shallow marine environment.

Table 4: *Harmonized biostratigraphic chart of STEP-1 well*

Depth (m)	Epoch	Age	P zone	B zone	N zone	Pa zone	Pa zone and sub-zone	Bioevents
1,900	Early Pliocene	ZANCLEAN	N18		NN 12		P840	FDO *Valvulina flexilis*
1,950								Presence of *Ceratolithus cristatus*
2,000								Presence of *Ceratolithus armatus*
2,050								FDO *Cyclammina cf. minima* (5.0Ma MFS)
2,100								FDO *Discoaster quinqueramus*
2,150	Late Miocene	MESSIAN	N 17 and older	*Cyclamina minima*	NN 11	*Echitricolporites Spinosus*	P800 P830	5.8 Ma MFS
2,200								Peak faunal abundance (5.8 Ma MFS)
2,250								6.3 Ma SB
2,300								Quantitative base occurrence of *Cyperaceaepollis spp*
2,350								*Discoaster beggrenii*
2,400								7.0 Ma MFS

Palaeoclimatic deductions

Palynofossils are preserved mainly in continental basins. The characteristics of great quantity, wide distribution and different preserved lithofacies are the unique advantage of these fossils [19]. For this reason, palynomorphs are now very important for reconstructing palaeoclimatic conditions at the time of sediments deposition. The climate of an area is reflected by its vegetation type [20]. The three important palynomorphs used for this study are *Monoporites annulatus*, *Zonocostites ramonae* and *Acrostichum aureum*. Monoporites annulatus abundance is often used as an indicator of a large degree of landscape openness [21, 22], and increased aridity [23, 24]. *Zonocostites ramonae* has been used as an indicator for mangrove vegetation and hence, wet climatic condition [25]. *Acrostichum aureum* is used as an indicator of wet climatic condition [26].

From Figure 7, the dominance in abundance of *Monoporites annulatus* over the relative abundance of *Acrostichum aureum* favours a dry climatic condition for the interval 1,853–2,048 m. While the sediments are believed to have been deposited in the Savanna setting, interval 2,073–2,146 shows alternating wet and dry climate.

From Figure 8, the dominance in abundance of *Acrostichum aureum* over *Monoporites annulatus* from interval 2,170–2,438 m indicates a wet climatic condition; hence, they are of mangrove species, although interval 2,243–2,265 m relatively shows alternating wet and dry climatic conditions. Figure 9 shows photomicrographs of foraminifera, calcareous nannofossil and Palynomorps recovered from the STEP-1 well.

Table 5: *Age deductions for STEP-1 well*

Depth (m)	Age (Ma)	Microfossil	Bioevents
1,926	5.0	Foraminifera	FDO *Cyclammina cf. minima*
1,963	5.8	Nannofossils	Maximum flooding surface (MFS)
1,987	5.8	Foraminifera	Peak faunal abundance (MFS)
2,097	6.3	Nannofossils	Sequence boundary
2,316	7.0	Nannofossils	MFS

Table 6: *Chronostratigraphic position of STEP-1 well*

	Standard chronostratigraphy			
Ma	**Period**	**Epoch**	**Age/stage**	**This study**
1	Quaternary	Holocene	Taranian	
2		Pleistocene	Ionian	
			Calabrian	
3				
	Neogene	Pliocene	Gelasian	
4			Piacenzian	
5			Zanclean	STEP-1 well
6		Miocene	Messinian	
7				
8				
			Tortonian	
9				
10				

Summary and conclusions

Foraminifera, calcareous nannofossils and palynomorph integrated biostratigraphic studies of the STEP-1 well in the offshore of Niger Delta Basin has resulted in the identification of biostratigraphic zones, determination of ages as well as reconstruction of the palaeoenvironment and palaeoclimatic conditions. The presence of some benthonic foraminifera such as *Uvigerina auberiana, Lenticulina spp, Valvulineria spp, Haplophragmoides spp, Cyclamina cf. inina and Bolivina scalprata* indicates a shallow marine environment of deposition (inner neritic). Two nannofossil zones subdivided into late Miocene and early Pliocene are confirmed by the FDO of *Discoster quinqueramus* at 1,939 m. The presence of *Discoaster berggrenni* at 2,292 m further confirmed the 7.0Ma MFS age assigned to the interval. The late Miocene age also corroborates with the appearance of the zonal marker, *Cyclammina cf. minima,* which was recorded at 1,914 m. The Palynological Zonation of the well and their stratigraphic distribution based on the zonation schemes of Germeraad et al. [15] and Evamy et al. [1] are broadly assigned to the *Echitricolporites spinosus* and P800 zone, respectively. The latter was further subdivided into P840 and P830 sub-zones. The assigned age is late–late Miocene. The boundary between P830 and P840 was at 2,204 m, which was marked by the Quantitative base

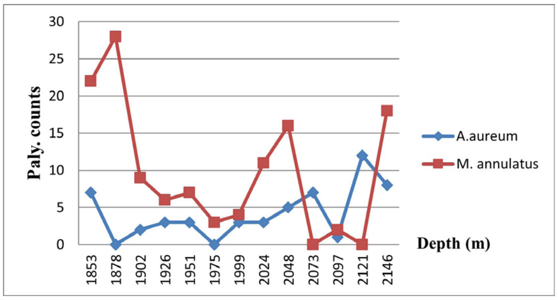

Figure 7: *Plot of A. aureum/M. annulatus against depth (1,853–2,146 m).*

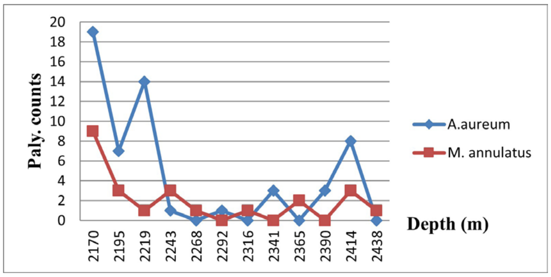

Figure 8: *Plot of A. aureum/M. annulatus against depth (2,170–2,438 m).*

occurrence of *Cyperaceaepollis spp*. The four major condensed sections identified within the studied section of the well which include intervals at 1,926, 1,987, 2,097 and 2,316 m have been dated 5.0, 5.8, 6.3 and 7.0 Ma, respectively, based on the identified foraminiferal and calcareous nannofossil zones with their equivalent bioevents. This study reveals that the well penetrated a major sedimentary formation in the Niger Delta, which conforms to the paralic

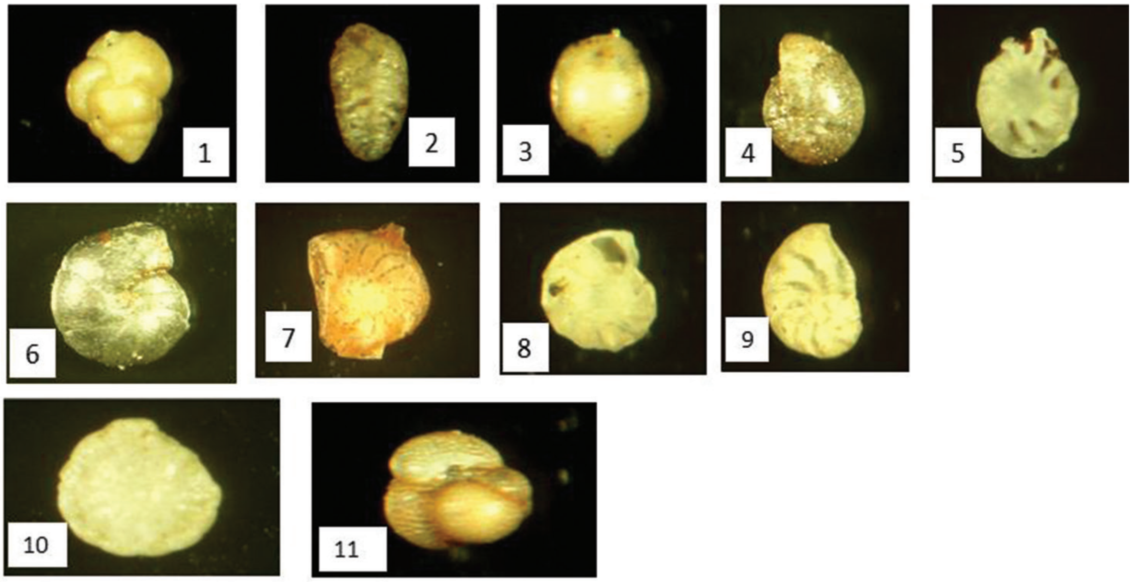

1. *Uvigerina peregrina*
2. *Bolivina scalptrata miocenica*
3. *Lagena sp.*
4. *Cyclammina cancellata*
5. *Lenticulina sp.*
6. *Cibicides sp*
7. *Planulina arinimensis*
8. *Lenticulina inornata*
9. *Valvulineria spp.*
10. *Cyclammina cf. minima*
11. *Globigerina praebulloides*

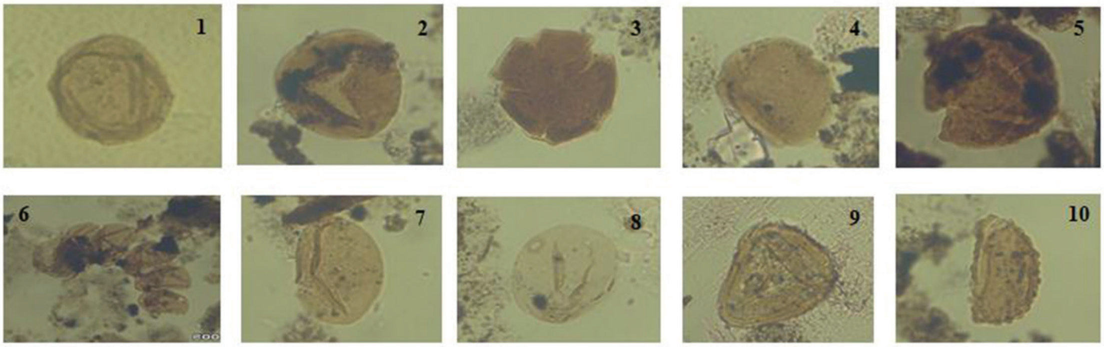

(1) *Leiosphaeridia sp* (2) *Acrostichum aureum* (3) *Pachydermites diederixi*

(4&5) *Psilatricolporites crassus* (6) *Microforaminiferal wall linings* (7) *Laevigatosporites sp*

(8) *Monoporites annulatus* (9) *Pteris sp* (10) *Verrucatosporites sp*

Figure 9: *Continued*

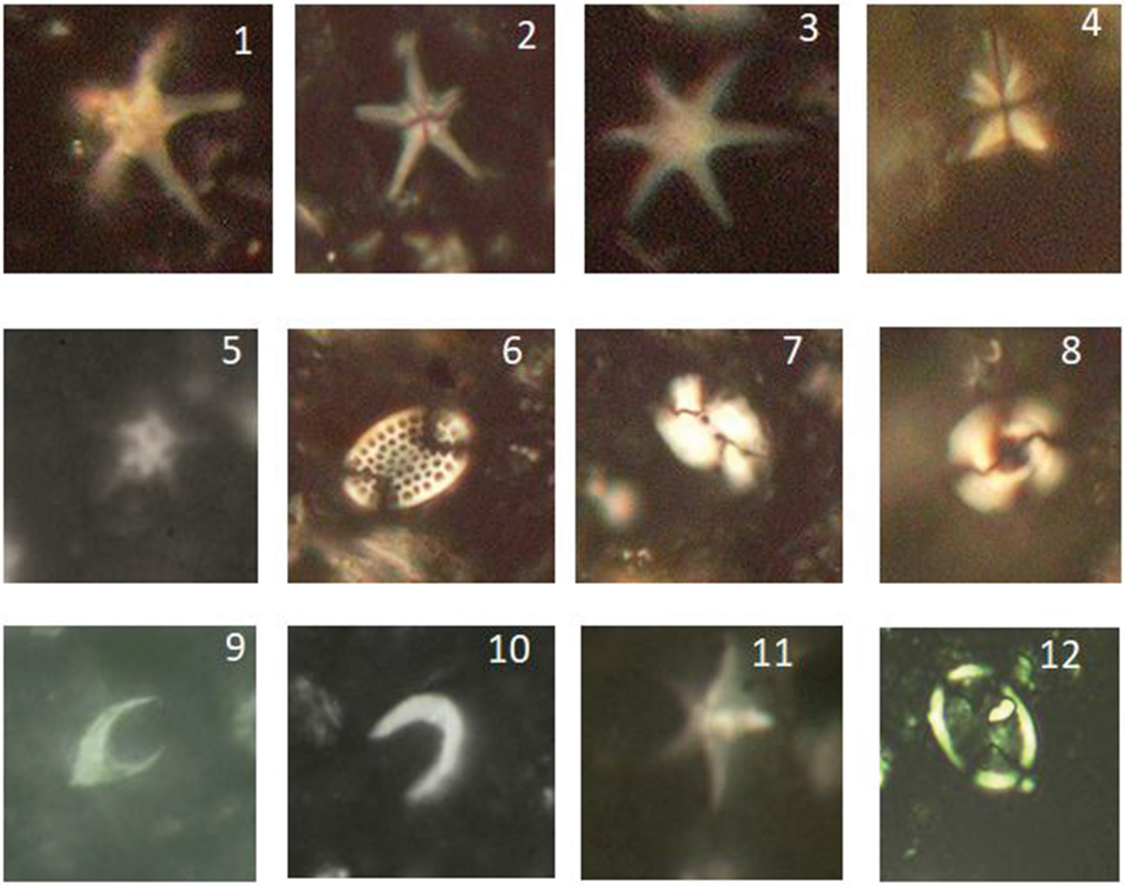

(1) *Discoaster quinqueramus* (2) *Discoaster pentaradiatus* (3) *Discoaster brouweri*
(4) *Sphenolithus abies* (5) *Discoaster berggrenii* (6) *Pontosphaera multipora*
(7) *Helicosphaera carteri* (8) *Reticulofenestra pseudoumbilicus* (9) *Ceratolithus armatus* (10) *Ceratolithus cristatus* (11) *Discoaster quinqueramus* (12) *Pontosphaera japonica*

Figure 9: *Photomicrographs of foraminifera, calcareous nannofossil and Palynomorps recovered from STEP-1 well.*

sequence of Agbada Formation. The palynoflora *Monoporites annulatus, Laevigatosporites sp.* among others suggests a shallow marine environment of deposition, while the palaeoclimatic setting indicated both wet (1,853–2,146 m) and dry (2,170–2,438 m) conditions. The integration of the three microfossil groups for biostratigraphic studies has produced a detailed analysis in the recognition and interpretation of absolute biosignals.

Acknowledgements

The authors appreciate the efforts of Mrs Adebiyi E. Abidemi from Mosunmolu Ltd. for her support and the staff of Crystal Age Ltd, Lagos.

References

[1] Evamy, B.D., Harremboure, J., Kamerling, P., Knaap, W.A., Molloy, F.A., Rowlands, P.H. (1978): Hydrocarbon habitat of the Tertiary Niger Delta. *American Association of Petroleum Geologists Bulletin*, 62, pp. 277–298.

[2] Singh, A. (2008): Micropaleontology in petroleum exploration, *Seventh International Conference and Exposition on Petroleum Geophysics Bulletin*, pp. 288–294.

[3] Fajemila, O.T. (2012): Foraminifera biostratigraphy and paleoenvironmental studies of two wells from offshore western Niger delta. *Ife Journal of Science*, 14(2), pp. 369–384.

[4] Sanuade, O.A. (2014): Calcareous nannofossil biostratigraphic analysis of well 'K-2', deep offshore Niger Delta, Nigeria. *Advances in Research*, 2(12), pp. 696–711.

[5] Obaje, N.G. (2009): Geology and mineral resources of Nigeria, lecture notes in earth sciences 120. *Journal of Geoscience and Environment Protection*, DOI: 10.1007/978-3-540-92685-6.

[6] Aturamu, A.O., Ojo, A.O. (2015): Integrated biostratigraphic analysis of the Agbada Formation [Nep-1 Well] offshore, Eastern Niger-Delta Basin, Nigeria, *Australian Journal of Biology and Environment Research*, 2(1), pp. 1–14.

[7] Ukpabi, N., Osterloff, P.L., Oloto, I.N. (2014): Biostratigraphy studies of Miocene sediments in the onshore/offshore area, Niger Delta Basin, Nigeria. *International Journal of Science Inventions Today*, 3(4), pp. 330–345.

[8] Doust, H., Omatsola, E. (1990): Niger Delta. In: *Divergent/passive Margin Basins, American Association of Petroleum Geologists Memoir* 48, Edwards, J.D., Santogrossi, P.A., (eds.), American Association of Petroleum Geologists: Tulsa, pp. 239–248.

[9] Short, K.C., Stauble, A.J. (1967): Outline of the geology of Niger Delta. *American Association of Petroleum Geologists* Bulletin, 51, pp. 761–779.

[10] Avbovbo, A.A. (1978): Tertiary lithostratigraphy of Niger Delta. *American Association of Petroleum Geologists Bulletin*, 62, pp. 295–300.

[11] Blow, W.H. (1969): Late middle Eocene to recent planktonic foraminiferal biostratigraphy. In: *Proceedings of the First International Conference on Planktonic Microfossils*, Genova, Brönnimann, P., Renz, H.H. (eds.). E.J. Brill, pp. 199–442.

[12] Loeblich, A.R. Jr., Tappan, H. (1988): *Foraminifera genera and their classification,* Vol. 2. Van Nostrand Reinhold Company: New York, pp. 970.

[13] Berggreni, W.A., Kent, D.V., Swisher, C.C., Aubry, M. (1998): *A revised Cenozoic geochronology and chronostratigraphy*. DOI:10.2110/pec.95.04.0129

[14] Martini, E. (1971): Standard Tertiary and Quaternary Calcareous Nannoplankton Zonation. In: *Proceedings II Planktic Conference*, Rome*,* Farinacci, A. (ed.). 1970. 2, pp. 739–785.

[15] Germeraad, J.H., Hopping, C.A., Muller, J. (1968): Palynology of tertiary sediments from tropical areas. *Review of Palaeobotany and Palynology*, 6, pp. 189–346.

[16] Hardenbol, J., Thierry, J., Farley, M.B., Jacquin, T., de Gracuabsjt, P., Vail, P.R. (1998): Mesozoic and Cenozoic sequence chronostratigraphic framework of European basins. In: *Mesozoic and Cenozoic sequence stratigraphy of European basins*, De Graciansky, P.C., Hardenbol, J., Jacquin, Th., Vail, P.R. (eds.). *SEPM Special Publication 60.*

[17] Okada, H., Bukry, D. (1980): Supplementary modification and introduction of code numbers to the low-latitude coccolith biostratigraphic zonation [Bukry, 1973, 1975]. *Marine Micropaleontology*, 5, pp. 321–325, DOI: 10.1016/0377-8398[80]90016-X.

[18] Haq, B.V.J., Hardenbol, J., Vail, P.R. (1988): Mesozoic and Cenozoic chronostratigraphy and eustatic cycles. In: *Sea level change – an integrated approach,* Wilgus et al. (eds.), SEPM Special Publication, No. 42, pp. 71–108.

[19] Zhao, J., Wan, X.Q., Xi, D.P., Jing, X., Li, W., Huang, Q.H., *et al*. (2014): Late cretaceous palynology and paleoclimate change: Evidence from the SK1 [South] core, Songliao Basin, NE China. *Science China Earth Sciences*, 57(12), pp. 2985–2997, DOI: 10.1007/s11430-014-4975-4.

[20] Samant, B., Phadtare N.R. (1997). Stratigraphic palynoflora of the Early Eocene Rajpardi lignite, Gujarat and the lower age limit of the Tarkeshwar Formation of South Cambay Basin, India. *Palaeontographica*, B, 245, pp. 1–108.

[21] Joly C, Barille L, Barreau M, Mancheron A, Visset L. (2007): Grain and annulus diameter as criteria for distinguishing pollen grains of cereals from wild grasses. *Review of Palaeobotany and Palynology*, 146, pp. 221-233.

[22] Schüler, L., Behling H. (2011): Poaceae pollen grain size as a tool to assess palaeoecological grassland dynamics in South America. *Veget Hist Archaeobot*, 20, pp. 83–96.

[23] Salgado-Labouriau M.L., Rinaldi M., (1990): Measurements of gramineae pollen of the Venezuelan mountains. *Revista Brasileira de Biologia*, 50, pp. 115–122.

[24] Behre K.E. (1981): The interpretation of anthropogenic indicators in pollen diagrams. *Pollen Spores*, 23, pp. 225–245.

[25] Massini García, J.L., Jacobs, B.F., Pan, A., Tabor, N., Kappelman, J. (2006): The occurrence of the fern Acrostichum in Oligocene volcanic strata of the

Northwestern Ethiopian Plateau. *International Journal of Plant Science*, 167(4), pp. 909–918.

[26] Morley, R.J. (1995): Biostratigraphy characterization of systems tracts in tertiary sedimentary basins. *Proceedings of the International Symposium on Sequence Stratigraphy*, Jakarta, S.E. Asia, 1, pp. 49–71.

Original scientific article

Received: Oct 14, 2020
Accepted: Jan 14, 2021
DOI: 10.2478/rmzmag-2020-0015

Fractional Current Flow in the Subsurface Using Electrical Resistivity Method: A Laboratory Approach

Podpovršinsko gibanje električnega toka z uporabo električne uporovne metode: laboratorijski pristop

James Adeyemo Adegoke[1], Gideon Oluyinka Layade[2,*], Temitayo Kadir[1]
[1]Department of Physics, University of Ibadan, Ibadan, Nigeria
[2]Department of Physics, Federal University of Agriculture, Abeokuta, Nigeria
*layadeoluyinka018@gmail.com

Abstract

The authors describe electrical resistivity method using a laboratory experiment, which was conducted in order to calculate the percentage of current that penetrated each layer of soil arranged in a container using Schlumberger array. Four soil samples arranged in three different set-ups were used. The apparent resistivity obtained was interpreted using curve matching techniques and WinResist iteration yielding types A curve, H curve and A curve, respectively. The interpreted data gave the resistivity of each layer and its thicknesses. The thicknesses obtained from the interpretation were at variance with the actual thicknesses arranged in the container. A multiplier was obtained which serves as a constant in other to obtain the actual thickness. The effective penetration depth of current was determined through the calculated thickness of each layer and the known electrode spacing (AB). The percentage of current that penetrates the layers was found to depend on the electrode spacing as well as the thickness of that layer. Thus, a layer with relatively small thickness has a small percentage of current passing through it compared to a thicker layer.

Key words: resistivity, depth, curve, soil, current.

Povzetek

Raziskava prikazuje električno uporovno metodo z laboratorijskim eksperimentom, ki je bil izveden z namenom izračuna odstotka električnega toka, ki se je gibal preko posamezne plasti zemljine v posodi, z uporabo Schlumbergerjeve postavitve elektrod. Uporabljeni so bili štirje različni vzorci zemljine s tremi postavitvami. Pridobljena navidezna upornost je bila interpretirana z uporabo tehnike ujemanja krivulj ter WinResist iteracijskih tipov krivulj A, H in A. Iz interpretacije podatkov so razvidne upornosti posamezne plasti in njena debelina. Pridobljeni rezultati debelin posameznih plasti niso bile skladne z dejanskimi debelinami. Za izračun dejanske debeline je bil zato pridobljen in uporabljen korekcijski faktor, ki služi kot konstanta. Efektivna globina prodiranja električnega toka je bila določena preko izračunane debeline posamezne plasti in znane razdalje med elektrodama (AB). Odstotek električnega toka, ki prodira preko plasti, je bil odvisen od razmika med elektrodama ter debelino plasti. Tako ima plast zemljine z razmeroma majhno debelino v primerjavi z večjo debelino majhen odstotek toka, ki prehaja skoznjo.

Ključne besede: upornost, globina, krivulja, zemljina, električni tok.

Introduction

The electrical resistivity method is a geophysical prospecting method in which electrical current is transmitted through copper electrodes to the ground for the determination of the electrical properties of subsurface [1–3]. Two types of electrodes are involved in the resistivity surveying method and they are current and potential electrodes. A pair of current electrode is used to transfer current into the ground, while the same pair of potential electrode is employed to measure the potential drop [4]. In other words, the resistivity meter calculates the current flow resistance. The distribution of resistivity of the volume of sounding soil is determined by the electrical resistivity surveys. The possible patterns of differences in result provide information on the form of heterogeneities in the subsurface and their corresponding electrical properties [5, 6].

Resistivity measurements are also based on rock composition, interstitial fluids, temperature and pore geometry. Such parameters influence the electrical resistivity of the soil, but in various ways and in varying degrees [7–9]. Electrical geophysical methods allow soil electrical properties to be measured non-destructively, cost-effectively and quickly [10, 11]. Over the years, engineering studies and groundwater exploration are on the increase as a result of geophysical survey. This is made possible due to the swift advances in software development and associated numerical modelling solutions which have shown the way to the development of the present day technology [12–14].

Studies have shown that vertical electrical sounding (VES) and electrical profiling are the two ways by which electrical resistivity survey can be conducted [6, 15, 16]. VES is applicable for the study of horizontal and near-horizontal interfaces. The procedures involve positioning of both the current and potential electrodes at the same relative spacing. The range is gradually expanded around a fixed central point while electrical profiling is used to assess lateral resistivity variations. The current and potential electrodes are retained and gradually moved along a profile at a fixed distance [6, 17, 18]. This research is aimed at determining the relationship that exists between electrode separation and the percentage of current passing at a particular depth based on the arrangement of layers.

Theoretical background

Resistivity varies with conductivity inversely. A high-conductivity surface therefore has low resistivity and vice versa. The relationship between resistivity (ρ) and conductivity (σ) is presented as Equation (1);

$$\rho = 1 / \sigma \tag{1}$$

The principle of electrical resistivity is based on Ohms' law which state that "the current flowing through a metallic conductor is proportional to the potential difference across its end provided other conditions are kept constant".

Mathematically, it is defined as V = IR

Where V is the Voltage in volts, I is the current in Amps and R is the resistance in Ohms.

The current density (J) and the Electric filed (E) are related through Ohms' law by Equation (2) where E is in volts per meter and σ is the conductivity of the medium in Siemens per meter (S/m)

$$J = \sigma E \tag{2}$$

The Electric field is the gradient of the scalar potential

$$E = -\nabla V \tag{3}$$

Thus we have

$$J = -\sigma \nabla V \tag{4}$$

Taking the gradient of both side

$$\nabla . J = -\nabla . \left(\sigma \nabla V \right) \tag{5}$$

But $\Delta . J = 0$

$$\nabla . \left(\sigma \nabla V \right) = 0 \tag{6}$$

$$\nabla \sigma . \nabla V + \sigma \nabla^2 V = 0$$

The Equation (6) becomes Laplace if σ in the first term is constant and disappear, that is, the potential is harmonic which is stated as follows:

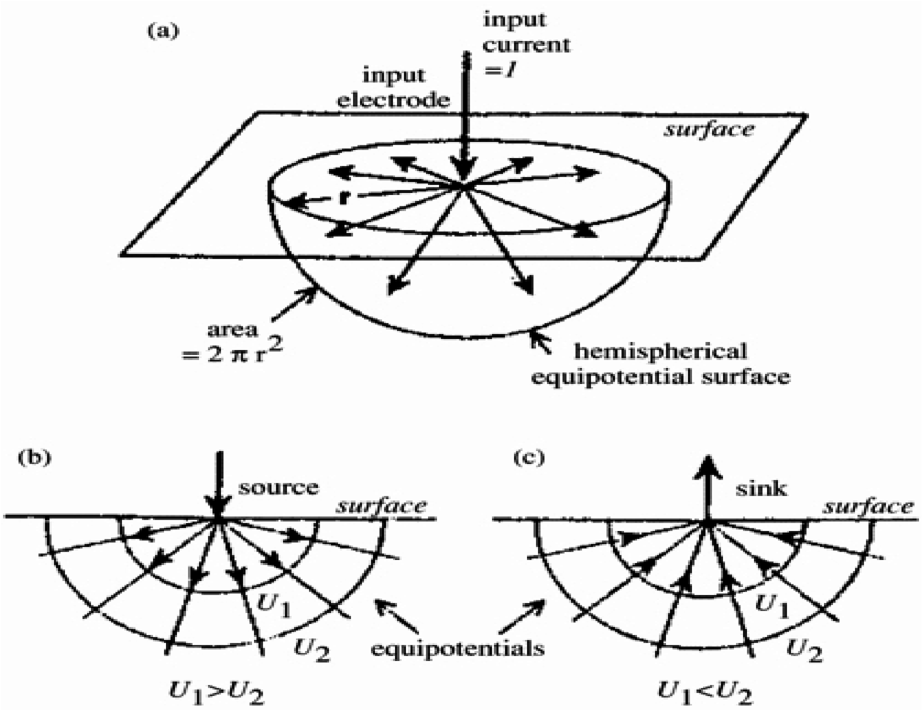

Figure 1: *Electric field lines and equipotential surfaces on the surface of a uniform half-space around a single electrode:* **(A)** *hemispheric equipotential surfaces,* **(B)** *radially outward field lines around a source, and* **(C)** *radially inward field lines around a sink [19].*

$$\nabla^2 V = 0 \tag{7}$$

The potential of a single electrode

The current (I) is injected into a homogeneous half-space, with a specific electrical conductivity (σ) and resistivity (ρ). The current passes under the surface in all directions, but does not flow through the surface. The electric field lines are parallel to the current flow and normal to the hemisphere-shaped equipotential surfaces. Hence, the current density J as a function of radius r is written as

$$J = \frac{I}{2\pi r^2} \tag{8}$$

But $E = \rho J$

Therefore, $$E = \frac{\rho J}{2\pi r^2} \tag{9}$$

Now, $$E = -\nabla V = -\frac{\partial V}{\partial r} = -\frac{\rho J}{2\pi r^2} \tag{10}$$

Integrating Equation (10), the equation for the potential can be stated as follows

$$V = \frac{\rho J}{2\pi r}$$

for a point source at the surface of the half-space.

The four-electrode method

Among the existing geophysical techniques, the resistivity method is generally and mostly used for shallow subsurface studies and groundwater exploration [20]. Four electrodes are used in this method to measure resistivity [21]. One pair of electrodes is used to penetrate the current into the ground and another pair is used to measure the potential difference of hemispheric equipotential surfaces where the ground surface is intersecting them [22]. This is the conventional way in which resistivity is measured in uniform half space [23]. Figure 2

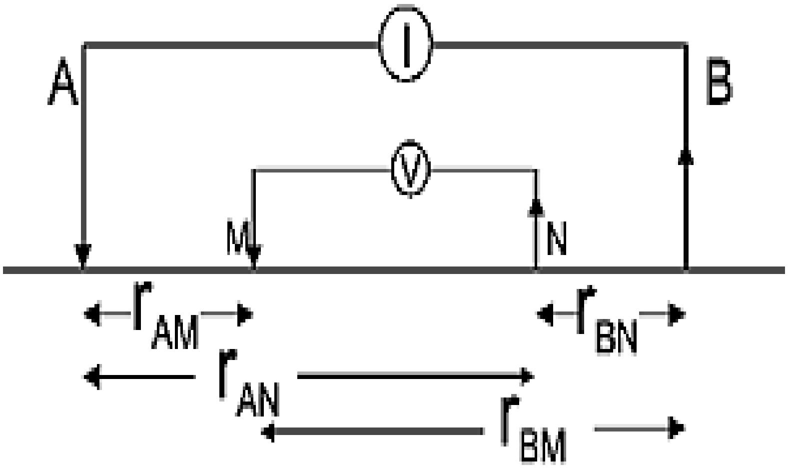

Figure 2: *General resistivity measurement method of four electrodes.*

shows the basic configuration of four electrodes for measuring resistivity.

The current electrodes, A and B act as source and sink, respectively. The potential at the electrode M due to the source A is $+\rho I/2\pi r_{AM}$ while sink B is $-\rho I/2\pi r_{BM}$. The combined potential (V) at M is (V_M) which relates the resistivity (ρ), current (I) and distance (r) between the source and sink is presented in Equation (11) as;

$$V_M = \frac{\rho I}{2\pi}\left(\frac{1}{r_{AM}} - \frac{1}{r_{BM}}\right) \tag{11}$$

Similarly, at N, the combined potential is

$$V_N = -\frac{\rho I}{2\pi}\left(\frac{1}{r_{AN}} - \frac{1}{r_{BN}}\right) \tag{12}$$

The potential difference measured between M and N,

$$V = V_M + V_N$$

$$V = \frac{\rho I}{2\pi}\left\{\left(\frac{1}{r_{AM}} - \frac{1}{r_{MB}}\right) - \left(\frac{1}{r_{AN}} - \frac{1}{r_{BN}}\right)\right\} \tag{13}$$

Then the resistivity (ρ) can be determined using the following formula stated here:

$$\rho_a = \frac{2V\pi}{I}\left\{\left(\frac{1}{r_{AM}} - \frac{1}{r_{MB}}\right) - \left(\frac{1}{r_{AN}} - \frac{1}{r_{BN}}\right)\right\}^{-1} \tag{14}$$

So, from the above equation we derive

$$\rho_a = \frac{2V\pi}{I}\,k, \tag{15}$$

where k is the geometric factor.

Apparent resistivity

Apparent resistivity is the volumetric average of a heterogeneous half-space, through a complex weighing function depending on the configurations of the electrode [24, 25]. On the other hand, true resistivity is the measured relationship between the current applied and the potential difference of an electrically homogeneous and isotropic half-space for a particular electrode arrangement and spacing [3]. This in situ resistivity is supposed to be homogeneous but not in a real situation, it gives the apparent resistivity of an equivalent uniform half-space and does not represent the ground's true resistivity [19]. The resistivity of the underlined layers is obtained from the measurement taken using a resistivity meter. Thus, apparent resistivity (ρ_a) is obtained by multiplying measured value by the geometric factors [26] under the assumption that the

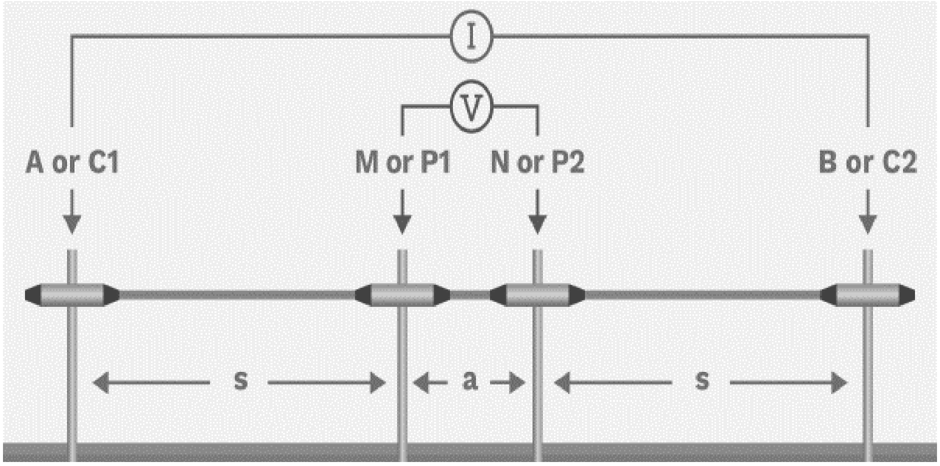

Figure 3: *Schlumberger array for resistivity measurement, consisting of a pair of current electrodes (A, B) and a pair of potential electrodes (M, N).*

ground is uniform; therefore, the measured resistivity is only the apparent resistivity and not the ground's true resistivity. Depending on the resistivity value of the layers underlined, the apparent resistivity increases or decreases with electrode spacing.

Schlumberger configurations

Schlumberger array used for VES investigation [11, 21], is a type of direct current resistivity survey described by its configuration. It makes use of four collinear electrodes, a pair of current electrodes as source and another pair of potential electrodes as the receivers. The potential electrodes are arranged in between the current electrodes; the central point is kept constant while the distance between the current electrodes is increased so that current can penetrate far down into the ground while the potential electrode is moved only when the voltage becomes too small to measure [27]. This arrangement enhances the capacity of the current to penetrate into greater depths, as the conductivity is distributed vertically [19]. The Figure 3 shows the Schlumberger configuration for resistivity measurement;

Let the separations between current and potential electrode be *(2s + a)* and *a*. This transforms Equation (14) as follows:

$r_{AM} = s$; $r_{MB} = s + a$; $r_{AN} = s + a$; $r_{BN} = s$

$$\rho_a = \frac{2V\pi}{I}\left\{\left(\frac{1}{r_{AM}} - \frac{1}{r_{MB}}\right) - \left(\frac{1}{r_{AN}} - \frac{1}{r_{BN}}\right)\right\}^{-1} \quad (16)$$

$$\rho_a = \frac{2V\pi}{I}\left\{\left(\frac{1}{s} - \frac{1}{s+a}\right) - \left(\frac{1}{s+a} - \frac{1}{s}\right)\right\}^{-1} \quad (17)$$

$$\rho_a = \frac{2V\pi}{I}\left\{\frac{s+a-s-s+s+a}{s(s+a)}\right\}^{-1} \quad (18)$$

$$\rho_a = \frac{2V\pi}{I}\left\{\frac{2a}{s(s+a)}\right\}^{-1} \quad (19)$$

$$\rho_a = \frac{2V\pi}{I}\left\{\frac{s(s+a)}{2a}\right\} \quad (20)$$

$$\rho_a = \frac{V\pi}{I}\left\{\frac{s(s+a)}{a}\right\} \quad (21)$$

Materials and method

Data acquisition

The research procedure was carried out at the geophysics research laboratory located at the Department of Physics, University of Ibadan. It was done using a tabletop model system made of a perspex container with a total depth of 29 cm and a length of 120 cm. Four samples of soil were used which were arranged in the transparent perspex container at different proportions. The experiment was done three times with three different arrangements. The arrangement from top to bottom is as follows;

- A three-layer soil containing humus (7 cm), sandy clay (10 cm) and sand (12 cm) which all together make a depth of 29 cm.
- A three-layer soil consisting of clay (4 cm), sandy clay (10 cm) and sand (15 cm) which all together make a depth of 29 cm.
- A two-layer soil consisting of clay (7 cm) and sand (11 cm) which make a depth of 18 cm.

In each of the arrangements, the soil samples were compacted one after the other to reduce the pore space in-between the soil particles and the moisture content was regulated. Electrical resistivity survey using Schlumberger array was carried out on each of the arrangements using Geopulse Tigre resistivity meter, first on three-layer arrangements which are humus, sandy-clay, and sand; then, clay, sandy-clay and sand; and lastly, a two-layer arrangement of clay and sand. The current electrode spacing starting from 1.0 cm to 55.0 cm and potential electrode spacing starting from 0.25 cm to 5.0 cm were used for measurement. Copper wire was used as probes in place of the copper electrode. A current of 0.5 mA was sent into the soil through the electrodes placed at two points with equal distance apart from the central point. The potential difference between the two points was measured using the resistivity meter in W-cm. Six measurements were taken in all, two for each arrangement for certainty purpose.

Results and discussion

Data acquired in centimetres were converted to meters and multiplied with the geometric factor (K) to obtain the apparent resistivity. The AB/2 was plotted against apparent resistivity and interpreted using a 2 layer master curve and WinResist. The mean of the thicknesses of each arrangement was mathematically simulated to obtain a constant value of 6.03 which serves as a multiplier to obtaining a value close to the real value. The thicknesses obtained were used to calculate the fraction of current that penetrated each layer using the equation for current (I) distribution in a uniform half space as stated in Equation (22); where *Ix* depends upon the current electrode spacing *L*:

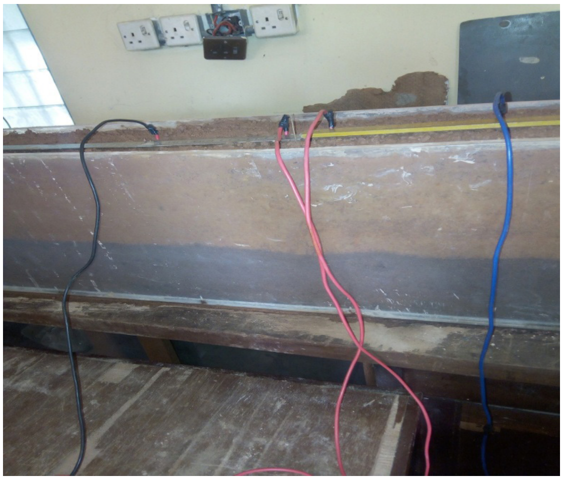

Figure 4: *The laboratory setup of three soil layers in a container.*

$$\frac{I_X}{I} = \left\{ \frac{2}{\pi} \tan^{-1} \frac{2z_1}{L} \right\} \tag{22}$$

The fraction of current between any two depths is obtained from the difference in the fractions above each depth, calculated with Equation (22).

First arrangement

The first arrangement contains humus, sandy-clay, and sand. The curve is a type-A curve that showed an increase in the resistivity value with depth in Figures 5 and 6, respectively. This indicates that the resistivity of humus is lower than that of sandy clay and the sandy-clay is lower than that of sand. This result is due to the degree of water saturation in the soil type. This factor depends on the porosity, permeability and the interconnectivity of pore spaces in the rock type. Humus and sandy clay have lower resistivity of 23.15 W-m and

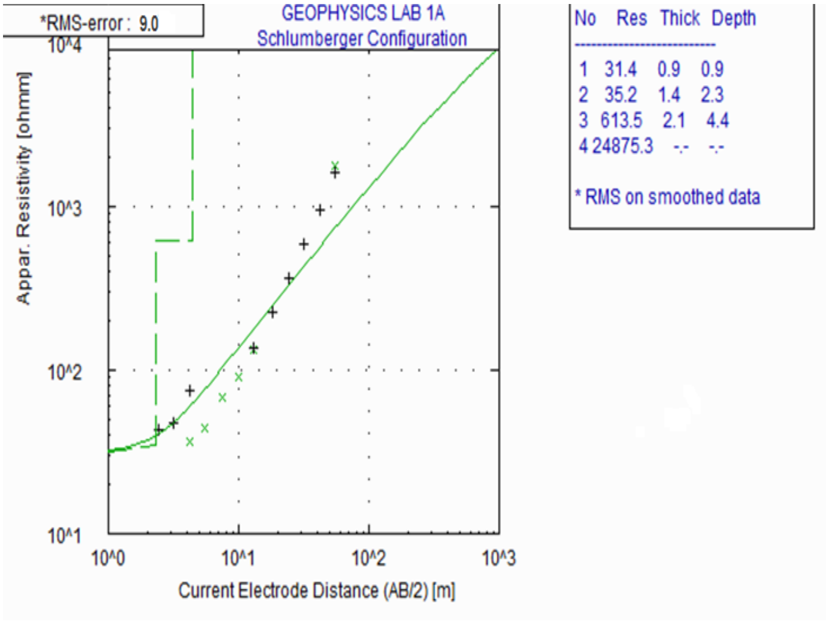

No	Res	Thick	Depth
1	31.4	0.9	0.9
2	35.2	1.4	2.3
3	613.5	2.1	4.4
4	24875.3	-.-	-.-

* RMS on smoothed data

Figure 5: *Resistivity measurement of soil layers against electrode spacing (AB/2) for the first arrangement.*

43.8 W-m, respectively, while sand has a higher resistivity of 757.95 W-m. Humus and sandy-clay have more porosity than sand because porosity decreases with grain size but they are less permeable, that is, they allow less water to flow. Sand in its case is less porous than humus and sandy-clay but its permeability is higher, so more water flows through it. It cannot hold water like the two types of rocks discussed earlier. This accounts for its high resistivity. The fourth layer is assumed as the plastic container whose resistivity value is very high and can be taken to be infinity. The thicknesses obtained are 5.0, 7.0 and 12.0 for the first layer, second layer and third layer, respectively, against the real values of 7.0, 10.0 and 12.0. The fraction of current passing through each layer is calculated using Equation (16) and it is 6% for first layer, 8% for second layer and 14% for the third layer.

Second arrangement

The second arrangement contains clay, sandy-clay and sand. The sand was made to serve as an aquifer as the base of the container was sealed and the flow of water out of it was restricted. In Figures 7 and 8, the curve is a type-H curve which demarcates the resistivity of each layer. Clay and sandy-clay have higher resistivity of 122 W-m and 161.7 W-m, respectively, while the resistivity of sand is 27 W-m. These values clearly show that in this particular experiment, the clay and the sandy-clay were less saturated compared to the sand. Sand is a good aquifer because of its high permeability property; therefore, it allows the flow of water. The fourth layer is assumed as the plastic container whose resistivity value is very high and can be taken to be infinity. The thicknesses obtained are 5.0, 11.0 and 34.0 for the first layer, second layer and third layer, respectively, against the real values of 4.0, 10.0 and 15.0. The fraction of current through each layer is calculated using Equation (16) and the values obtained are 6% for first layer, 13% for second layer and 35% for the third layer.

Third arrangement

The third arrangement contains clay and sand. The curve obtained in Figures 9 and 10 is a type-A curve which shows that there is a direct relationship between the increases of resistivity and depth. The resistivity of clay is 67 W-m while that of sand is 301.15 W-m. The value of resistivity obtained for each layer of rock shows the degree of saturation of each layer, and which indicates that the clay held

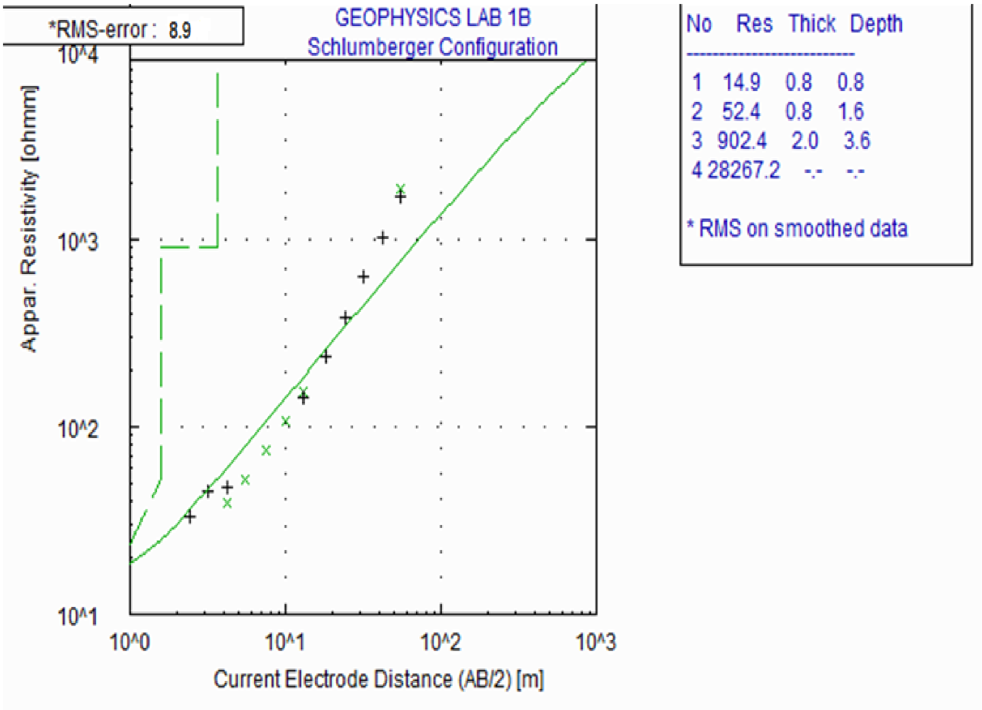

No	Res	Thick	Depth
1	14.9	0.8	0.8
2	52.4	0.8	1.6
3	902.4	2.0	3.6
4	28267.2	-.-	-.-

* RMS on smoothed data

Figure 6: *Resistivity measurement (repeated) of soil layers against electrode spacing (AB/2) for the first arrangement.*

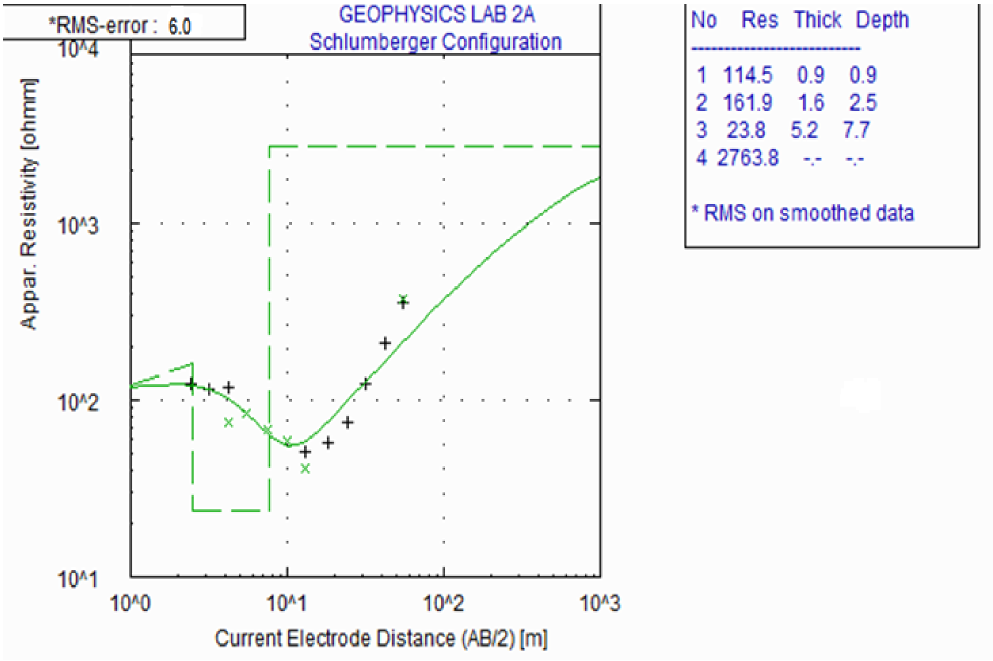

No	Res	Thick	Depth
1	114.5	0.9	0.9
2	161.9	1.6	2.5
3	23.8	5.2	7.7
4	2763.8	-.-	-.-

* RMS on smoothed data

Figure 7: *Resistivity measurement of soil layers against electrode spacing (AB/2) for the second arrangement.*

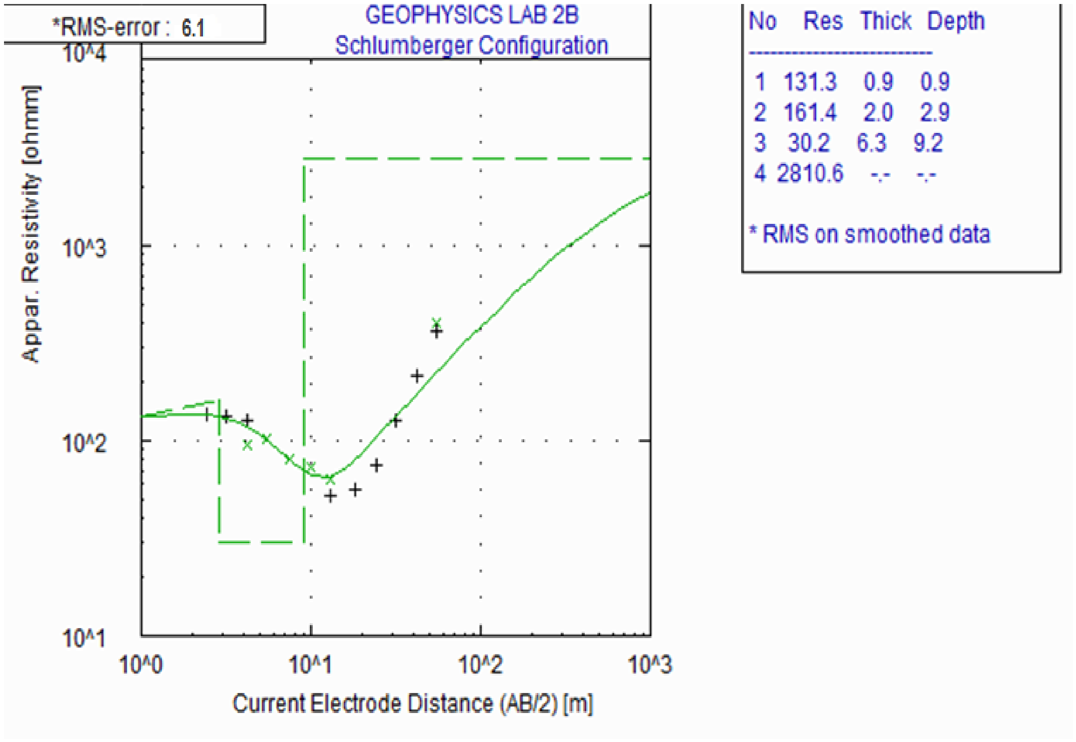

No	Res	Thick	Depth
1	131.3	0.9	0.9
2	161.4	2.0	2.9
3	30.2	6.3	9.2
4	2810.6	-.-	-.-

* RMS on smoothed data

Figure 8: *Resistivity measurement (repeated) of soil layers against electrode spacing (AB/2) for the second arrangement.*

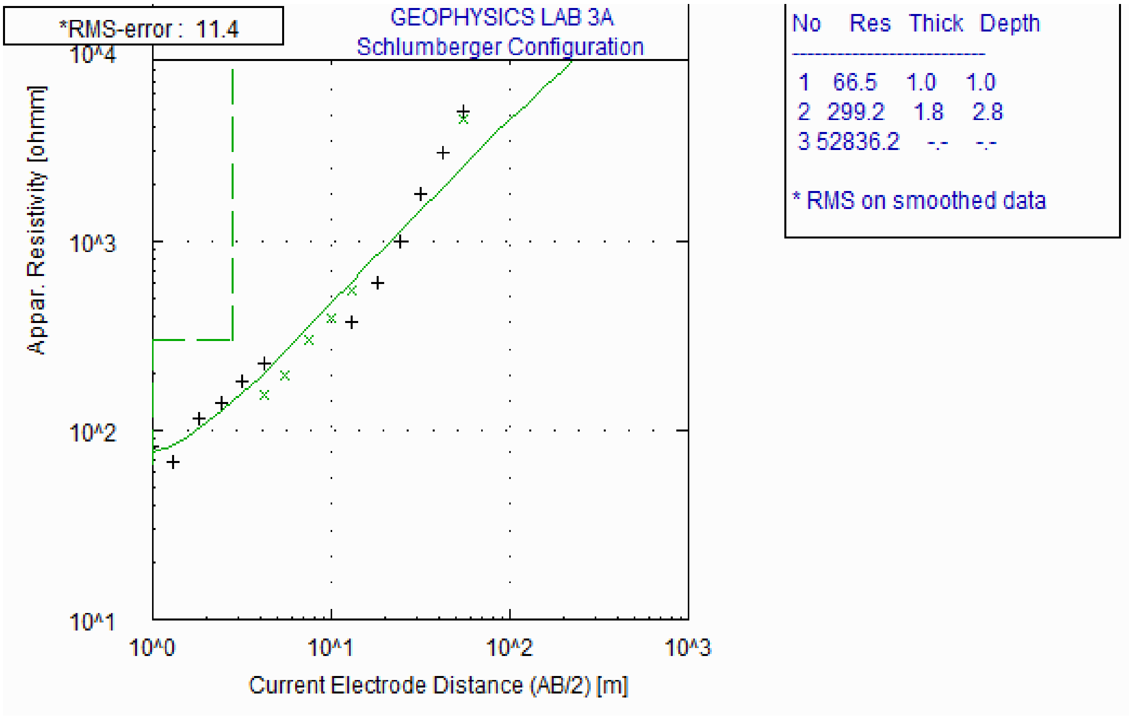

No	Res	Thick	Depth
1	66.5	1.0	1.0
2	299.2	1.8	2.8
3	52836.2	-.-	-.-

* RMS on smoothed data

Figure 9: *Resistivity measurement of soil layers in a container against electrode spacing (AB/2) for the third arrangement.*

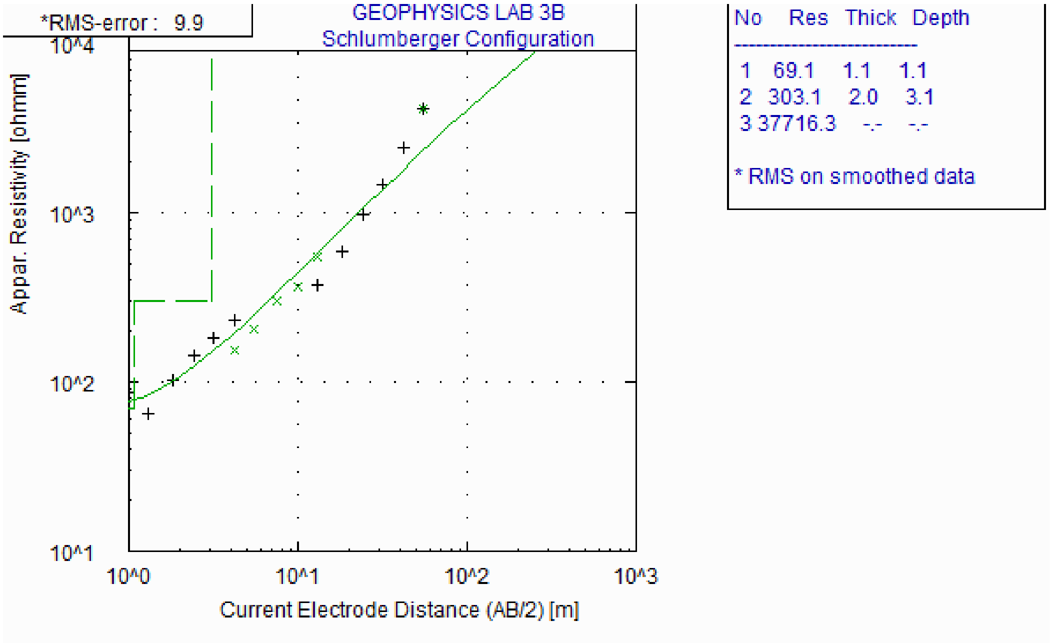

No	Res	Thick	Depth
1	69.1	1.1	1.1
2	303.1	2.0	3.1
3	37716.3	-.-	-.-

* RMS on smoothed data

Figure 10: *Resistivity measurement (repeated) of soil layers in a container against electrode spacing (AB/2) for the third arrangement.*

more moisture content and therefore is more conductive than the sand. The third layer is assumed to be the plastic container whose resistivity value is very high and can be taken to be infinity. The thicknesses obtained are 6.0 and 11.0 for the first layer and second layer, respectively, against the real values of 7.0 and 12.0. The fraction of current passing through each layer is calculated using Equation (16) and the values are 7% for first layer and 14% for second layer.

Conclusion

The percentage of current penetrating each layer shows that the effective current penetration depth depends on the spacing of electrodes. When the electrode spacing is increased, the effective current penetration depth is also increased. This is true when compared to Lowrie, 2007 who stated when Z = L/2, 50% of the current penetrates while about 90% of the current flows in the same layer when Z = 3 L. This implies that the percentage of current passing through a layer of shallow thickness is lower than that of passing through a deeper layer. Therefore, in electrical resistivity survey method, the subsurface depth being investigated should be considered for current needed.

References

[1] Archie, G.E. (1942): The electrical resistivity log as an aid in determining some reservoir characteristics. *Society of Petroleum Engineers,* 146(1), pp. 54–61, DOI: 10.2118/942054-G.

[2] Fukue, M., Minato, T., Horibe, H., Taya, N. (1999): The microstructures of clay given by resistivity measurements. *Engineering Geology*, 54(1–2), pp. 43–53, DOI: 10.1016/S0013-7952(99)00060-5.

[3] Meindinyo, R.O.K., Utuedeye, O, Adedokun, I.O. (2017): Vertical electrical sounding (Ves) for the determination of under ground resistivity in part of Nigeria Wilberforce Island, Amassoma, Bayelsa State. *IOSR Journal of Research & Method in Education*, 7(2), pp. 53–61, DOI: 10.9790/7388-0702035361.

[4] Coker, J. O. (2012): Vertical electrical sounding (VES) methods to delineate potential groundwater aquifers in Akobo area, Ibadan, South-western, Nigeria.

Journal of Geology and Mining Research, 4(2), pp. 35–42, DOI: 10.5897/JGMR11.014.

[5] Ghosh, D.P. (1971): The application of linear filter theory to the direct interpretation of geo-electrical resistivity sound measurement. *Geophysical Prospecting*, 11(4), pp. 471–508, DOI: 10.1111/j.1365-2478.1971.tb00593.x.

[6] Kearey, P., Brooks, M., Hill, I. (2002): *An introduction to geophysical exploration*. Blackwell Science.

[7] Gupta, S.C., Hanks, R.J. (1972): Influence of water content on electrical conductivity of the soil. *Proceedings of Soil Science Society of America*, 36(6), pp. 855–857, DOI: 10.2136/sssaj1972.03615995003600060011x.

[8] Herman, R. (2001): An introduction to electrical resistivity in geophysics. *American Journal of Physics*, 69(9), pp. 943–952, DOI: 10.1119/1.1378013.

[9] Hossain, Z., Cohen, A.J. (2012): Relationship among porosity, permeability, electrical and elastic properties. *SEG Technical Program Expanded Abstracts*, pp. 1–5, DOI: 10.1190/segam2012-1496.1.

[10] Giao, P.H., Chung, S.G., Kim, D.Y., Tanaka, H. (2003): Electric imaging and laboratory resistivity testing for geotechnical investigation of Pusan clay deposits. *Journal of Applied Geophysics*, 52(4), pp. 157–175, DOI: 10.1016/S0926-9851(03)00002-8.

[11] Syed, B.A., Siddiqui, F.I. (2012): Use of vertical electrical sounding (VES) method as an alternative to standard penetration test (SPT). *Proceedings of the Twenty-second International Offshore and Polar Engineering Conference Rhodes*, Greece, June 17–22.

[12] Kalinski, R.J., Kelly, W.E. (1993): Estimating water content of soils from electrical resistivity. *Geotechnical Testing Journal*, 16(3), pp. 323–329, DOI: 10.1520/GTJ10053J.

[13] Jatau, B.S., Patrick, N.O., Baba, A., Fadele, S.I. (2013): The use of vertical electrical sounding (VES) for subsurface geophysical investigation around Bomo area, Kaduna state, Nigeria. *IOSR Journal of Engineering (IOSRJEN),* 3(1), pp. 10–15, DOI: 10.9790/3021-03141015.

[14] Layade, G.O., Adegoke, J.A., Oladewa, F.C. (2017): Hydro geophysical Investigation for groundwater development at Gbongudu Area, Akobo Ojurin, Ibadan, Southwestern Nigeria. *Journal of Applied Sciences and Environmental Management*, 21(3), pp. 527–535, DOI: 10.4314/jasem.v21i3.14.

[15] McCarter, W.J., Desmazes, P. (1997): Soil characterization using electrical measurements. *Géotechnique,* 47(1), pp. 179–183, DOI: 10.1680/geot.1997.47.1.179.

[16] McCarter, W.J. (1984): The electrical resistivity characteristics of compacted clays. *Géotechnique,* 34(2), pp. 263–267, DOI: 10.1680/geot.1984.34.2.263.

[17] Zohdy, A.A. (1989): A new method for the automatic interpretation of Schlumberger and Wenner sounding curves. *Geophysics*, 54(2), pp. 245–253.

[18] Pandey, L.M., Shukla, S.K., Habibi, D. (2015): Electrical resistivity of sandy soil. *Géotechnique Letters*, 5(3), pp. 178–185, DOI: 10.1680/jgele.15.00066.

[19] Lowrie, W. (2007): *Fundamentals of geophysics.* Cambridge University Press.

[20] Telford, W.M., Geldart, L.P., Sheriff, R.E. (1990): *Applied geophysics*. Cambridge University Press: Cambridge, U.K.

[21] Zohdy, A.A. (1975): Automatic interpretation of Schlumberger sounding curves using modified Dar Zarrouck functions. *Geological Survey Bulletin*, 1313-E, pp. 39, DOI: 10.3133/b1313E.

[22] Keller, G.V., Frischnecht, F.C. (1966): *ElectricaI methods in geophysical prospecting*. Pergamon Press: Oxford England.

[23] Dahlin, T. (1996): 2D resistivity surveying for environmental and engineering applications. *First Break,* 14(1137), pp. 275–283, DOI: 10.3997/1365-2397.1996014.

[24] Zulfadhli, H.A., Mohd, H.M., Khairul Arifin, M.N. (2010): Electrical resistivity of subsurface: Field and laboratory assessment. *World Academy of Science, Engineering and Technology*, 45(1), pp. 799–m802.

[25] Keller, G.V. (1975): DC resistivity methods for determining resistivity in the earth's crust. *Physics of the Earth and Planetary Interiors,* 10(3), pp. 201–208, DOI: 10.1016/0031-9201(75)90046-1.

[26] Samouëlian, A. C., Isabelle, T.A., Bruand, A.G. (2005): Electrical resistivity survey in soil science: A review. *Soil and Tillage Research*, 83(2), pp. 173–193, DOI: 10.1016/j.still.2004.10.004.

[27] Nicholas, O. (1986): Schlumberger vertical soundings: Techniques and interpretations with examples from Kr1suv1k and Glerardalur, Iceland and Olkaria, Kenya, Geothermal Training Programme, United Nations University.